NUCLEAR RESONANCE IN DISPERSED SYSTEMS

By

KOAHSIUNG YANG

A DISSERTATION PRESENTED TO THE GRADUATE COUNCIL OF
THE UNIVERSITY OF FLORIDA
IN PARTIAL FULFILLMENT OF THE REQUIREMENTS FOR THE
DEGREE OF DOCTOR OF PHILOSOPHY

UNIVERSITY OF FLORIDA

1977

ACKNOWLEDGMENTS

To begin, I would like to thank Dr. Thomas A. Scott, the chairman of my supervisory committee, for suggesting the study and providing a very well equipped laboratory in which I could perform my work. Dr. Scott gave not only academic help and financial support, but also spiritual encouragement at the very time that I could concentrate most attention to the work. Special appreciation is given Dr. William Derbyshire of the University of Nottingham, England for his inspiring and tireless advice on both experiment and theory. This project was proposed by Dr. Derbyshire and initiated while he was visiting professor at the University of Florida. Appreciation is also felt for the other members of the supervisory committee: Drs. Raymond Pepinsky, Dinesh O. Shah, John W. Flowers and James W. Dufty.

I would also like to express my gratitude to Dr. Katherine Scott for her great help in the high resolution NMR study. Many thanks are extended to Mr. Paul C. Canepa for his electronic and technical expertise during the course of experiment.

Finally, I wish to present the work in memory of my dear grandmother who passed away on October 21, 1976. Because of many kinds of difficulties, I was not able to fly home in the last days of her life. Her kindness will be ever fresh to me in my whole life.

TABLE OF CONTENTS

Page

ACKNOWLEDGMENTS ii

LIST OF TABLES vi

LIST OF FIGURES vii

ABSTRACT xii

CHAPTER I INTRODUCTION 1

I.1 History and Significance of the Subject 1

I.2 The Microemulsions 3

I.2.1 The Surfactant and Interfacial Tension 3

I.2.2 The Formation of Microemulsions 3

I.3 The Liquid Crystal Phase 9

CHAPTER II BASIC THEORY 16

II.1 Nuclear Magnetic Resonance 16

II.2 Relaxation 19

II.3 Deuteron Relaxation in Water 27

II.4 Bound Water Model for Microemulsions 32

II.5 High Field Theory of Liquid Crystal Powder Pattern . . 46

CHAPTER III EXPERIMENTAL METHOD AND PROCEDURE 53

III.1 Sample Preparation 53

III.1.1 Preparation of Chemicals 53

III.1.2 Sample Sealing 54

III.2 Temperature Measurement and Controlling Apparatus . . 55

III.2.1 Cryostat 55

Page

III.2.2 Thermometer 57

III.2.3 Feedback Regulator 58

III.3 Nuclear Resonance Measuring Apparatus 61

III.3.1 Circuit Description 61

III.3.2 Electromagnet 63

III.3.3 Signal Generator and Frequency Synchronizer 66

III.3.4 Pulse Programmer and High Power Gated Amplifier 66

III.3.5 Sample Coil and Probe 67

III.3.6 Receiver 67

III.3.7 Phase Sensitive Detector 70

III.3.8 Diode Detector 75

III.4 Continuous Wave Method 76

III.4.1 Power Saturation and Line Width Broadening 76

III.4.2 Rate of Sweep and Magnetic Field Inhomogeneity 85

III.5 Noise 88

III.6 T_1 Measurement with $\pi \sim \tau \sim \frac{\pi}{2}$ Pulse Sequence 90

III.6.1 Disadvantage of Cross-Over Method 90

III.6.2 Ringing 93

III.7 T_2 Measurement with $\frac{\pi}{2} \sim \tau \sim \pi$ Pulse Sequence 98

III.8 Least Square Fit 100

III.9 Visual Observation 103

CHAPTER IV RESULTS AND CONCLUSIONS 108

IV.1 The Microemulsions 108

IV.1.1 The Validity of Bound Water Model 108

Page

IV.1.2 The Rotational Diffusion and Chemical Exchange 114

IV.2 The Liquid Crystals 129

IV.2.1 Explanation of Line Spectra and Relaxation . . 129

IV.2.2 Motional Narrowing of the Quadrupole Splitting 143

IV.3 Comparison between Hexanol and Pentanol in Water-Oil System 147

IV.3.1 Electrical Conductivity Difference 147

IV.3.2 Experimental Evidence and Explanation 147

IV.4 Conclusions 157

APPENDIX A 160

APPENDIX B 162

BIBLIOGRAPHY 164

BIOGRAPHICAL SKETCH 166

LIST OF TABLES

Table Page

(1) Effect of hexanol and potassium oleate on the average volume of water drops in hexadecane 7

(2) Effect of water contact on water droplet diameter in the hexadecane system 8

(3) Temperature dependence of various correlation times . . 29

(4) Components used for sample preparation 53

(5) The thickness of the motional restricted layer of the microemulsions at different temperatures and various radii 111

(6) Temperature dependence of the OH peaks in the proton spectrum of the hexanol microemulsion system 128

(7) The composition dependence of quadrupole splittings and widths of the wide lines 143

LIST OF FIGURES

Figure Page

(1) Schematic representation of the spontaneous development of negative interfacial tension as a result of the surfactants 4

(2) The decrease of interfacial tension due to hexanol . . 5

(3) The decrease of interfacial tension due to potassium oleate 6

(4) Schematic representation of the structure of the microemulsion 8

(5) Schematic representation of the structure of the birefringent cylinders 11

(6) Schematic representation of the structure of the birefringent lamellae 12

(7) The changes in the viscosity of microemulsions and liquid crystals with water/hexadecane ratio 13

(8) Disorientation and mutual entanglement results in higher viscosity than that of the initially well oriented liquid crystals 14

(9) The hydrogen bond association between carboxyl and hydroxyl groups from adjacent droplets 15

(10) The energy level splitting and population distribution in equilibrium of nuclei in a static magnetic field . . 17

(11) T_1 measurement by $\pi \sim \tau \sim \frac{\pi}{2}$ pulse sequence 23

(12) The envelope of free induction decay of the $\pi \sim t \sim \frac{\pi}{2}$ sequence 24

(13) The formation of an echo 25

(14) The envelope of spin echoes of the $\frac{\pi}{2} \sim \tau \sim \pi$ pulse sequence 26

(15) T_1 relaxation in pure D_2O 30

(16) Temperature dependence of the apparent activation energy 31

Figure Page

(17) The bound water model of microemulsions 35

(18) The relaxation time and population of the "bound" and "free" phases influenced by exchange rate 37

(19) The relationship between reorientation rate and temperature 38

(20) The relationship between reorientation rate of the "bound" and "free" phases and temperature 40

(21) The effect of exchange rate on (A) apparent reorientation rates, (B) apparent relaxation rates, (C) apparent populations of NMR in the "bound" and "free" phases . . 41

(22) Change of relaxation time due to chemical exchange . . 45

(23) Geometry of the electric field gradient principal axes at the deuteron nucleus and the laboratory frame in the liquid crystal 47

(24) Energy diagram for first order quadrupole perturbation of the Zeeman effect of the deuteron nucleus 49

(25) The powder pattern resonance line for I = 1 50

(26) The bound water model of lamellae structure 52

(27) Cryostat 56

(28) Block diagram of Feed-Back Regulator for temperature control of the sample 60

(29) Simple block diagram for pulsed NMR experiment 62

(30) Block diagram of pulsed NMR experiment with phase sensitive detector 64

(31) Block diagram of pulsed NMR experiment with diode detector 65

(32) Probe network 68

(33) Simple diagram for tuning of preamplifier 69

(34) Phase detection 73

(35) (a) Nonlinear characteristic of a diode, (b) modified circuit for diode detection 74

(36) Diode detection 75

Figure Page

(37) The relation of the signal height to H_1 and H_m 78

(38) The relation between audio frequency f_m and line shape 79

(39) The affection of change of H_m upon H_1 80

(40) Line shapes of the cases: $f_m > \Delta f$ 82

(41) Characteristic for different side bands 83

(42) Line shapes corresponding to different modulation frequency f_m of signal composing both narrow and wide line 84

(43) The effect of slow and fast sweep upon the spectrum. . 86

(44) The distinction of line distortion due to magnetic field inhomogeneity and rapid passage 87

(45) Magnetization flipped down by an angle θ from initial direction 91

(46) Comparison between first pulses of $\theta=\pi$ and $\theta\neq\pi$ in T_1 measurements 92

(47) The observed FID as displayed on the X-Y recorder . . 94

(48) Effect of ringing on T_1 measurements 95

(49) Envelope of spin echoes of two typical liquid crystals 99

(50) Apparatus for visual observation 106

(51) Cryostat for visual observation 107

(52) The relation between line width and radius of the microemulsions 112

(53) Temperature dependence of the spin-spin relaxation rate due to the bound water 113

(54) The temperature dependence of T_1 of pure D_2O and D_2O in W/O=0.1 microemulsion 115

(55) The temperature dependence of relaxation times of the hexanol microemulsion W/O=0.1 116

(56) The temperature dependence of relaxation times of the hexanol microemulsion W/O=0.2 117

Figure Page

(57) The temperature dependence of relaxation times of the hexanol microemulsion W/0=0.4 118

(58) The temperature dependence of relaxation times of the hexanol microemulsion W/0=0.6 119

(59) The temperature dependence of spin-spin relaxation time of the hexanol microemulsions above room temperature 122

(60) High resolution NMR spectrum of the hexanol microemulsion W/0=0.6 at 80°C 123

(61) High resolution NMR spectrum of the hexanol microemulsion W/0=0.6 at 23°C 124

(62) High resolution NMR spectrum of the hexanol microemulsion W/0=0.6 at 60°C 125

(63) High resolution NMR spectrum of the hexanol microemulsion W/0=0.6 at 80°C 126

(64) High resolution NMR spectrum of the hexanol microemulsion W/0=0.6 at 23°C (30 minutes after 80°C) 127

(65) Line shape variation of the liquid crystal W/0=1.4 obtained on cooling the sample from room temperature to -19°C 131

(66) Line shape variation of the liquid crystal W/0=1.4 obtained by heating the sample from room temperature to 90°C 132

(67) The powder-pattern wide-line spectra in the derivative mode and the corresponding absorption line shape . . 133

(68) The wide-line spectrum of the hexanol liquid crystal W/0=1.4 after shaking 136

(69) The wide-line spectrum of the hexanol liquid crystal W/0=1.0 after shaking 137

(70) The composition dependence of the relaxation times of the hexanol system 138

(71) The temperature dependence of the relaxation times of the hexanol liquid crystal W/0=1.0 139

(72) The temperature dependence of the relaxation times of the hexanol liquid crystal W/0=1.2 140

Figure Page

(73) The temperature dependence of the relaxation times of the hexanol liquid crystal W/0=1.4 141

(74) The coexisting two features of the spin echo in hexanol liquid crystal W/0=1.2 142

(75) (A) Electrical resistance of microemulsions containing hexanol or pentanol as cosurfactant, (B) schematic representation of cosolubilized and microemulsions system 148

(76) Composition dependence of the relaxation times of the pentanol dispersion system 152

(77) Spin echoes from the pentanol emulsion W/0=0.6 at 3.72°C and 16.8°C 153

(78) Temperature distribution of two features of the spin echoes in the pentanol emulsion W/0=0.6 154

(79) The change of spin echoes of the pentanol emulsion W/0=0.6 on cooling 155

(80) The temperature dependence of the relaxation times of the pentanol emulsion W/0=0.6 156

Abstract of Dissertation Presented to the Graduate Council
of the University of Florida in Partial Fulfillment of the Requirements
for the Degree of Doctor of Philosophy

NUCLEAR RESONANCE IN DISPERSED SYSTEMS

By

Koahsiung Yang

December 1977

Chairman: Thomas A. Scott
Major Department: Physics

Continuous wave and pulse techniques have both been used to study deuteron NMR lineshape, resonance frequencies, and relaxation times T_1 and T_2 in oil-water dispersions as a function of temperature and composition. The systems studied contain hexadecane, potassium oleate, hexanol (or pentanol), and water. The water/oil ratio determines the phases: $W/O \lesssim 0.6$ for microemulsions, $W/O \simeq 1.0$ for cylindrical rod liquid crystal, and $W/O \gtrsim 1.2$ for lamellar liquid crystal. A model in which the water molecules rapidly exchange between a "bound" state on the surfactant interface and a "free" state in the bulk liquid is highly successful in explaining many of the observations.

For the microemulsions the relaxation rate is proportional to the reciprocal of the radius of the water droplet spheres dispersed in the oil. The correlation time for both bound and free molecules is on the order of 10^{-12} sec, which is fast compared with the reciprocal of the resonance frequency(10^{-6} sec). The electric quadrupole interaction is averaged to zero by the rapid interchange of water between the two states and diffusion of "bound" molecules around the spherical surface of the droplets. The high resolution data show that the chemical shift difference at 23°C between the two OH peaks of the hexanol and H_2O is approximately 0.045 ppm and therefore the lifetime of the OH is about 250 ms. The chemical exchange rate becomes rapid when the temperature is raised to 60°C and thus explains the anomaly in T_2 occurring at 57°C.

The cylindrical rod and lamellar liquid crystal phases exhibit a static quadrupolar splitting of several hundred Hz, which was most readily observed as a CW powder pattern spectrum. The observed quadrupole splitting is approximately ten times smaller than is expected from the two state bound-free model. The correlation time for slowest tumbling of the bound water at room temperature, 0.32×10^{-6} sec, is only slightly larger than the characteristic time of experiment, approximately 0.15×10^{-6} sec. This explains the large degree of motional averaging.

The pentanol emulsion has two coexisting features of the spin echoes, one for isotropic microemulsion and the other for a liquid crystalline structure with $T_2 = T_2^+ \simeq 0.72$ ms. The portion having a liquid crystal characteristic is temperature dependent and is presumed to provide paths for charge carriers such as potassium ions, which enhance the electrical conductivity.

J a Scott

Chairman

CHAPTER I INTRODUCTION

I.1 History and Significance of the Subject

The membrane structure has been a major interest in biology for a number of decades. For many years, biophysists and physical chemists have used nuclear resonance techniques to study the structure and mobility of the "head" group in lipid membranes. This is basically a water-surfactant-lipid interface. The properties of the lipid and surfactants separately are understood fairly well from extensive studies of their chemical shift, mass spectroscopy, UV and IR light absorption, etc. But upon addition of water the system becomes much more complicated. The principal difficulty encountered in the use of proton nuclear magnetic resonance lies in the extreme difficulty of resolving the resultant multicomponent spectra into assignable resonances[1],[2], especially when these individual resonances occur over a wide frequency range(typically several kHz), and overlap each other. Deuteron magnetic resonance(DMR) was first used in 1971 to study the mobility of the hydrocarbon chains, in isotopically enriched molecules by Oldfield, Chapman and Derbyshire. As a simple model, they studied the modulation, by cholesterol, of the quadrupole splitting in a synthetic di(perdeuterio)myristoyl-Lα-Lecithin, as a function of temperature. Subsequently, Finer[3], Smith[4], Seelig[5] and their collaborators have performed many DMR studies on the hydration of Lecithin and of the dynamics of the ^2H

dispersions spin labelled lipids occuring in membranes and model membranes. The kinetic properties of the hydratiar water in such "liquid crystals" are gradually becoming clear to us.

The structure and physical properties of thermotropic liquid crystals and lyotropic systems are also among the major interests of the petroleum and pharmaceutical industry. They are intimately related to the problems of oil recovery, and pollution, and the mechanism of action of detergent, med cine, etc.

The microemulsion systems and liquid crystals studied in this dissertation are composed of hexanol (pentanol), hexadecane, potassium oleate and deuterium oxide(D_2O). To describe the properties of the water we adopt a two state bound-free water model, which assumes a layer of water near the surfactants having prefered orientation and restricted motion while the remainings of water have bulk-like isotropy in motion. The validity of the model can be checked through DMR with both continuous wave and pulse techniques. The correlation time of bound water, phase transitions, probability of being bound, the isotropic rotational process of free water molecules and anisotropic rotational process of bound water molecules are expected to be deduced from the experiment.

A brief description of the microemulsion and liquid crystal phases of the system are given in the following sections of this chapter. An equally brief basic theory of nuclear resonance and its application to this particular system are provided in chapter II. Experimental method and procedure are described in chapter III. Chapter IV gives results and conclusions.

I.2 The Microemulsions

I.2.1 The Surfactant and Interfacial Tension

Oil and water can be dispersed in each other at the microscopic but not molecular level by introducing mixtures of surface-active compounds as emulsifiers. The mixtures of surface-active compounds are called surfactant and co-surfactant depending upon the degree of interfacial tension obtained. The systems studied in this dissertation are composed of hexadecane(oil), deuterated water, potassium oleate (surfactant), and alcohol(co-surfactant). The alcohol used is hexanol/ or pentanol, but we put emphasis on the hexanol system.

The potassium oleate creates the interfacial film. The spontaneous development of negative interfacial tension is caused by penetration of hexanol through this film. A schematic representation is provided in Fig.(1), Fig.(2) and Fig.(3)[6] on the next three pages to show the hydrophilic and hydrophobic duality of potassium oleate and hexanol.

I.2.2 The Formation of Microemulsions

Microemulsions are optically clear, thermodynamically stable oil-water dispersions, obtained in low water/oil ratios. Phase diagrams showing the regions of microemulsion formation have been obtained for a number of systems[7]. Studies of these systems by light scattering[8], low-angle X-ray scattering[9], viscosity[10], electron microscopy[11], ultra-centrifugation[12], nuclear magnetic resonance[13],[14], infrared spectroscopy[13] and electrical resistance measurements[14] have been reported. Water-in-oil microemulsions

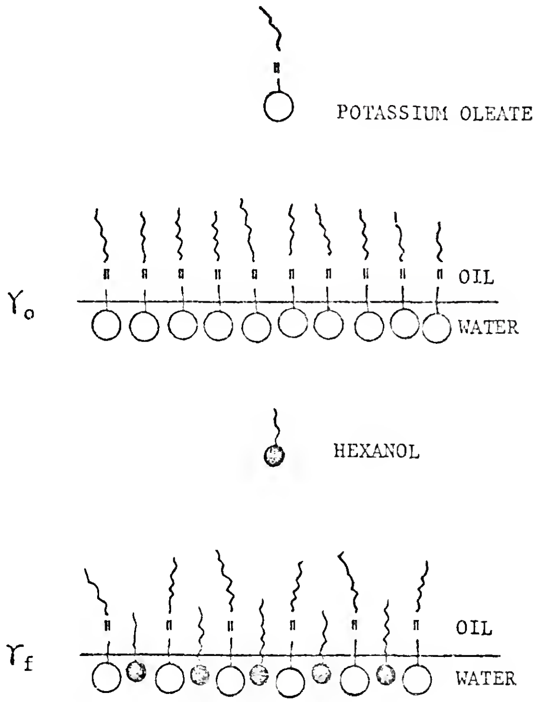

$$\gamma_f = \gamma_o - \pi$$

$$\gamma_f < 0 \quad \text{IF} \quad \gamma_o < \pi$$

where π is the interfacial tension reduction due to addition of hexanol

Fig.(1) A schematic representation of the spontaneous development of negative interfacial tension as a result of penetration of an interfacial film of potassium oleate by hexanol at the hexadecane/water interface [6]

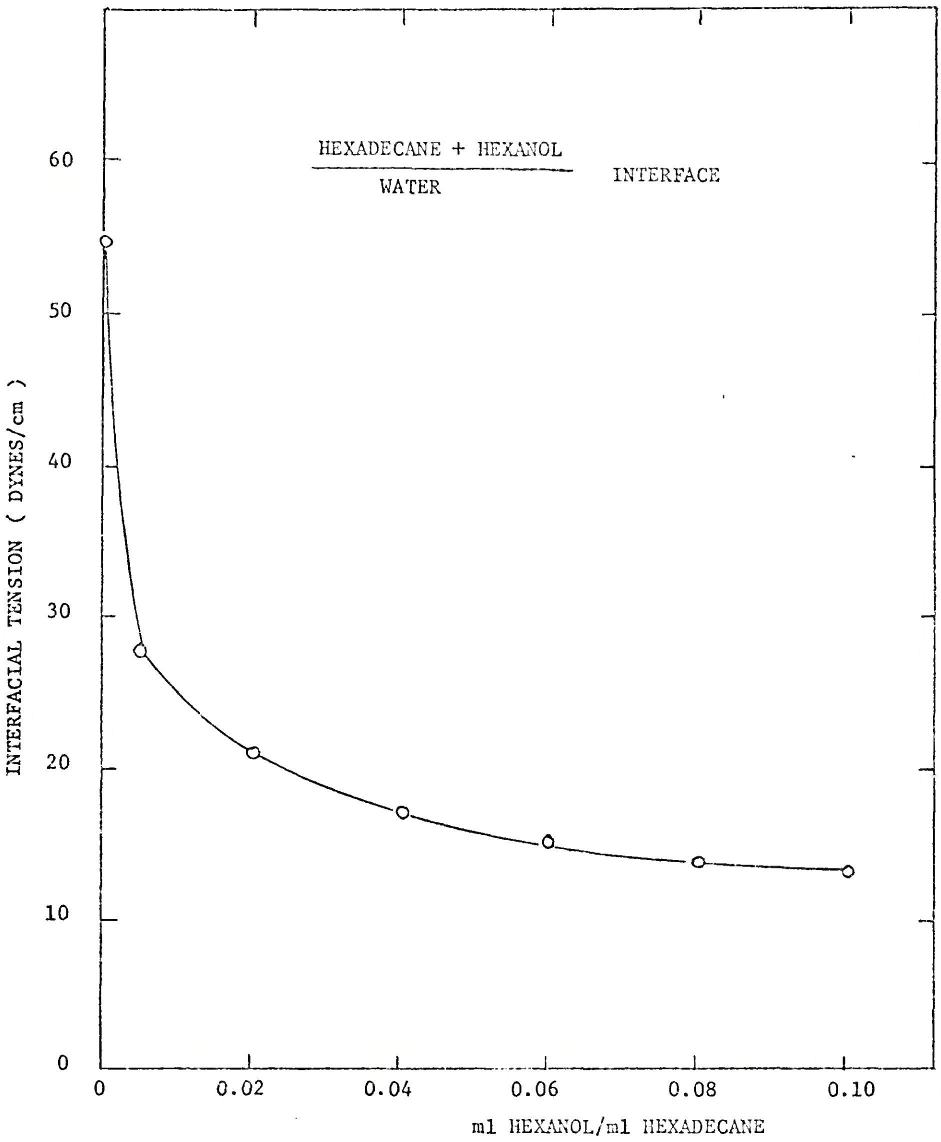

Fig.(2) The decrease of interfacial tension due to the surfactant hexanol [6]

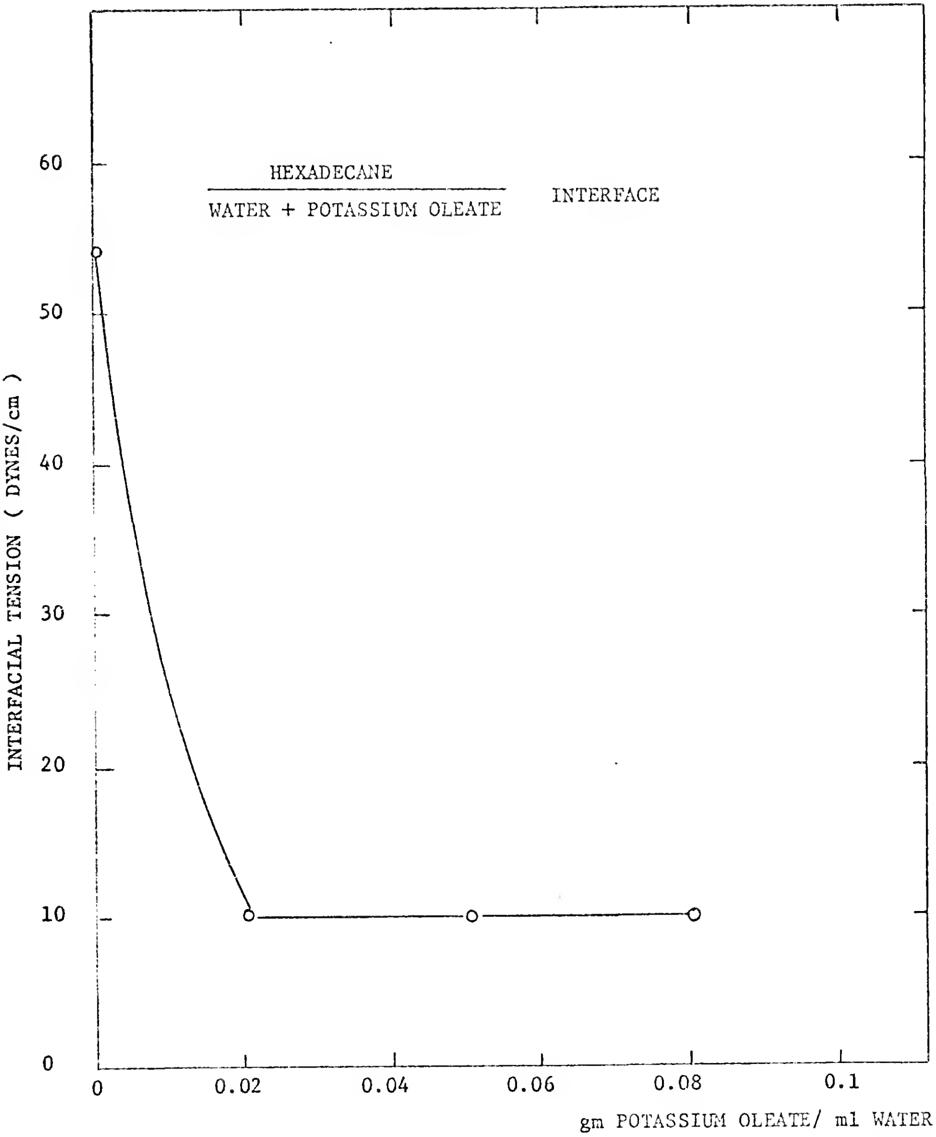

Fig.(3) The decrease of interfacial tension due to the surfactant potassium oleate [6] have been shown to consist of water droplets from less than 100 Å to several hundred Å in diameter surrounded by an interfacial film of surfactant and co-surfactant as in Fig.(4).

The effect of hexanol and potassium oleate on the average volume of water droplets in hexadecane are shown in Table(1)[15] and Table(2)[16].

Table(1) Effect of Hexanol and Potassium Oleate on the Average Volume of Water Drops in Hexadecane [15]

Interfacial Composition		Average Drop-Volume
Hexadecane(oil)	Water	
No additive	No additive	2.8x10^{-2}ml
Hexanol	No additive	
0.2 ml/ml of oil	No additive	6.0x10^{-3}ml
0.4 ml/ml of oil	No additive	5.0x10^{-3}ml
0.6 ml/ml of oil	No additive	5.0x10^{-3}ml
No additive	Potassium Oleate	
No additive	0.02 gm/ml of water	8x10^{-4}ml
No additive	0.06 gm/ml of water	8x10^{-4}ml
No additive	0.1 gm/ml of water	4.4x10^{-4}ml
Hexanol	Potassium Oleate	
0.025 ml/ml of oil	0.06 gm/ml of water	1x10^{-4}ml
0.05 ml/ml of oil	0.06 gm/ml of water	6.6x10^{-5}ml
0.075 ml/ml of oil	.06 gm/ml of water	Volume $<10^{-6}$ml

Table(2) Effect of Water Contact on Water Droplet Diameter in the Hexadecane Systems [16]

Aggregate	W/O (*)	Droplet Diameter Å
Inverted micelle	0.1	32
W/O microemulsion	0.2	46
W/O microemulsion	0.4	56
W/O microemulsion	0.6	72

(*) 1ml hexadecane was presented in system which contained 0.2 gm potassium oleate and 0.4 ml hexanol.

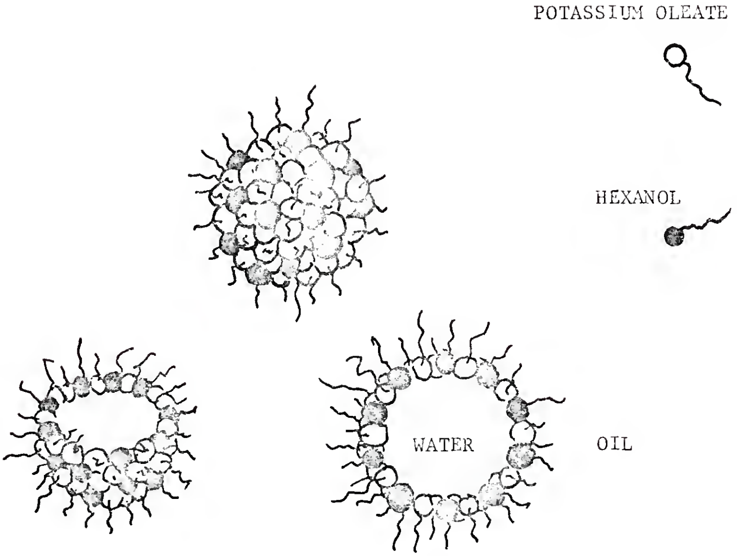

Fig.(4) Schematic representation of the structure of the microemulsions

I.3 The Liquid Crystal Phase

When the volume ratio of water to oil increases, the microemulsion breaks down and a liquid crystal forms. For the composition W/O = 1.0, a rod like structure [Fig.(5)] appears. Normally, the cylindrical structure has a diameter roughly 100 Å and a length of 1000 Å. Water is contained within the surfactant membrane. The membrane stability has been discussed by Shah[17] who concludes that a surfactant composition of 1 hexanol molecule to 3 potassium oleate molecules gives the most stable association. It is speculated that potassium oleate molecules occupy the corners and hexanol molecules occupy the centers of hexagons. This is why we choose the system with potassium oleate/ hexadecane = 0.2 gm/cm^3 and volume ratio of hexanol/hexadecane = 0.4.

As the water concentration is further increased, a lamellar structure [Fig.(6a)] forms. Additional water merely increases the gap between layers of surfactant [Fig.(6b)].

Figure(7)[18] shows the change in the viscosity of microemulsions and liquid crystals (cylindrical and lamellar structures) upon increasing the water/hexadecane ratio. The sharp increase of viscosity after disorientation, such as violent shaking, is due to the mutual entanglement of the liquid crystals [Fig.(8)]. After disorientation, the cylindrical structure does not increase viscosity as much as lamellar structure because of easier sliding due to circular cross section. The lamellar structure results in more resistance among domains after disorientation. Thus, the fact that the sample of W/O = 1.0 has less viscosity than the sample of W/O = 1.4 is well understood.

The gaps between liquid crystals of both cylindrical and lamellar structure are similar to slits of a diffraction grating which cause light (visible) interference. One therefore can observe colorful birefringence through polarized plates.

Oil spheres are formed for water/oil ratio greater than 2.0. In this case, oil is surrounded by a surfactant membrane. The hydrogen bond association [Fig.(9)] between carboxyl and hydroxyl groups from adjacent droplets causes an abrupt increase in viscosity [Fig.(8)]. This kind of electrostatic interaction is so strong that the viscosity is much larger than that of liquid crystals. This region is not of interest in the present dissertation study.

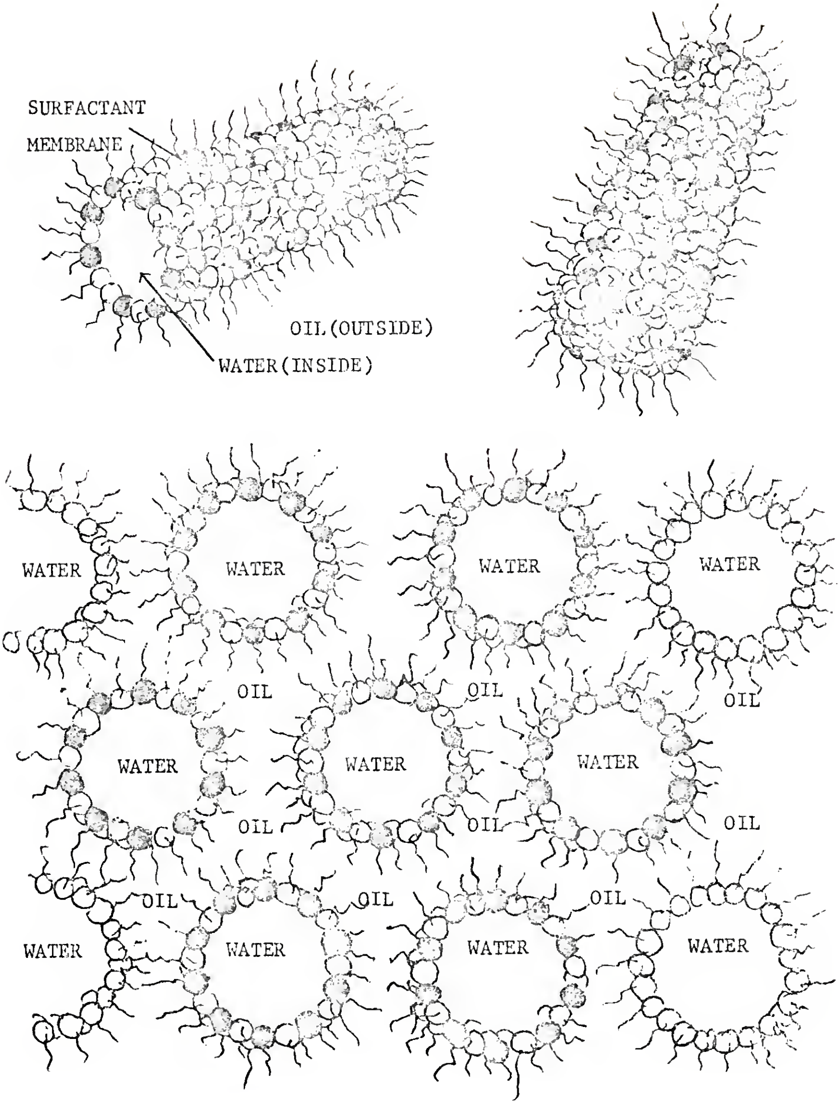

Fig.(5) Schematic representation of the structure of the birefringent cylinders

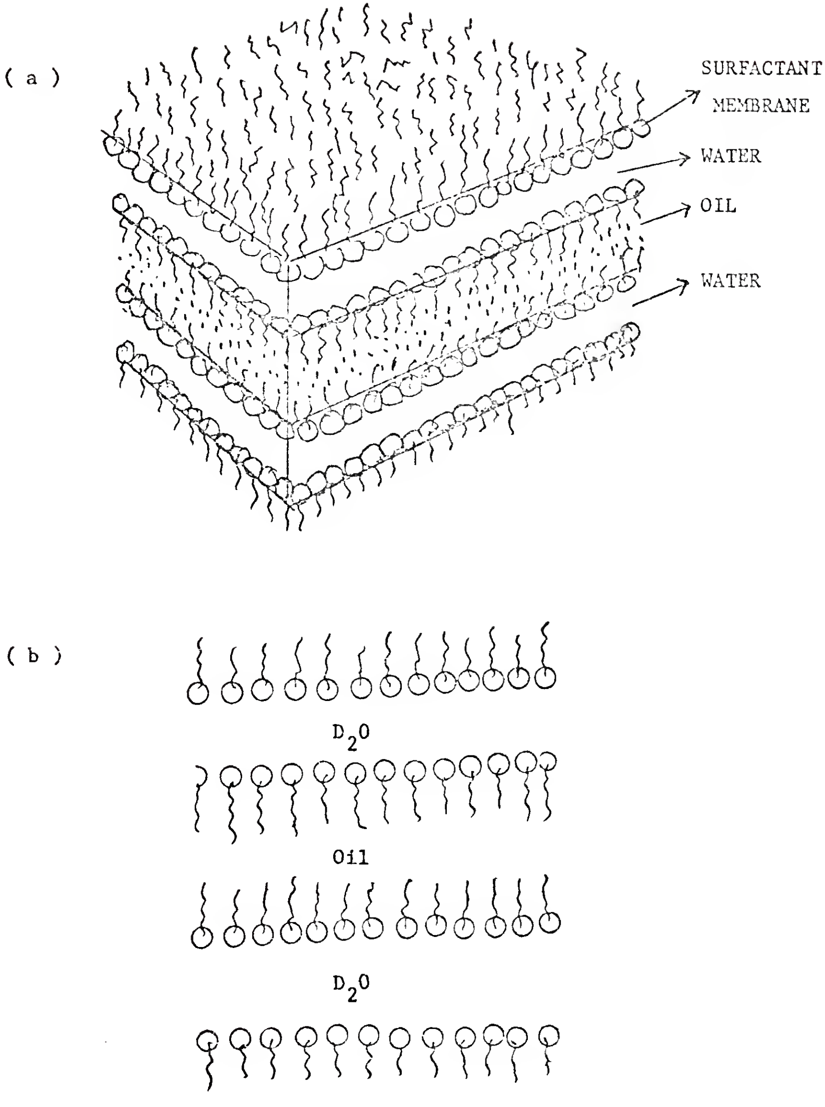

Fig.(6) Schematic representation of the structure of the birefringent lamellae

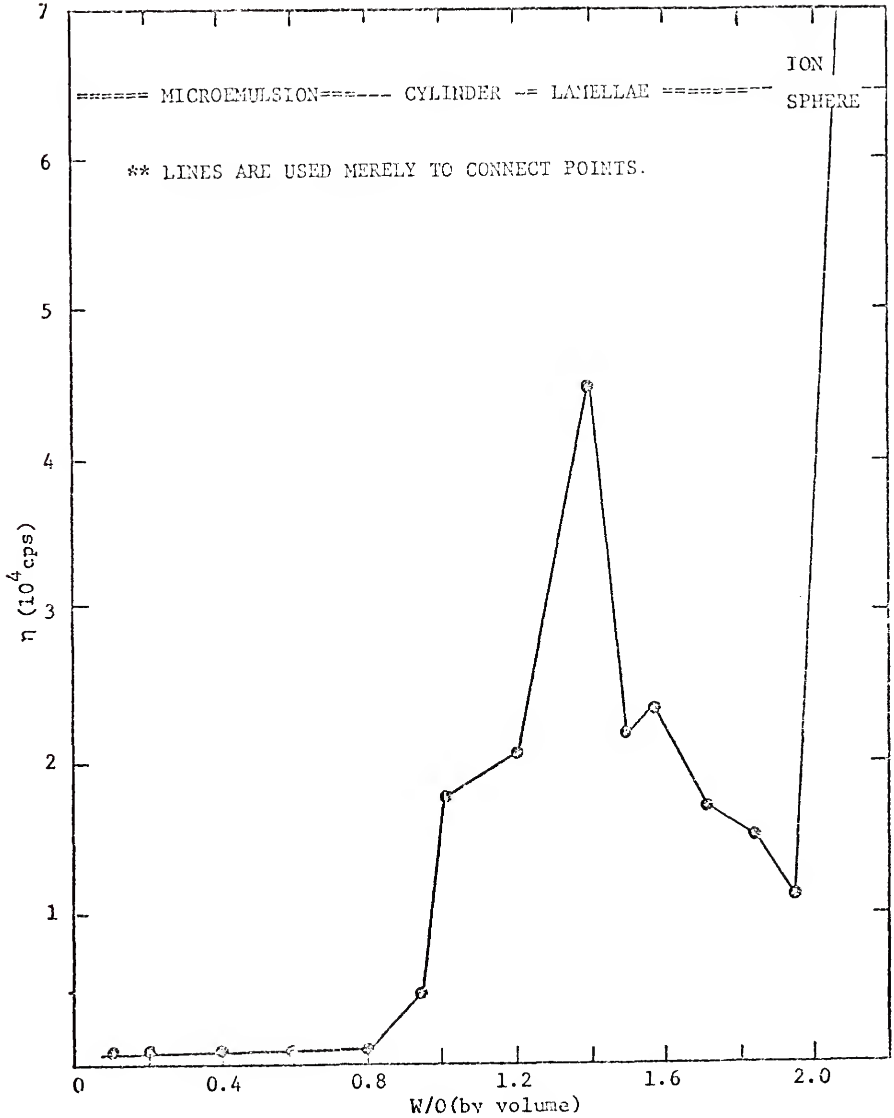

Fig.(7) The changes in the viscosity of microemulsions and liquid crystals with water/hexadecane ratio [18]

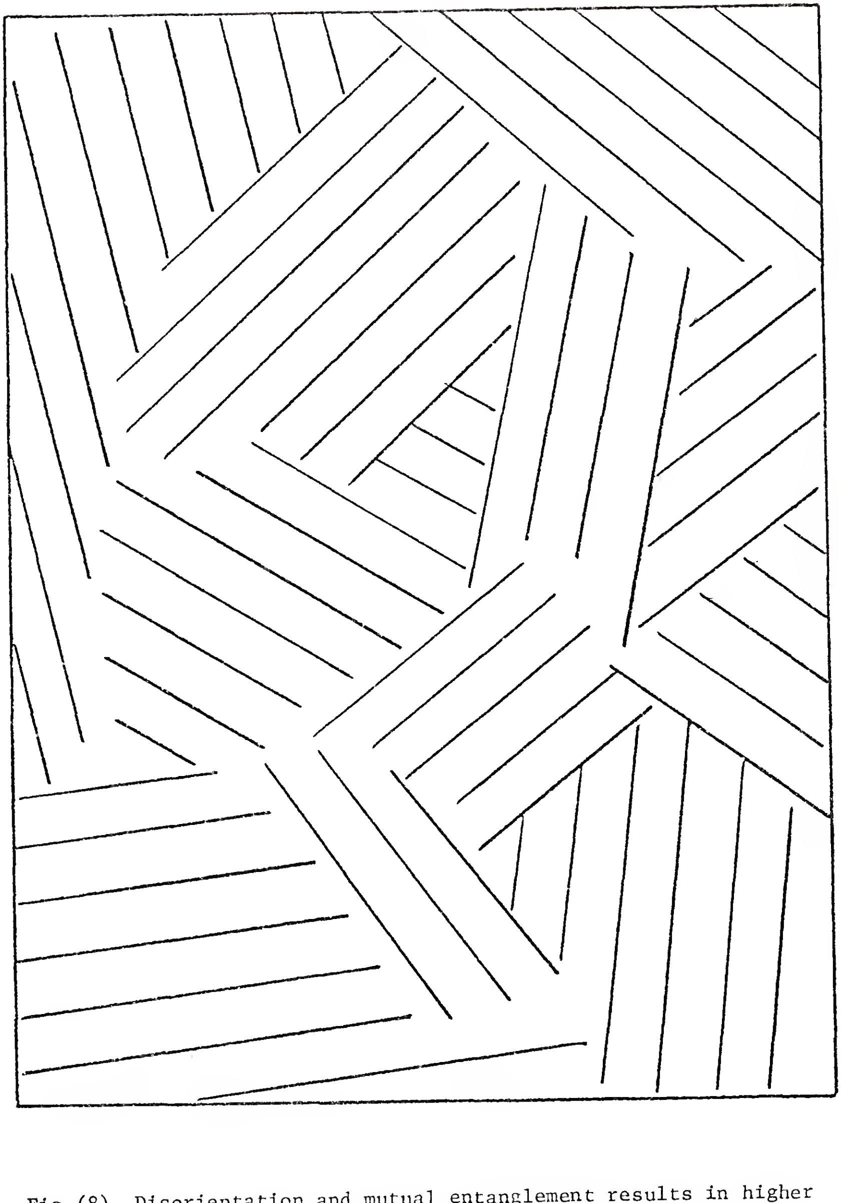

Fig.(8) Disorientation and mutual entanglement results in higher viscosity than that of the initially well oriented liquid crystals.

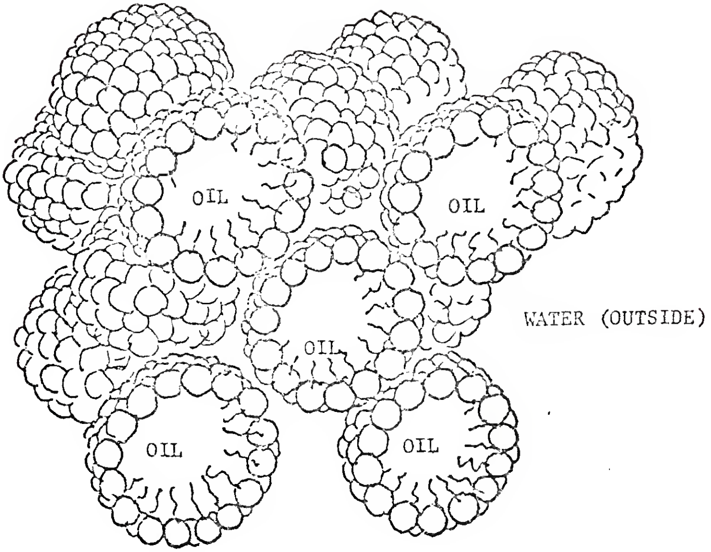

Schematic representation of the oil spheres suspended in water

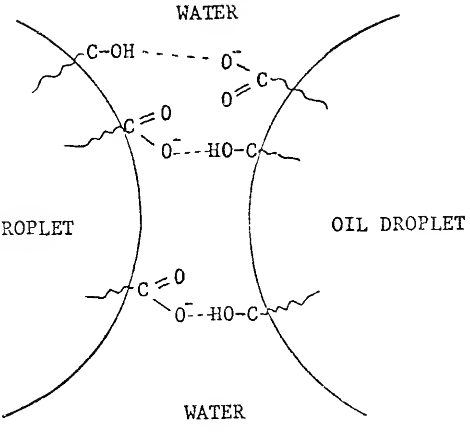

Fig.(9) The hydrogen bond association between carboxyl and hydroxyl groups from adjacent droplets causing an abrupt increase in viscosity for water/hexadecane ratio of 2.0 to 3.5

CHAPTER II BASIC THEORY

II.1 Nuclear Magnetic Resonance

A nucleus with spin $\vec{I}$ has a nuclear magnetic moment $\vec{\mu} = \gamma \hbar \vec{I}$, where γ is the nuclear magnetogyric ratio. If a magnetic field $\vec{B}_o$ is applied, the interaction Hamiltonian is

$$\mathcal{H} = -\vec{\mu} \cdot \vec{B}_o \qquad \text{(II.1.1)}$$

The nuclear moment precesses about the applied magnetic field, and the quantum mechanical equation of motion of the net magnetization $\vec{M}$ of an ensemble of spins is identical with the classical Newtonian law, namely the change of angular momentum is equal to the torque applied. Therefore

$$\frac{d\vec{M}}{dt} = \gamma \vec{M} \times \vec{B} \qquad \text{(II.1.2)}$$

where the macroscopic magnetization $\vec{M}$ is defined as a sum over nuclear magnetic moments of all nuclei.

Since the nuclear spin $\vec{I}$ is space quantized, the allowed eigenstates must be $m = -I, -I+1, -I+2, \ldots I-1, I$. In thermal equilibrium, the distribution of population on each energy level is governed by the Boltzman factor $\exp(-\gamma\hbar B_o/kT)$ [see Fig.(10)] to guarantee minimum internal energy.

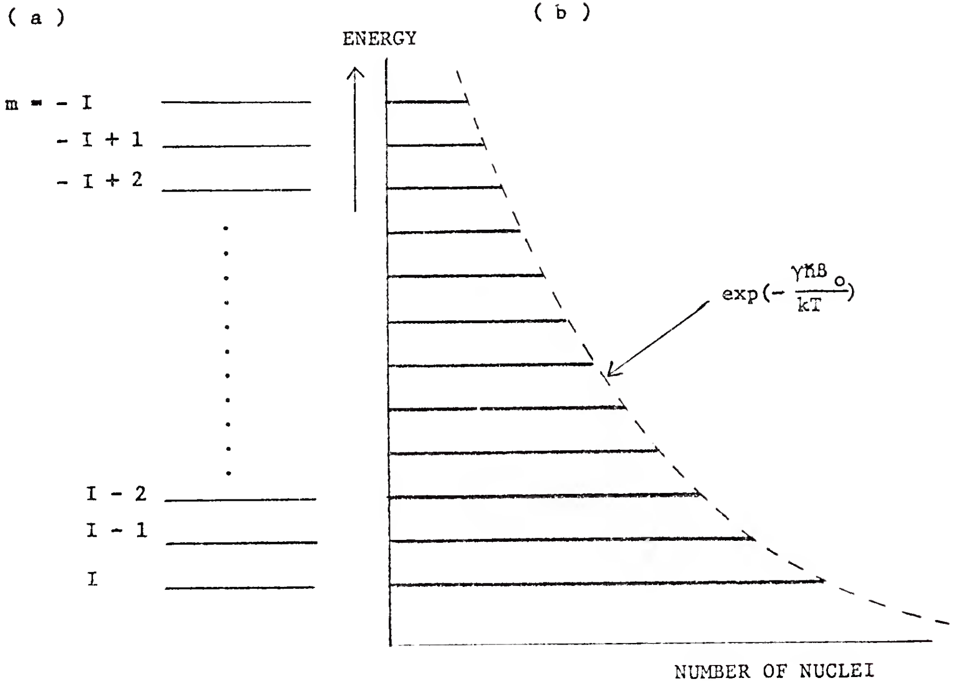

Fig.(10) The energy level splitting and population distribution in equilibrium of nuclei in a static magnetic field $\vec{B}_o$

$$\sum_{m=-I}^{I} N_m = N \qquad \text{and} \qquad \frac{N_m}{N_{m+1}} = \exp(-\gamma\hbar B_o/kT) \qquad \text{(II.1.3)}$$

where N_m is the number of nuclei in the eigenstate designated by magnetic quantum number m, N is the total number of nuclei of the ensemble, and T is the temperature of the lattice.

The statistical description above strictly requires a large number of nuclear moments but in practice $N \simeq 10^{20}$ so this is no problem. Transition between states is induced by the applied rf field with equal probability in both directions, but as the net population of the lower states are higher than those of the higher energy states there will be a net absorption of energy from the rf source.

A steady state nuclear resonance experiment can be interpreted as the result of two competing processes, the relaxation which tends to establish Boltzman inequalities after nuclei have been pumped to higher energy levels and the driving electromagnetic field that tends to destroy thermal equilibrium and to equalize the population of the different energy levels. An alternative "classical" description is that when disturbed from equilibrium the nuclear magnetic moment process about the magnetic field that they experience. An applied rf field,orthogonal to the main applied field,will interact with those precessing nuclei. An oscillatory field can be resolved into two counter-rotating components. The interaction will be strongest with the component rotating in the same direction as the precessing nuclei and will occur when the precessional frequency is the same as the rotation frequency of the rf field. It is often convenient to discuss the situation from a rotating frame of reference.

II.2 Relaxation

The macroscopic magnetization due to a spin system in a large static magnetic field relaxes because of the coupling between the microscopic magnetic moments of the nuclear spins and lattice motions. As the molecules move about in space, they, of course, carry the nuclear spins with them and the motions of the nuclear magnetic moments generate fluctuating magnetic field which is experienced by neighboring spins; this time varying field behaves in many respects like the rf field generated in an NMR transmitter. The probability of spontaneous transition is negligibly small at those low frequencies. Transitions between different energy levels have, therefore, to be induced. They may be induced by the experiments in the form of a rf field or by the system itself by a random motion which produces an oscillatory field of appropriate frequency.

Fluctuating local electric fields are produced also by molecular motion and where the nuclei have an electric quadrupole moment, this is an additional usually more potent source of relaxation. To describe the return from non-equilibrium to equilibrium, we use a characteristic time termed T_1, the spin-lattice relaxation. T_1 is often described as a longitudinal relaxation time. After a disturbance the nuclear magnetization may have a component at right angles to the applied static field. However because of the presence of various local fields, owing to the fact that the spins are actually not free but interact with each other and with their surroundings, there is a progressive dephasing giving rise to a transverse decay of the magnetization. We use T_2 to define this "spin-spin relaxation". T_2 is also called transverse relaxation time.

The Bloch equations are phenomenological equations developed to describe the longitudinal and the transverse relaxation mechanisms through the equation of motion(II.1.2) of the nuclear magnetization for an ensemble of free spins. In a laboratory frame, this equation is

$$\frac{d\vec{M}}{dt} = \gamma\, \vec{M} \times \vec{H} - \frac{M_x\hat{i} + M_y\hat{j}}{T_2} - \frac{M_z - M_o}{T_1}\hat{k} \qquad \text{(II.2.1)}$$

where $\hat{i},\hat{j},\hat{k}$ are the unit vectors of the laboratory frame of reference. Assume that the applied field is the sum of a d.c. field $H_z = H_o = -\frac{\omega_o}{\gamma}$ and of an rf field $\vec{H}_1$ of amplitude $H_1 = -\frac{\omega_1}{\gamma}$ rotating at a frequency ω in the neighbourhood of ω_o. This field will be the more effective of the rotating components of an applied field $H_x = 2H_1\cos\omega t$, linearly polarized along the OX axis of the laboratory frame. In the frame rotating around $\vec{H}_o$ at the frequency ω there is an effective static field. In the rotating frame the observed rate of nuclear precession equals $\gamma B_o \pm \omega$ and thus the effective field in the z direction$=(\gamma B_o \pm \omega)/\gamma$ whereas the field in the $\hat{i}'$ direction$= H_1$. Neglect of the counter-rotating component gives

$$\vec{H}_{eff} = (H_o + \frac{\omega}{\gamma})\hat{k}' + H_1\hat{i}' \qquad \text{(II.2.2)}$$

where $\hat{i}',\hat{j}',\hat{k}'=\hat{k}$ are the unit vectors of the rotating frame. The equation of motion of (II.2.1) can be rewritten as

$$\frac{d\vec{M}}{dt} = \gamma(\vec{M} \times \vec{H}_{eff}) - \frac{M_x^*\hat{i}' + M_y^*\hat{j}'}{T_2} - \frac{M_z - M_o}{T_1}\hat{k}'$$

where M_x^* and M_y^* are the transverse components of $\vec{M}$ in the rotating frame. Therefore,

$$\frac{dM_x^*}{dt} = -\frac{M_x^*}{T_2} + (\omega-\omega_o)M_y^*$$

$$\frac{dM_y^*}{dt} = -(\omega-\omega_o)M_x^* - \frac{M_y^*}{T_2} - \omega_1 M_z \qquad \text{(II.2.3)}$$

$$\frac{dM_z}{dt} = \omega_1 M_y^* - \frac{M_z - M_o}{T_1}$$

If a sufficiently long time has passed to allow transient effects to decay away, we can obtain a steady state solution by setting

$$\frac{dM_x^*}{dt} = \frac{dM_y^*}{dt} = \frac{dM_z}{dt} = 0 \qquad \text{(II.2.4)}$$

Therefore,

$$M_x^* = \frac{(\omega-\omega_o)\,H_1 T_2^2}{1 + T_2^2(\omega-\omega_o)^2 + \gamma^2 H_1^2 T_1 T_2}\,M_o$$

$$M_y^* = \frac{H_1 T_2}{1 + T_2^2(\omega-\omega_o)^2 + \gamma^2 H_1^2 T_1 T_2}\,M_o \qquad \text{(II.2.5)}$$

$$M_z = \frac{1 + (\omega-\omega_o)^2 T_2^2}{1 + T_2^2(\omega-\omega_o)^2 + \gamma^2 H_1^2 T_1 T_2}\,M_o$$

We can reconvert these values to the laboratory frame by using

$$M_x + iM_y = (M_x^* + iM_y^*)\,e^{i\omega t}$$

$$\text{(II.2.6)}$$

$$M_x = M_x^* \cos\omega t - M_y^* \sin\omega t$$

$$M_y = M_x^* \sin\omega t + M_y^* \cos\omega t \qquad \text{(II.2.6)}$$

The components of the magnetization in the laboratory frame are functions of time and can induce in a coil a detectable voltage at the frequency ω. The power absorption of $\mathcal{P} = -\vec{H} \cdot \frac{d\vec{M}}{dt}$ only occurs in the transverse direction and has its maximum value at $\omega = \omega_o$ by contribution of the term M_y^*.

Various pulse techniques have been reported in the literature[19] [20] for measuring the relaxation times T_1 and T_2. In this work the $\pi \sim \tau \sim \pi/2$ pulse sequence was used to measure T_1 and the $\pi/2 \sim \tau \sim \pi$ pulse sequence to measure T_2. For the measurement of T_1 in high field, the first pulse of time interval $\Delta t_{\text{pulse } 1}$ tilts down the magnetization M_o by π. As there is no transverse magnetization, only longitudinal relaxation exists. After time τ, the magnetization vector is tilted back to the x-y plane by the second pulse($\omega_o \Delta t_{\text{pulse } 2} = \pi/2$) so that the coil can pick up the signal. This pulse sequence and the measurement of T_1 are illustrated in Fig.(11), Fig.(12). The initial amplitude of the free induction decay signal recorded after the $\pi/2$ pulse is a measure of the net component of the magnetization along the z axis. In Fig.(13), the first $\pi/2$ pulse tilts the magnetization M_o down to the x-y plane. In the rotating frame coherent with the Larmor precession, the tilted magnetization spreads due to the variations in $\vec{H}_o$ over the sample. The second pulse applied at $t = \tau$ rotates the magnetization by π and it is therefore still in the x-y plane. The components of the magnetization that had precessed more rapidly by $\Delta\omega = \gamma\ \Delta B$ and had developed a phase lead of $\Delta\phi = \Delta\omega\ \tau$ now lag the mean by $\Delta\phi$. At $t = 2\tau$, the spread magnetization vectors

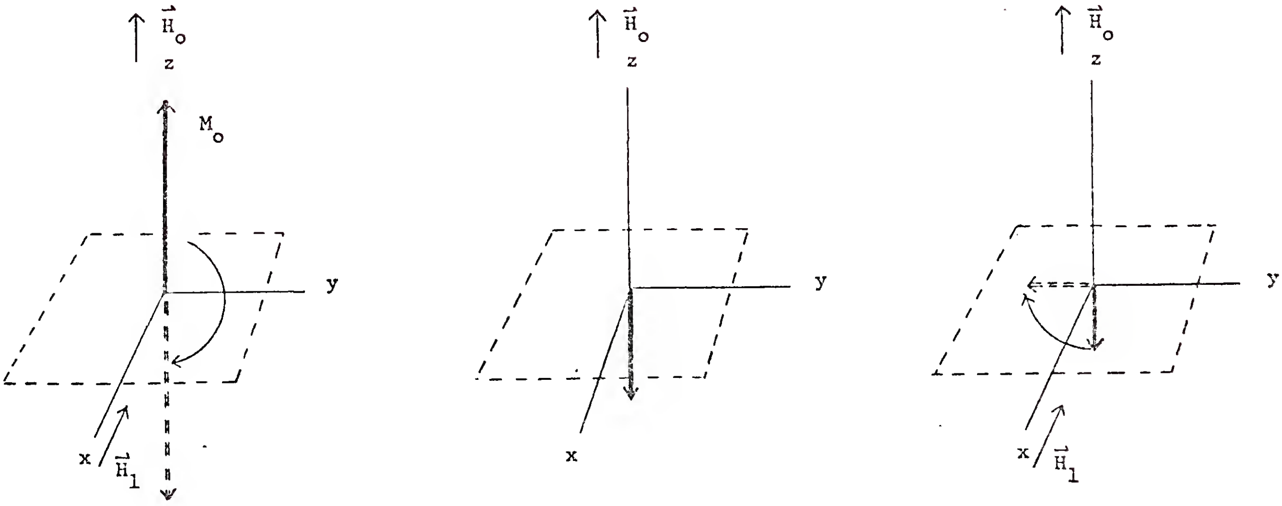

$t = 0$ $\quad 0 < t < \tau$ $\quad t = \tau$

Fig. (11) T_1 measurement by $\pi - \tau - \frac{\pi}{2}$ pulse sequence

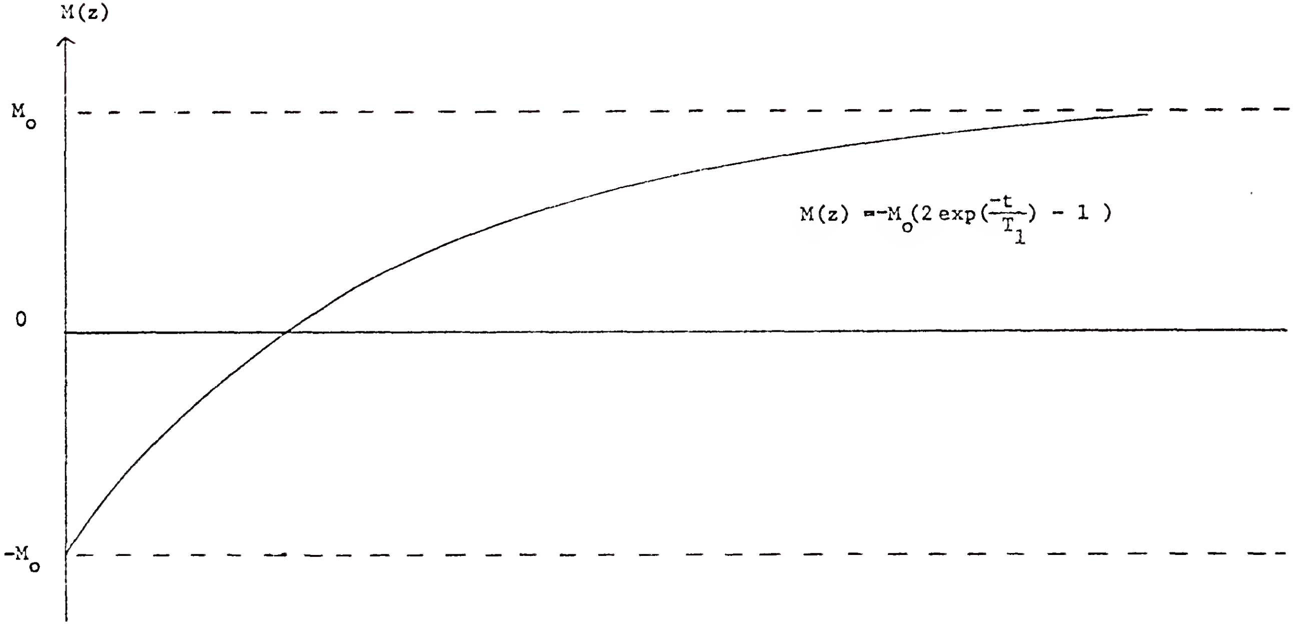

Fig. (12) The envelope of free induction decay of the π -t-$\frac{\pi}{2}$ sequence

Fig.(13) The formation of an echo. Initially the net magnetic moment vector is in its equilibrium position (a) parallel to the direction of the strong external field. The rf field $\vec{H}_1$ is then applied. As viewed from the rotating frame of reference the net magnetic moment appears (b) to rotate about $\vec{H}_1$. At the end of a $\pi/2$ pulse the net magnetic moment is in the equatorial plane (c). During the relatively long period of time following the removal of $\vec{H}_1$, the incremental moment vectors begin to fan out slowly (d). This is caused by the variations in $\vec{H}_1$ over the sample. At time $t=\tau$ the rf field $\vec{H}_1$ is again applied. Again the moments (e) are rotated about the direction of $\vec{H}_1$. This time $\vec{H}_1$ is applied just long enough to satisfy the pulse condition. This implies that at the end of the pulse all the incremental vectors begin to recluster slowly (f). Because of the inverted relative positions following the π pulse and because each incremental vector continues to precess with its former frequency, the incremental vectors will perfectly reclustered (g) at $t= 2\tau$. Thus the maximum signal is induced in the pickup coil at $t= 2\tau$. This maximum signal, or echo, then begins to decay as the incremental vectors again fan out (h).[From H. Y. Carr and E. M. Purcell, Physical Review 94, p630 (1954)]

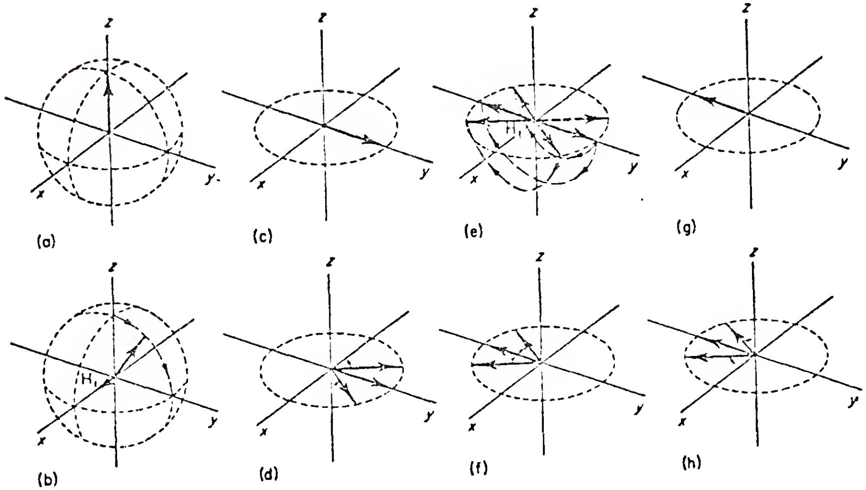

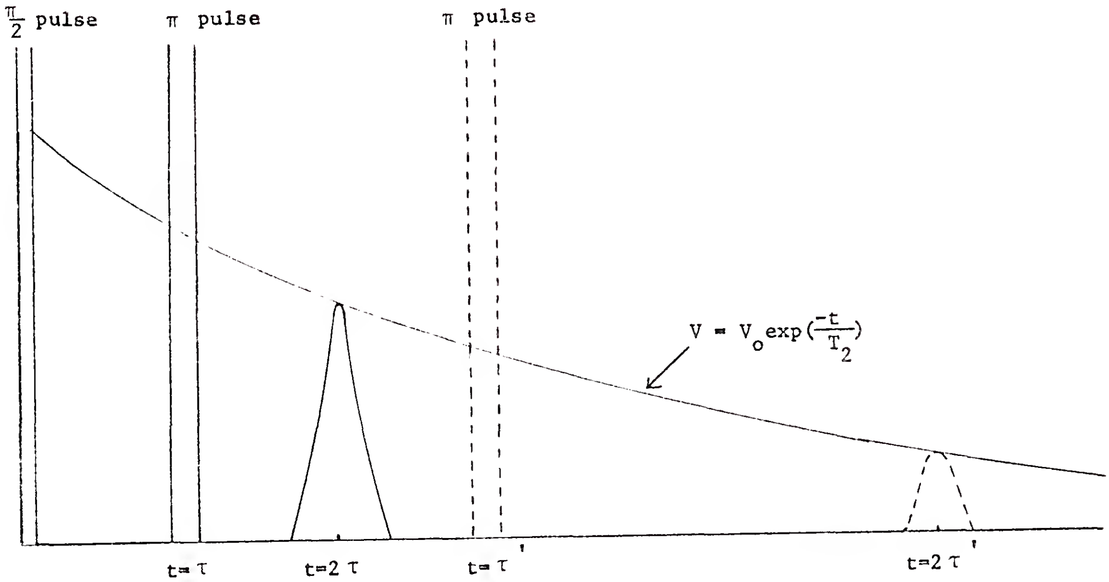

Fig.(14) The envelope of spin echoes of the $\frac{\pi}{2} - \tau - \pi$ pulse sequence overlap again and an "echo" occurs. The envelope of echoes generated by a series of π rf pulses is governed by $\exp(-2t/T_2)$ [Fig.(14)], that is if diffusion and other effects are ignored. (Note: All the pulse intervals are assumed much shorter than T_1 and T_2.)

II.3 Deuteron Relaxation in Water

The standard Hamiltonian representing the electric quadrupole interaction[21] is

$$\mathcal{H}_Q = \frac{e^2qQ}{4I(2I-1)}[\, 3\, I_z^2 - \vec{I}^2 + \frac{1}{2}\eta(\, I_+^2 + I_-^2)] \qquad \text{(II.3.1)}$$

where $eQ = \langle I,I|\sum_{i=1}^{A} e_i(\, 3\, z_i^2 - R_i^2)|\, I,I\rangle$

The two parameters used to define the electric field gradient tensor are

$eq = V_{zz}$ the z component of the field gradient

$\eta = \frac{V_{xx} - V_{yy}}{V_{zz}}$ the asymmetry parameter with $|V_{zz}| \geq |V_{yy}| \geq |V_{xx}|$

The quadrupole interaction was first shown by Pound[22] to dominate the spin lattice relaxation in water. The relaxation times T_1 and T_2 are given by Bloembergen[23], calculated by standard time-dependent perturbation theory applied to the quadrupole interaction term (II.3.1). They are

$$\frac{1}{T_1} = \frac{3}{80}\left(\frac{e^2qQ}{\hbar}\right)^2\left(\frac{2\tau_Q}{1 + \omega_o^2\, \tau_Q^2} + \frac{8\tau_Q}{1 + 4\, \omega_o^2\, \tau_Q^2}\right)\left(\, 1 + \frac{\eta^2}{3}\right) \qquad \text{(II.3.2)}$$

$$\frac{1}{T_2} = \frac{3}{80}\left(\frac{e^2qQ}{h}\right)^2\left(3\tau_Q + \frac{5\tau_Q}{1 + \omega_o^2\,\tau_Q^2} + \frac{2\tau_Q}{1 + 4\,\omega_o^2\,\tau_Q^2}\right)\left(1 + \frac{\eta^2}{3}\right) \quad (II.3.3)$$

Intensive studies have been undertaken by Eisenberg[24] and Hindman[25] on the quadrupole relaxation in deuterated water. Even in pure D_2O anisotropic motion does exist at lower temperature, due to cluster of hydrogen bonded molecules. The hydrogen bond influences the activation energy and in turn the relaxation. In these systems the quadrupolar relaxation mechanism is generally governed by two processes[25] (I) a hydrogen bond(dipole-dipole pair) breaking process and (II) a Brownian isotropic rotational diffusion process. These two processes compete with each other. Process (I) dominates at lower temperature and process (II) dominates at higher temperature; each of them is subject to a different activation energy. The relaxation time is a sum of two Arrhenius terms as shown in Fig.(15). For simplicity, we only focus on two correlation times associated with the processes mentioned. If exchange of D_2O molecules between the hydrogen bonded lattice and a isotropic rotational phase is rapid a mean correlational frequency will result

$$\tau_Q = \tau_Q^{I} + \tau_Q^{II} \quad (II.3.4)$$

and in turn influence the observed relaxation rate.

$$\frac{1}{T_1} = \frac{1}{T_1^{I}} + \frac{1}{T_1^{II}} \quad (II.3.4a)$$

T_1^{I} and T_1^{II} are the T_1 relaxation times corresponding to the correlation times τ_Q^{I} and τ_Q^{II}.

For D_2O, the averaged quadrupole coupling constant $\frac{e^2qQ}{h}$ over a wide temperature range is about 258.6 kHz[25]. Correlation times extracted from Hindman's experimental result are given in Table(3).

Table (3) Temperature dependence of various correlation time[25]

t (^oC)	τ_Q^I (x 10^{-12} sec)	τ_Q^{II} (x 10^{-12} sec)	τ_Q(apparent)$=\tau_Q^I+\tau_Q^{II}$ (x 10^{-12} sec)
5	1.93	2.76	4.70
20	0.75	2.03	2.79
40	0.24	1.41	1.66
60	0.091	1.03	1.12

From the values listed in Table(3), we obtain two correlation times essentially having the same order of 10^{-12}sec in all cases and therefore we can omit the quadratic term in the denominators of formulae (II.3.2) and (II.3.3). In a NMR experiment of resonance frequency 6.5 x 10^6 Hz. The simplified formula will become

$$\frac{1}{T_{1,2}} = \frac{3}{8} \left(\frac{e^2qQ}{\hbar} \right)^2 \tau_Q \qquad \text{when } \eta = 0 \qquad \text{(II.3.5)}$$

Activation energies due to two different processes can be calculated directly from Fig.(15) by the formula

$$E_{exp} = RT^2 \frac{d \ln T_1}{dT} \qquad \text{(II.3.6)}$$

,R is the ideal gas constant.

For the convenience of comparison with experimental results on microemulsions, Hindman's activation energy versus temperature graph is included in Fig.(16). The figure indicates that the rotational motion

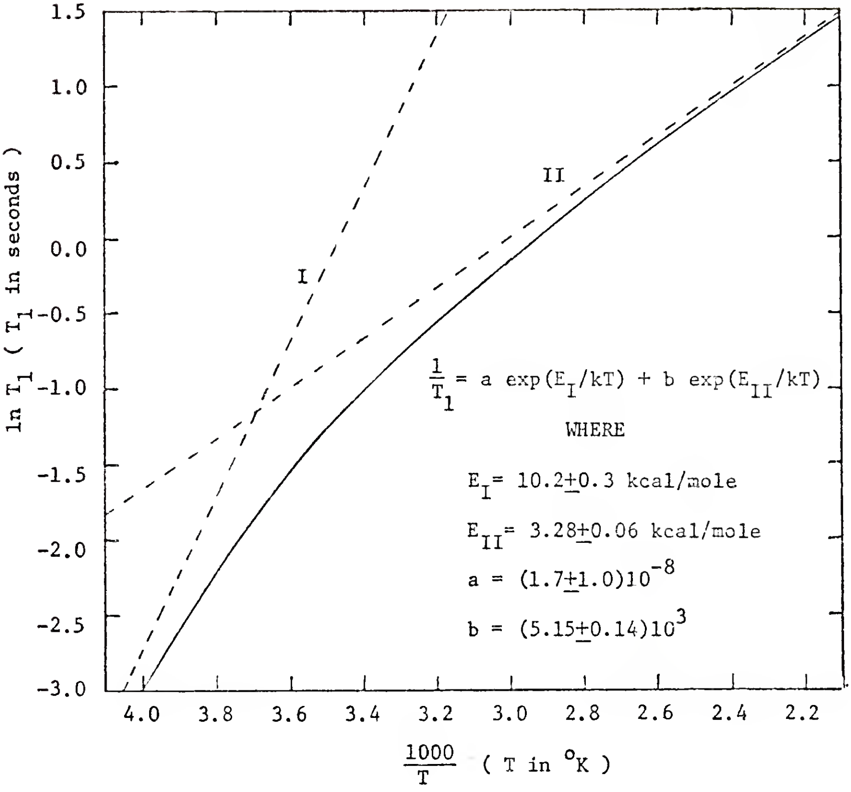

Fig.(15) The contribution due to (I) hydrogen bond breaking process and (II) isotropic rotational diffusion process in T_1 relaxation of pure D_2O[25]

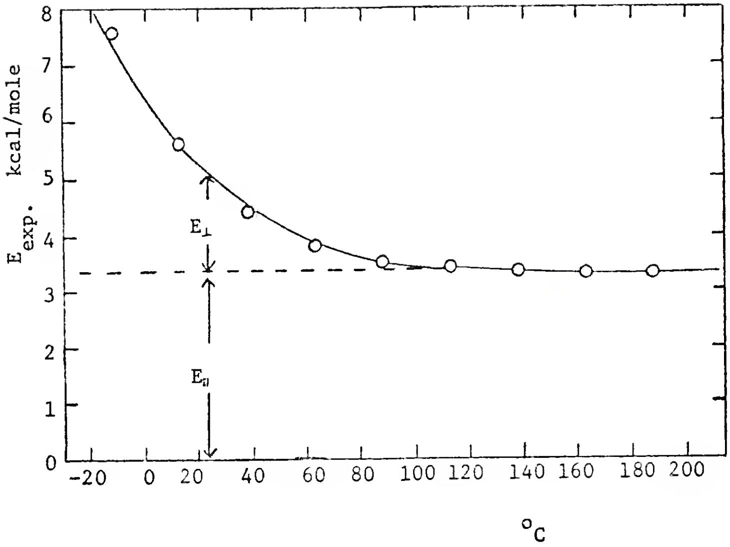

++ $$\frac{1}{T_1} = \text{constant}\cdot[m(\theta)\exp(\frac{E_\perp}{RT}) + n(\theta)\exp(\frac{E_\parallel}{RT})]$$

Fig.(16) Plot of apparent activation energies, $E_{exp.}$ (II.2.3.6) versus temperature, for D_2O water[25] for the D_2O molecules relaxing in process (II) (high temperature path) is isotropic and thus rules out the possibility that anisotropic rotation is a factor in the relaxation process. The anisotropic rotation will be reflected in differences in the apparent activation energies for relaxation of geometrically non-equivalent quadrupolar nuclei in the same molecule[26],[27].

In molecular terms water is normally considered as a mixture of hydrogen bonded and non-hydrogen bonded species. The nature of the mixture may be continuous or discrete, but in any event the ratio of non-hydrogen bonded to hydrogen bonded will increase with increasing temperature. The barriers to molecular rotation will differ between the species, and hence so will the corresponding activation energies.

II.4 Bound Water Model for Microemulsions

Assume there are two types of water [Fig.(17)] in the small water droplets, i.e. (a) free water, and (b) bound water, each subject to different rates of molecular reorientation. The bound water molecules have their prefered orientation determined by the polar groups of the surfactants at the oil/water interface. If the radius of the water droplet is r, with the thickness of the bound water layer Δr, the weighting factor of bound water P_b is given by

$$P_b = \frac{4\pi r^2 \ \Delta r}{\frac{4}{3} \ \pi r^3} = \frac{3 \ \Delta r}{r} \qquad \text{(II.4.1)}$$

Therefore, the weighting factor of free water is

$$P_f = 1 - P_b = 1 - \frac{3 \ \Delta r}{r} \qquad \text{(II.4.2)}$$

If the exchange of molecules between bound and free water is rapid, averaged physical observables $< X >$ will be determined. These can be the relaxation rate $\frac{1}{T_1}$, $\frac{1}{T_2}$ or signal height, etc. and may be expressed in the following form

$$< X > = P_b X_b + (1 - P_b) X_f \qquad \text{(II.4.3)}$$

and for the microemulsions:

$$< X > = X_f + 3 \Delta r \ (X_b - X_f) \frac{1}{r} \qquad \text{(II.4.4)}$$

If the observable $< X >$ is plotted against the reciprocal of radius, i.e. the same experiment is repeated by replacing different microemulsion samples, a constant slope is expected if the model is true. This X_f can be obtained from the intercept of the line with the ordinate, which also must be the same as given by a pure D_2O data at the same temperature.

When we measure the height of the free induction signal as the temperature is varied an abrupt change of intensity will be noted on crossing the freezing point. The loss of intensity below the freezing point is caused by freezing of bulk water. The intrinsic quadrupole constant $\frac{e^2qQ}{h}$ =258.6 kHz causes a very broad line; hence the signal amplitude contributed by the solid D_2O lattice is too small to be detected at the spectrometer settings used. The remainder of the signal observed is totally contributed by bound water. In fact this is often used as a definition of bound water. The "bound" water is that water whose molecular properties are modified by the proximity of, or interactions with the surface to such an extent that the structure of the water is not competible with bulk ice and this water remains unfrozen below the bulk freezing point. After freezing the relaxation time of the bulk phase is reduced and exchange with the bound phase is reduced to such an extent that exchange between bound water and bulk ice is slow or the new characteristic time scale and separate signals are observable. The spectrometer settings can be selected so that only one phase, i.e. the bound, is observed. The indications are that the rate of molecular motion within the bound phase is approximately the geometic mean of the bulk ice and bulk water values. Nevertheless, the bound water will be "frozen" eventually, when the temperature is further reduced and the rate of molecular motion decreased. Therefore, the change of intensity at the freezing point gives the weighting factor P_b of $\frac{3\,\Delta r}{r}$ [Fig.(17)] at that temperature.

Though the quadrupole interaction Hamiltonian is significant, we do not expect to see line splitting by the continuous wave method. The bound water molecules might be expected to have a prefered orientation relative to the droplet surface. However the occurance of a rapid exchange between bound and free water and the small size of the droplets results in water molecules experiencing regions of the bound phase at all orientation relative to the laboratory , i.e. the magnetic field on the NMR timescale thereby averaging out the quadrupolar spectral features. The quadrupolar interactions are manifested as relaxation mechanisms.

The exchange of nuclei or of molecules between two regions has been discussed by two groups of workers. Anderson and Fryer[28] and Zimmerman and Brittin[29]. Anderson and Fryer considered the transition

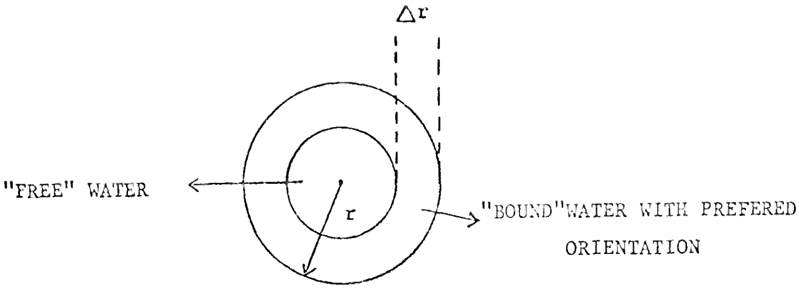

$$P_b = \frac{4\pi r^2 \Delta r}{\frac{4}{3}\pi r^3} = \frac{3\Delta r}{r}$$

$$P_f = 1 - P_b$$

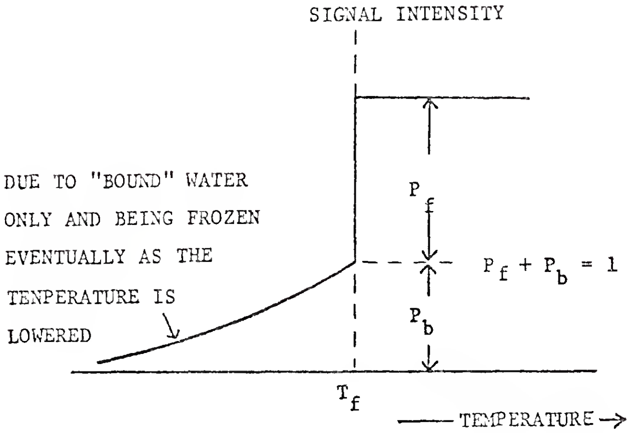

Fig. (17) The bound water model of microemulsions from slow to fast exchange where the exchange rate was compared with the molecular reorientation rates in the two phases, whereas Zimmerman and Brittin discussed the transition when the exchange rate was compared with the intrinsic relaxation rates in the two phases. At temperature to the high temperature side of the T_1 minimum both the spin lattice and spin-spin relaxation rates are inversely proportional to the molecular reorientation rate $\nu(= \frac{1}{\tau_Q})$ as in the equations (II.3.2), (II.3.3) and (II.3.5) although the proportionality relationship is more general than for relaxation by quadrupolar interactions. It should be noted that $\frac{1}{T_1}$ and $\frac{1}{T_2}$ are very much less than ν or $\frac{1}{\tau_Q}$. If the nuclei reside in the separate regions or phases for times sufficiently long for relaxation to occur, separate relaxations will be observed. If the residence lifetime is short compared with the characteristic relaxation times, population weighted average relaxation rates will be observed.

$$\frac{1}{T} = \frac{P_f}{T_f} + \frac{P_b}{T_b} \qquad \text{(II.4.5)}$$

Hence a small fraction of bound phase having a greatly increased relaxation rate can dominate the observed relaxation rate $\frac{1}{T}$.

e.g. if $T_f = 1$ s, $T_b = 1$ ms, $P_f = 0.99$ and $P_b = 0.01$

$$\frac{1}{T} = \frac{0.99}{1} + \frac{0.01}{10^{-3}} = 0.99 + 10 \quad \text{and } T \simeq 100 \text{ ms}$$

Zimmerman and Brittin have developed expression relating the apparent relaxation rates $\frac{1}{T_b'}$, $\frac{1}{T_f'}$ and P_b' and P_f' to the exchange rate. These may be represented diagramatically as follows

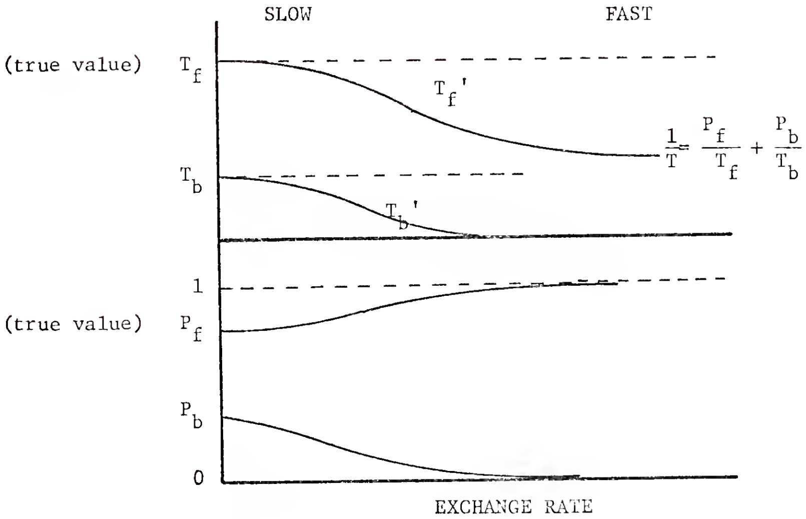

Fig.(18) The relaxation time and population of the "bound" and "free" phases influenced by exchange rate

In developing this treatment it has been assumed that the exchange process does not itself provide a relaxation mechanism. Because spin-lattice and spin-spin relaxation times can have different values exchange can be fast for one measurement and slow for the other. It is possible to generalize the treatment to apply to a larger number of discrete or to a continuous range of environments. Therefore fast exchange in the Zimmerman and Brittin sense means the observation of averaged NMR relaxation rates but the concept of separate phases has still some validity; many molecular rotations can occur in each phase before exchange occurs.

Anderson and Fryer discuss the problem where the residence lifetime in a phase becomes comparable to and ultimately exceeds the molecular reorientation rates in that phase. The mathematical treatments of the two models are formally similar but the physical consequences differ. When exchange is slow in both models nuclei can reorientate and relax in their separate environments before exchange occurs and the separate environments are essentially uncoupled. As $\frac{1}{T_1}$, $\frac{1}{T_2}$ $<< \nu_Q$ for much of the range it is possible for exchange to be slow in the Anderson and Fryer and fast in the Zimmerman-Brittin sense.

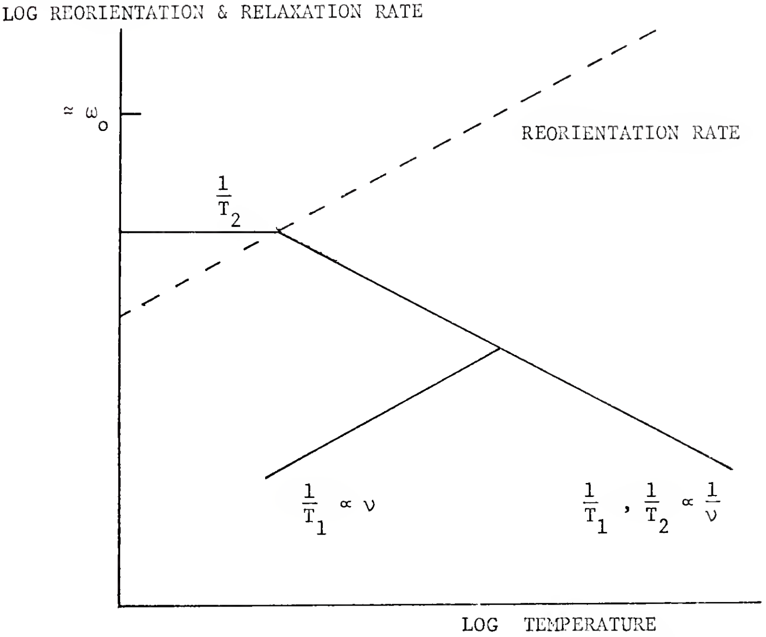

Fig.(19) The relationship between reorientation (or relaxation) rate and temperature (logarithmic scale)

Measurements of reorientation rates e.g. by dielectric techniques would still reveal separate phases but averaged relaxation rates will be observed. As these are inversely proportional to the reorientation rate the presence of a small fraction reorienting slowly will dominate the relaxation as discussed earlier. If the exchange rate is increased to become fast by the Anderson-Fryer criterion reorientation will occur at a rate determined by the population weighted average relaxation rate in the two phases.

$$\nu = P_f \nu_f + P_b \nu_b \qquad (II.4.6)$$

Using our previous values $P_a = 0.99$, $P_b = 0.01$, $\nu_b = 10^{-3}\nu_f$, ν is completely dominated by the abundant rapidly reorientating a phase and hence so is the recorded relaxation rate. This again assumes that the exchange process does not itself provide a reorientation mechanism.

We can imagine a "thought experiment" where we increase the exchange rate between two phases f and b (for convenience both may be assumed to be to the high temperature side of their maximum spin lattice relaxation rates), without at the same time modifying their intrinsic relaxation and reorientation rates. In practice this is impossible within a single system. An increase in exchange rate is normally accomplished by a change in temperature which will affect the intrinsic rates.

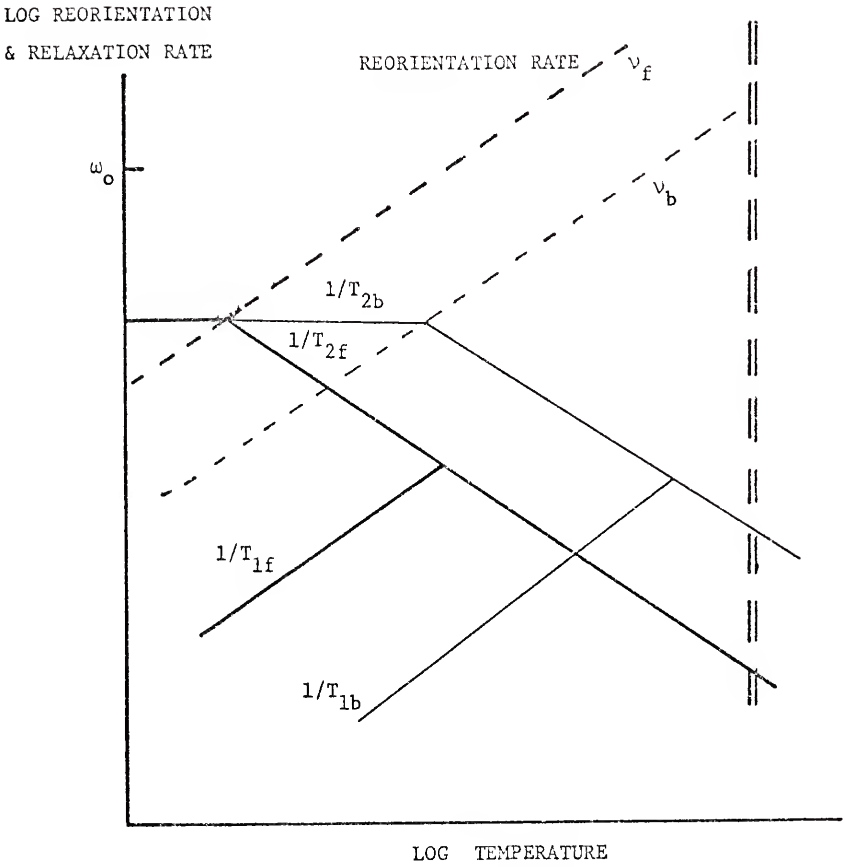

We are envisaging increasing the exchange rate along the line

== == == ==

Fig.(20) The relationship between reorientation (or relaxation) rate of the "bound" and "free" phases and temperature (logarithmic scale)

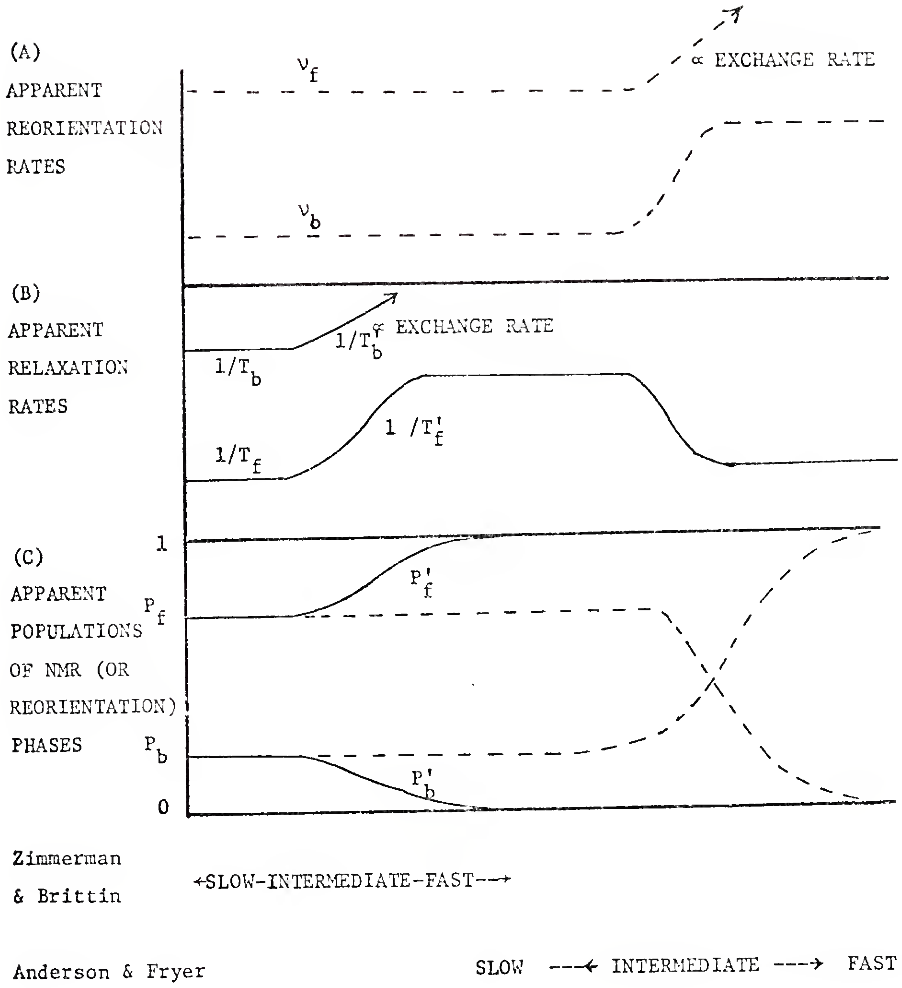

Fig.(21) The effect of exchange rate on (A) apparent reorientation rates, (B) apparent relaxation rates, (C) apparent populations of NMR (or of reorientation) in the "bound" and "free" phases

The core D_2O has only isotropic rotational motion with rate k_1. The bound D_2O molecule has an anisotropic rotational rate k_2. We write the equilibrium

$$D_2O\ (\text{bound}) \underset{k_3}{\overset{k_4}{\rightleftarrows}} D_2O\ (\text{free})\ . \qquad (\text{II}.4.7)$$

The value k_3 is the exchange rate from free deuteron to bound deuteron. The value k_4 is the rate in the reverse direction. We are only concerned with the situation $\omega_o^2\tau^2 \ll 1$, which is true from the argument in the last section. Two limiting cases to be considered are then: (1) the case where the chemical or phase exchange is fast relative to the rotation rate, and (2) the case where the chemical exchange is slow relative to the rotation rate of the free water molecule, i.e., the relaxation rate is limited by the rate of breaking polar bonds.

FAST EXCHANGE: k_3 and $k_4 \gg k_1$ and k_2. This case has been fully treated by Anderson and Fryer[28] with the result:

$$\frac{1}{T_{1,2}} = Q'[(1 + K)/(k_1K + k_2)], \qquad (\text{II}.4.8)$$

and if $k_2 \ll k_1K$, which is a reasonable assumption,

$$\frac{1}{T_{1,2}} = Q'\left(\frac{1}{k_1} + \frac{1}{k_1K}\right). \qquad (\text{II}.4.9)$$

where $K = k_4/k_3$, and

$$Q' = [(3/40)(2I + 3)/I^2(2I - 1)][(1 + \eta^2/3)(e^2qQ/h^2)].$$

We note that the assumption--- $k_2 \ll k_1$ is based on the premise that the Debye-Stokes equation for the rotational correlation time,

$$\tau_r = \frac{4\pi\ \eta' a^3}{3kT} \qquad \text{(II.4.10)}$$

where η'= viscosity and a is a molecular radius, should be obeyed at least approximately. If the relaxation were controled by molecular motion of molecules in bound sites, i.e., $k_2 \gg k_1 K$,

$$\frac{1}{T_{1,2}} = Q'(1/k_2 + K/k_2) \qquad \text{(II.4.11)}$$

SLOW EXCHANGE: k_1 or $k_2 \gg k_3$ and k_4. Anderson and Fryer treated the case for k_1 and $k_2 \gg k_3$ and k_4 but a more general result is needed here because, as noted above, k_2 could be negligibly small. The more general T_1 equation is found to be

$$\frac{1}{T_{1,2}} = Q'\{[K/(1+K)](1+1/k_1) + [1/(1+K)][1/(k_2+k_4)] + k_3/(k_1-k_2)(k_2+k_4)\} \qquad \text{(II.4.12)}$$

which for $k_1 \gg k_2$ reduces to

$$\frac{1}{T_{1,2}} = Q'\{[K/(1+K)](1/k_1) + [1/(1+K)][1/(k_2+k_4)] + k_3/k_1(k_2+k_4)\} \qquad \text{(II.4.13)}$$

The subcases are then, if $k_2 \ll k_4$

$$\frac{1}{T_{1,2}} = Q'[(K/k_1 + 1/k_4)/(1 + K) + 1/Kk_1] \qquad \text{(II.4.14)}$$

and if $k_2 \gg k_3$ and k_4 and K not $\ll 1$,

$$\frac{1}{T_{1,2}} = Q' \left[(K/k_1 + 1/k_2)/(1 + K)\right] \qquad \text{(II.4.15)}$$

which is equivalent to the Anderson and Fryer result.

For $K \ll 1$

$$\frac{1}{T_{1,2}} = Q'/k_2. \qquad \text{(II.4.16)}$$

The plotting of Fig.(22) by Anderson and Fryer is included for future data analysis of the significant T_2 change of the microemulsive D_2O droplets at 57°C. This graph gives the change of relaxation time due to chemical exchange of fast, intermediate and slow passages in the presence of bound water.

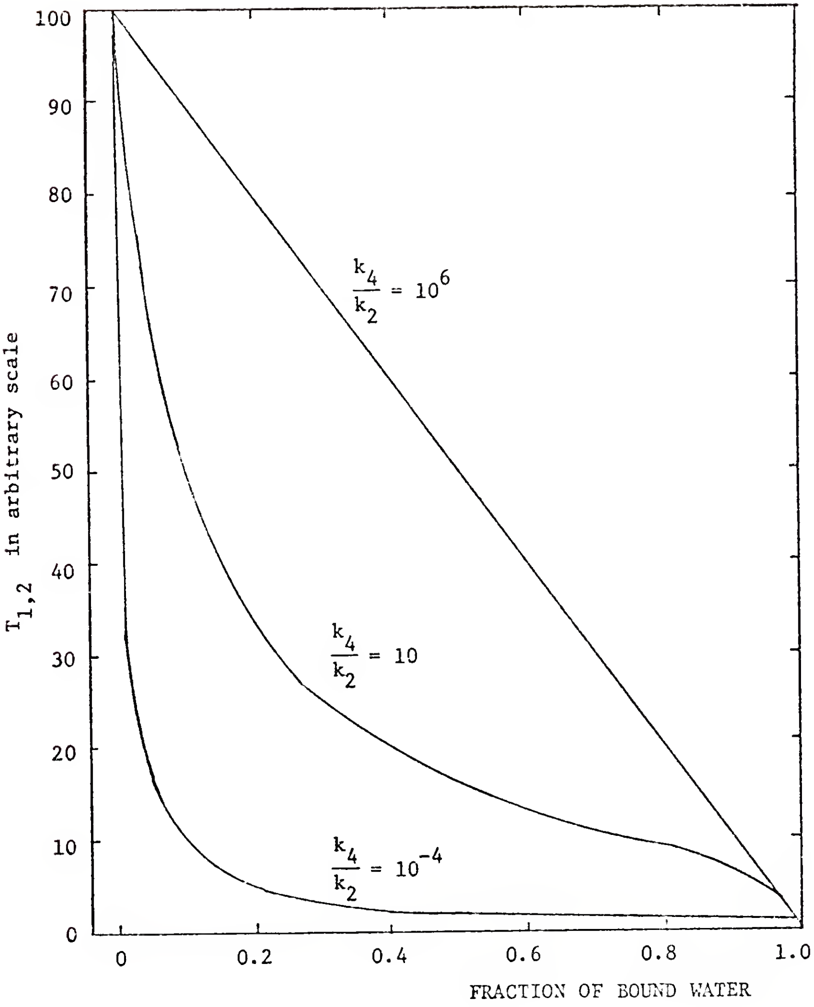

Fig.(22) Change of relaxation time due to chemical exchange of fast, intermediate and slow passages in the presence of bound water [Anderson and Fryer, J. Chem. Phys. 50, 3785 (1969)]

II.5 High Field Theory of Liquid Crystal Powder Pattern

Though the layers of the liquid crystal are ordered within a domain, these domains are distributed randomly throughout the sample. Thus a powder pattern [30][31][32] is obtained. The quadrupole interaction therefore must be weak for the line to be observable in the presence of this broadening. Only first order splitting need be considered in the present case.

$$\mathcal{H} = \mathcal{H}_M + \mathcal{H}_Q \qquad \text{where } \mathcal{H}_Q \ll \mathcal{H}_M \qquad \text{(II.5.1)}$$

$$\mathcal{H}_M = - \gamma\hbar \, H_o \, I_z$$

The $\mathcal{H}_Q$ is given in equation (II.3.1). Since the rotation of the D_2O molecule is fast (about 10^{-12} sec), the electric field gradient of the OD bond is averaged around the molecular axis of symmetry, as seen by the deuteron nucleus. For the isotropic water molecule, the asymmetry parameter η is zero, but is not for an anisotropic water molecule. The anisotropic D_2O molecule has η about 0.1 [25]. This small asymmetry parameter can be ignored in high field theory without causing serious error because, $\eta/2$ appearing in the quadrupole interaction Hamiltonian is much smaller than 1. The nuclear quadrupole interaction Hamiltonian of (II.3.1) is then simplified to the following:

$$\mathcal{H}_Q = A \left(3 I_Z^2 - \vec{I}^2 \right) \qquad \text{(II.5.2)}$$

where A is a constant of known value.

We choose xyz as the strong quantization frame (same as laboratory frame) with the Oz axis parallel to the static field $\vec{H}_o$ and XYZ as the principal axis frame of the electric field gradient. Since the system is cylindrically symmetric, we can choose Oy, OY coincident. Now, we can express I_Z in terms of I_x, I_z and Θ, the angle between the static magnetic field H_o and the principal axis of the electric field gradient of the molecule. This is shown in Fig.(23).

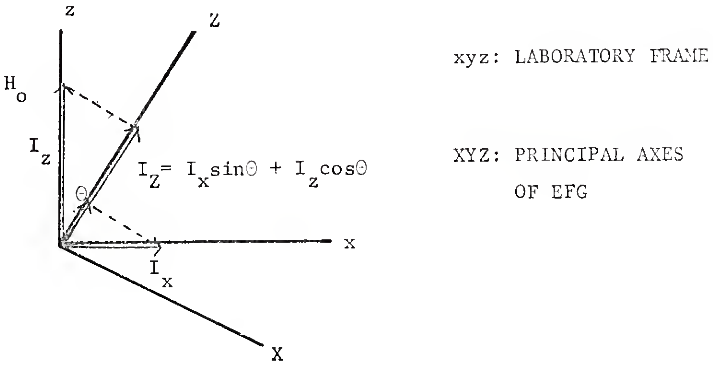
z
Z
H_o
I_z
Θ
$I_Z = I_x \sin\Theta + I_z \cos\Theta$
x
I_x
X
xyz: LABORATORY FRAME
XYZ: PRINCIPAL AXES OF EFG

Fig.(23) Geometry of the electric field gradient principal axes at the deuteron nucleus and the laboratory frame in the liquid crystal

$$I_Z = I_x \sin\Theta + I_z \cos\Theta \qquad \text{(II.5.3)}$$
$$I_Y = I_y$$

Also, I_x and I_y can be replaced by ladder operators I_+ and I_-.

$$I_x = (I_+ + I_-)/2 \qquad \text{(II.5.4)}$$
$$I_y = (I_+ - I_-)/2i$$

Substitute relation (II.5.3) and (II.5.4) into (II.5.2).

$$\mathcal{H}_Q(\text{in laboratory frame}) = \frac{e^2qQ}{4I(2I-1)}\left[\frac{1}{2}(3\cos^2\Theta - 1)(3I_z^2 - I^2)\right.$$

$$+ \frac{3}{2}\sin\Theta\cos\Theta[I_z(I_+ + I_-) + (I_+ + I_-)I_z]$$

$$\left. + \frac{3}{4}\sin^2\Theta\,(I_+^2 + I_-^2)\right] \qquad (II.5.5)$$

The second and third terms do not contribute matrix elements of the diagonal. The first order perturbation contributes only in the case of m = 0, ±1, therefore

$$E_m^{(o)} = -\gamma\hbar H_o m = -h\,\nu_L m \text{ with Larmor frequency } \nu_L = \frac{\gamma H_o}{2\pi}$$

$$E_m^{(1)} = \langle m|\mathcal{H}_Q\,|m\rangle$$

$$= \frac{e^2qQ}{4I(2I-1)}\;\frac{1}{2}\;(3\cos^2\Theta - 1)(3m^2 - I(I+1))$$

$$= \frac{1}{4}\,h\nu_Q(3\cos^2\Theta - 1)(m^2 - I(I+1)/3) \qquad (II.5.6)$$

where $\nu_Q = \dfrac{3\;e^2qQ}{4\;hI(I - 1/2)}$

For the deuteron, I = 1, m = ±1, 0

$$E_1^{(1)} = \frac{e^2qQ}{8}\,(3\cos^2\Theta - 1)$$

$$(II.5.7)$$

$$E_o^{(1)} = -\frac{e^2qQ}{4}(3\cos^2\Theta - 1)$$

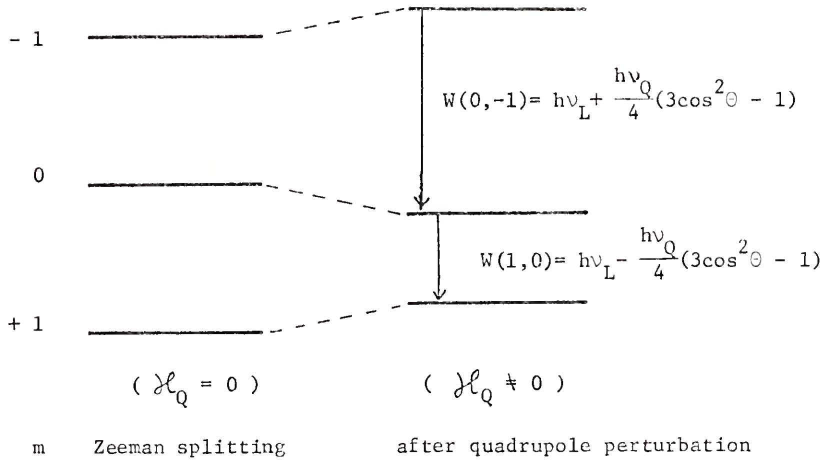
- 1
0
+ 1
$W(0,-1)= h\nu_L + \frac{h\nu_Q}{4}(3\cos^2\Theta - 1)$
$W(1,0)= h\nu_L - \frac{h\nu_Q}{4}(3\cos^2\Theta - 1)$
$(\mathcal{H}_Q = 0)$
$(\mathcal{H}_Q \neq 0)$
m
Zeeman splitting
after quadrupole perturbation

Fig.(24) Energy diagram for first order quadrupole perturbation of the Zeeman effect of the deuteron nucleus

According to selection rules $\Delta m = \pm 1$, the transition energies are given by

$$W(1,0) = -\gamma\hbar H_o + \frac{3}{8}e^2qQ(3\cos^2\Theta - 1)$$

$$W(0,-1) = -\gamma\hbar H_o + \frac{3}{8}e^2qQ(3\cos^2\Theta - 1) \qquad \text{(II.5.8)}$$

Calculation of the spectral shape function, which is a product of the transition probability by the density of transition at each angle Θ , requires the transition probabilities, which we obtain directly from the matrix elements

$$< m \,|I_x|\, m+1 > = \frac{1}{2}\,[(I - m)(I + m + 1)]^{1/2}$$

$$< m \,|I_x|\, m-1 > = \frac{1}{2}\,[(I + m)(I - m + 1)]^{1/2}\,, \qquad \text{(II.5.9)}$$

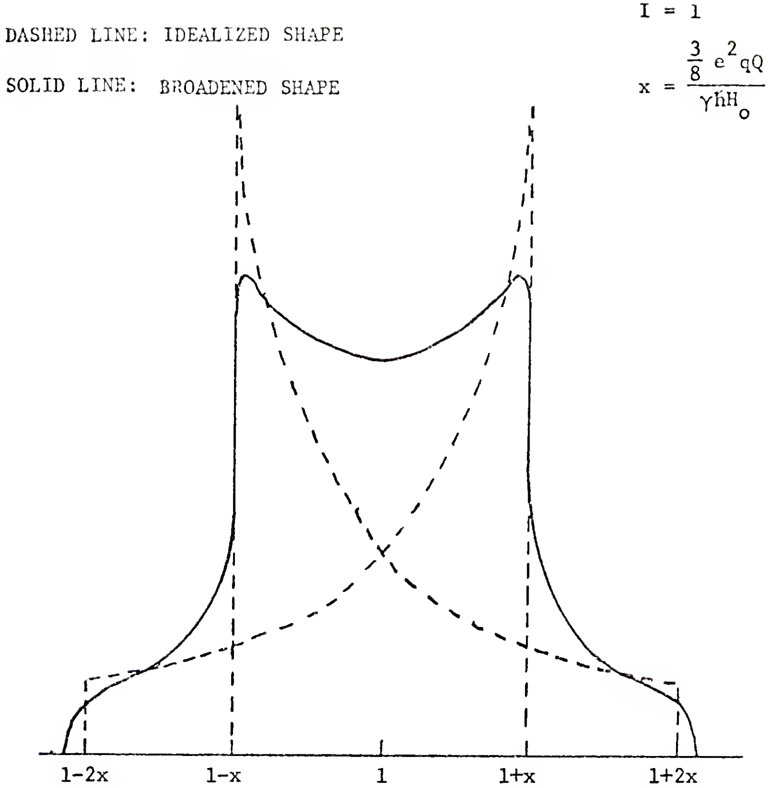

Fig.(25) The powder pattern resonance line for I = 1, corresponding to the transitions $\Delta m = \pm 1$, in a strong magnetic field, as a function of the transition energy. The ordinate unit is arbitrary. The nuclear quadrupole interaction is treated as a first-order perturbation of the NMR transitions. The figure corresponds to a nuclear magnetic resonance experiment in which the strong magnetic field is held constant, while the oscillating frequency is swept through the resonance.

therefore,

$$P(1,0) \propto \left|< 1 \right| -2H_1\cos\omega t\ \gamma\hbar\ I_x \left| 0> \right|^2 = 2\gamma^2\hbar^2H_1{}^2\cos^2\omega t \qquad \text{(II.5.10)}$$

$$P(0,-1) \propto \left|< 0 \right| -2H_1\cos\omega t\ \gamma\hbar\ I_x \left| -1 > \right|^2 = 2\gamma^2\hbar^2H_1{}^2\cos^2\omega t\ .$$

The value P is independent of θ. Thus, the shape function for the transition depends on θ only through the density of transition D at angle θ. For an isotropic distribution all orientations are equally probable and the number density of nuclei for a given orientation varies as

$$\begin{aligned} D(\cos\theta) &= \frac{d\ \cos\theta}{d\ W} \\ &= \left(\frac{d\ W}{d\ \cos\theta}\right)^{-1} \\ &= \frac{e^2qQ}{16}\left(\frac{W \pm \gamma\hbar H_o}{\frac{3}{8}\ e^2qQ} + 1\right)^{-\frac{1}{2}} \end{aligned} \qquad \text{(II.5.11)}$$

The ± signs in the parenthesis depend on which one of W(0,-1) and W(1,0) is chosen for W. The final line shape is determined by superposing the shape functions of both transitions.

The idealized shape shown in Fig.(25) by the dashed line has certain striking features. For values of W corresponding to cosθ = 0, the denominator of the shape function vanishes and the line strength becomes infinite. It is also to be noted that the outsides of the lines are very sharp, while, on the inside, the lines merge. Observed spectra shown by solid line, may be expected to be differ from this idealized shape, because of various broadening mechanisms, such as lifetime and dipolar broadening. In addition, the effect of second order quadrupole perturbation terms, which were disregarded in our discussion of the line shape-will distort the shape of the line and shift the positions of the minimum-without, however, changing the distance between them.

The average quadrupole coupling constant of the deuteron nucleus in D_2O has the magnitude 258.6 kHz measured by Hindman[25].

The simple bound water model of lamellae structure is shown in figure(26). If the water layer has a thickness d=100 Å and the bound water a thickness with prefered orientation Δ=1.25 Å, the observed quadrupole constant can be calculated from the relation

$$< \frac{e^2qQ}{h} >_{obs.} = 258.6 \text{ kHz} \times P_b + 0 \times (1 - P_b) \qquad (II.5.12)$$

Only bound deuteron water contributes to the quadrupole splitting. The weighting factor P_b for bound water [33], is equal to $\Delta/d = 1.25\text{x}10^{-2}$. The unbound deuteron water with fast tumbling frequency (on the order of 10^{12}Hz, is much faster than the Larmor frequency) has no contribution due to quadrupole splitting. There numbers give

$$< \frac{e^2qQ}{h} >_{obs.} = 3.23 \text{ kHz} \qquad (II.5.13)$$

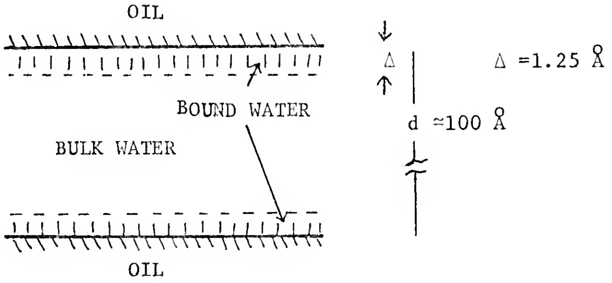

Fig.(26) The bound water model of lamellae structure(bound water has prefered orientation)

CHAPTER III EXPERIMENTAL METHOD AND PROCEDURE

III.1 Sample Preparation

III.1.1 Preparation of Chemicals

The chemicals used in this research, their purities, molecular weights, and the commercial source are listed below:

Table(4) Components used for sample preparation

Name of Component	%Purity	Molecular Weight	Supplier
Deuterium Oxide (D_2O)	99.8	20	Stohler Isotope Chemicals
Oleic Acid ($C_{18}H_{34}O_2$)	95	282	Fisher Scientific Co.
Potassium Hydroxide (KOH)	85.9	56	Fisher Scientific Co.
1-Hexanol ($C_6H_{14}O$)	99	102	Fisher Scientific Co.
n-Hexadecane ($C_{16}H_{34}$)	99	226	Fisher Scientific Co.
1-Pentanol	99	88	Fisher Scientific Co.

Potassium oleate is prepared by mixing equimolar amounts of potassium hydroxide and oleic acid. Since solid potassium hydroxide does not readily react with oleic acid, the latter is mixed with the other three components(D_2O , hexanol and hexadecane) in the desired ratio first and then with potassium hydroxide. The physical properties of the dispersed system studied are highly sensitive to change of potassium oleate.

Since potassium hydroxide rapidly absorbs water vapor and the amount of it used is small, it was necessary to quickly and precisely measure the weight so that negligible vapor is absorbed during weighing. The resolution of the balance is about 10^{-4}gram.

The samples are labeled by W/O, the volume ratio of deuterium oxide to hexadecane oil, and by S/O, the ratio of surfactant potassium oleate in grams to hexadecane oil in cm^3. All the samples have a fixed ratio of the cosurfactant hexanol or pentanol to hexadecane oil of 0.4 by volume.

The prepared samples are listed in the following:

Hexanol system (S/O= 0.2) W/O = 0.1, 0.2,0.3, 0.4, 0.5, 0.6, 0.7, 0.8
1.0, 1.2, 1.4, 1.6, 1.8, 2.1
Pentanol system (S/O= 0.2) W/O= 0.1, 0.2, 0.4, 0.6, 0.8, 1.0, 1.2, 1.4

Other samples were prepared with changing surfactant/oil ratios and a fixed W/O ratio. Unfortunately most of them were not stable and had a separation problem during the time of the experiment. These samples were all rejected.

III.1.2 Sample Sealing

Since the sample is a mixture of liquids, small amount of dissolved oxygen molecules, which is a paramagnetic impurity having a net magnetic moment arising from unpaired p electrons [34][35] roughly 10^3 times larger than that of the deuteron, cause a significant contribution to the relaxation process. In order to exclude the oxygen molecules, standard freeze-pump-thaw method was employed. Using the low solubility of the oxygen molecules at cold temperature, we can freeze the sample with liquid nitrogen first and then pump to evacuate. The next step is to thaw the sample to release the remainder of the oxygen molecules. Repeat this method for two cycles and then seal it. This procedure represents a compromise. Prolonged freeze-pump thaw cycles may well cause composition changes.

The sample container is a Pyrex tube with an inner diameter of 1 cm and an outer diameter of 1.22 cm. The length of the sample tube is about 3 cm. Before filling with sample, the tubes were cleaned by aceytone and dried. Sample tubes were prepared by drawing to a narrow neck and annealing with a moderate flame. During sealing, caution was exercised to heat the sample, otherwise the chemicals may evaporate or dissociate even though most of the sample tube was submerged in liquid nitrogen.

III.2 Temperature Measurement and Controlling Apparatus

III.2.1 Cryostat

The cryostat is shown in Fig.(27). After locating the sample in the rf coil, the inner copper and intermediate brass chambers are sealed with an indium wire O-Ring of 0.025" diameter. Helium exchange gas of about 5 psi is admitted to both chambers. Though the helium exchange gas in the brass chamber was latter pumped out, it is important to do this to expell water vapor; otherwise the water vapor attached on electric wire may cause current leaking especially when the temperature was below ice point.

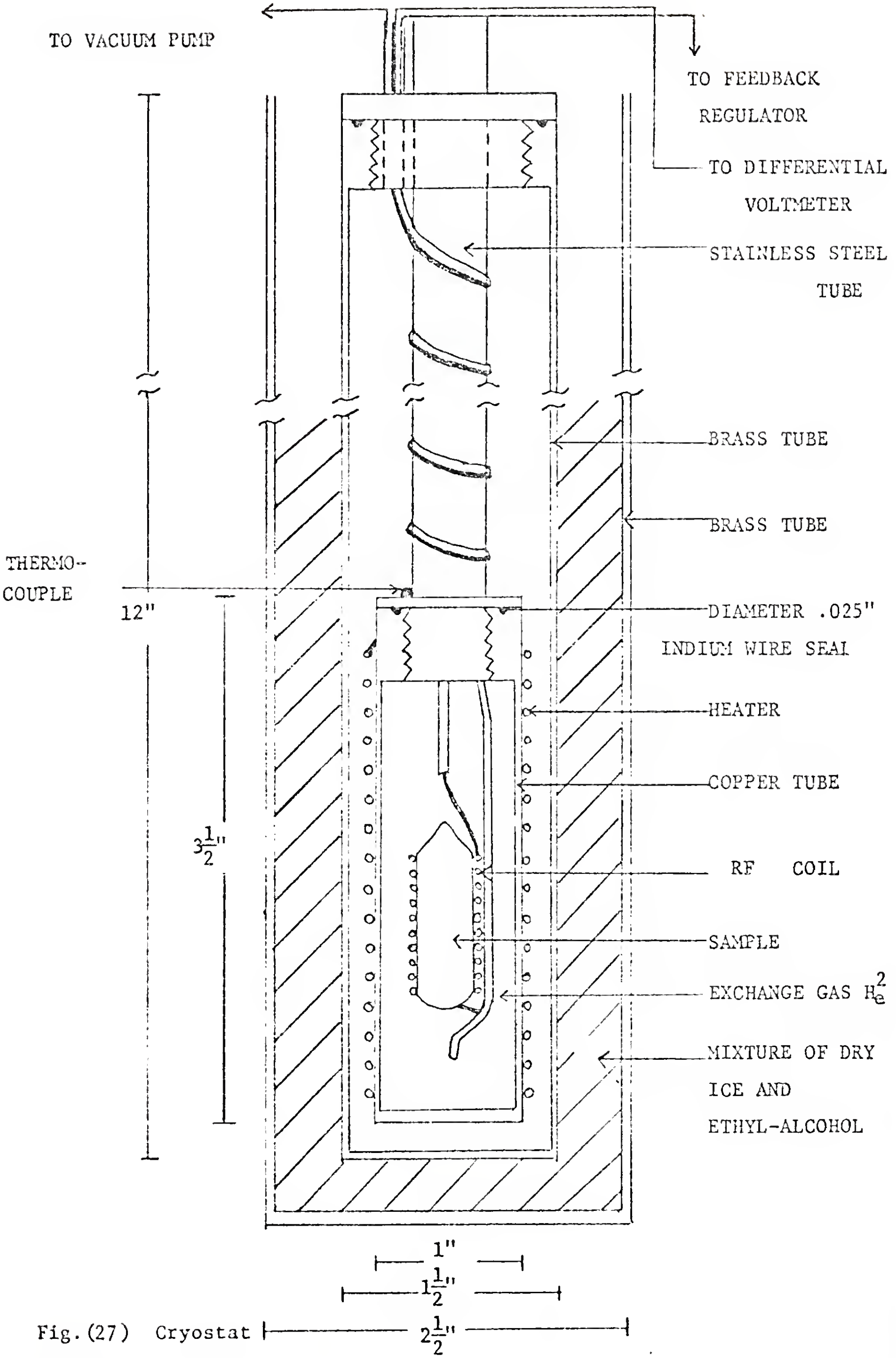

Fig. (27) Cryostat

For experiments below room temperature, a mixture of powdered dry ice (solid CO_2) and ethylalcohol is admitted to the outside brass cylinder. Ethylalcohol guarantees good temperature uniformity of the heat reservoir at -77^oC. Then, the helium gas between the intermediate brass and inner copper chamber is pumped out to a pressure of 10^{-4} torr or less by a two-stage vacuum pump. Even though the pressure is low and brass is a poor thermal conductor, slow heat exchange between the sample and environment is still possible. This slow heat exchange facilitates proper cooling of the sample. The copper chamber has excellent thermal conductivity, thus the rate of heat exchange between heater and the sample is much faster than that between environment and sample. The thermocouple and heater are connected to the feed back regulator discussed in the following sections.

III.2.2 Thermometer

A copper-constantan thermocouple was used as the thermometer, and is located at the top of inner copper chamber [Fig. (27)]. A mixture of crushed ice and water was used as reference at 273.16^oK. Every 43 μv thermovoltage corresponds to one degree of temperature difference from the reference point. In order to obtain identical temperature of the copper chamber and the sample, measurements should be made during heating and cooling parts of any thermal cycle. The time needed for temperature equilibrium and removal of the temperature gradient across the sample varies from 5 to 30 minutes depending upon the temperature difference between initial and the final states and the rate of heat exchange between the sample and the environment.

III.2.3 Feedback Regulator

A feedback regulator is used for maintaining the sample at constant temperature. Figure(28) shows the block diagram of the feedback regulator. The three amplifiers in the system, namely the FLUKE 823 AR DC-AC differential voltmeter, the DYMEC 2460 MI amplifier and the Hewlett-Packard 467A power amplifier, give large multifold gain of approximately 10^3 so that even a small difference between the temperatures of the sample and control value is sensitive enough to generate a considerable quantity of additional heat. The actual and desired thermal potential difference between the sample and reference ice-water mixture may be expressed as $k\Delta t$ and is compared with a voltage E_s. The value V_B generated by KEPCO power supply (voltage regulated) series with power amplifier HP 467A. The difference voltage is amplified to produce an output $A(E_s - k\Delta t)$. It is necessary to operate the amplifier in a slightly unbalanced condition so that positive and negative excursion of the sample temperature from the desired value can be compensated by decreased or increased heater power. If operated strictly a balance, positive and negative voltage at the output would both produce heat in the sample.

The unbalance is produced by the insertion of a "DC" power supply V_B generated by the KEPCO in series with the balanced HP 467A. Even so if the output of the amplifier is sufficiently negative the system will become unstable, a high temperature will generate a greater negative voltage $(k\Delta t - V_B)$, and a greater negative current will flow through the heater. Insertion of a suitable diode prevents the negative current flowing.

The value R_H is the resistance of the sample heater. The distinguishable temperature differentiation Δt is about $0.25^\circ C$.

If $E_s - k\Delta t > 0$ The heater current turned on and the sample heated up.

$E_s - k\Delta t < 0$ The heater current is terminated by a diode between the HP 467A and KEPCO, and the sample is cooled down.

The required value of V_B is such that V_B^2/R_H is larger than the cooling rate between the sample and environment at the desired temperature. The regulating procedure are listed below

(1) Set E_s a little larger than $k\Delta t$, the real potential developed in the thermocouple, then one will see current through ammeter.

(2) Increase the gain but not sufficiently that the current exceeds the maximum current that the heater can tolerate.

(3) Adjust V_B to obtain a null current in ammeter, i.e. the ammeter is balanced. This provides proper cut down current.

(4) Set E_s to the desired value, and the system will regulate.

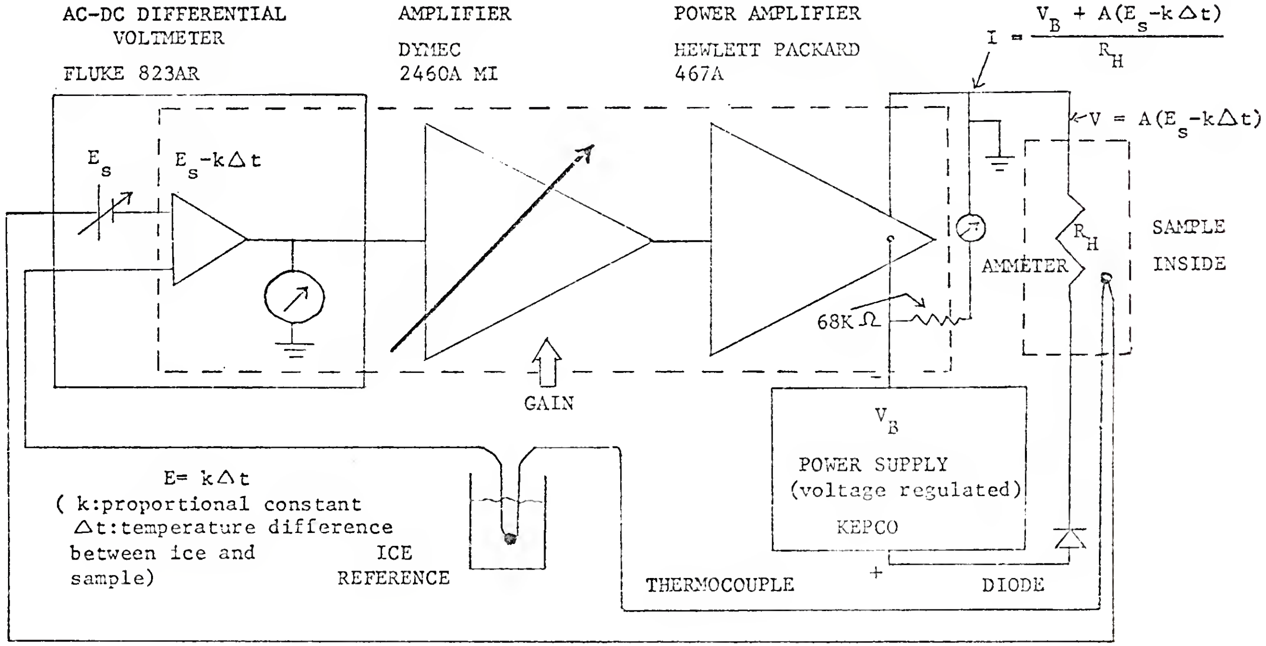

Fig.(28) Block diagram of Feed-Back Regulator for temperature control of the sample

III.3 Nuclear Resonance Measuring Apparatus

III.3.1 Circuit Description

Figure(29) shows a block diagram of the probe and associated major components. The output impedance of the transmitter is matched to the transmission line and is equal to the input impedance of the receiver. The impedance at resonance of the sample tank circuit is also equal to that of the transmission line.

The operation of the system depends upon the nonlinear properties of semiconductor diodes. During the application of a high-powered rf pulse from the transmitter, both sets of crossed diodes in Fig.(29) are conducting heavily and have low impedances. Thus, the rf pulse passes through the diodes at A without appreciable attenuation, while the diodes at B prevent the rf level at the receiver input from rising above 1 v. Since point A is a quarter wavelength from B, the effective short circuit at B appears as an open circuit at A and thus does not affect the voltage at A.

Following the rf pulse and after the transients have decayed, the diodes stop conducting and the series crossed diodes prevent a large impedance at point A. The small NMR signal voltage (typically about 1 mv) is not enough to lower the impedance of the diodes, and thus in the absence of an rf pulse the transmitter is isolated from the system, while the receiver is matched to the sample tank circuit.

It should be observed that the length of the $\lambda/4$ line between points A and B is not specially critical, as the purpose of this line is to allow the use of the diode short at B without presenting a low impedance shunt at the sample coil. Thus, since the transformed

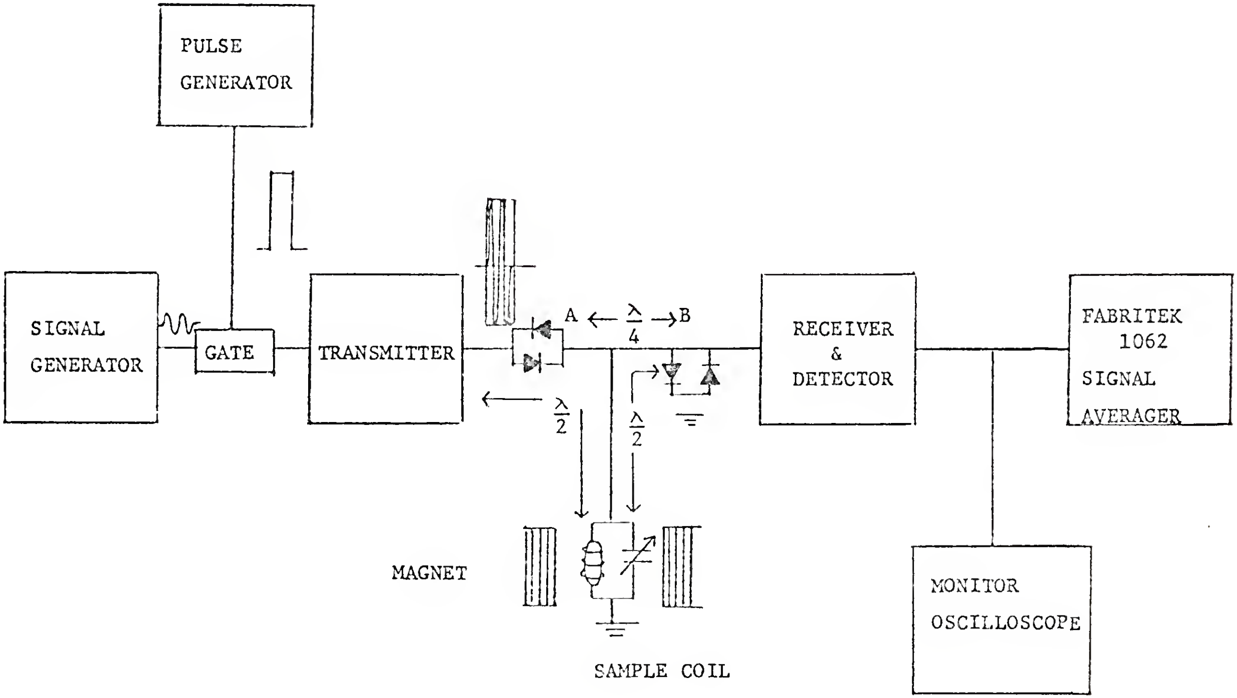

Fig.(29) Simple block diagram for pulsed NMR experiment impedance of the diode short need only be large compared with 50 Ω, within the bandwidth of the tuned sample coil, the cable need only be of the order of λ/4, and the use of the quarter wave cable does not entail any significant narrow-banding of the system.

A more detailed block diagram is given in Fig.(30). The rf signal generator (HP 606B) is stabilized by a HP 8708A synchronizer. High voltage pulses are provided by an ARULAB PG-650C oscillator. A programmed pulse generator (Wang Lab. 612AT) controls the width of pulses and the delay time τ between pulses. The resonance frequency, pulse width, and the delay time can be checked using the model 729C universal time counter. Transient signal picked up from the sample coil after preamplification (the wide band amplifier serves as power source for the preamplifier) is sufficient to feed the phase sensitive detector (1-30 MHz F+H Instruments) about 0.5 v. However, in the case of spin-echo measurement of T_2 the stability of the electromagnet was not adequate to use phase sensitive detection, and diode detection was employed. This arrangement is shown in Fig.(31). Signals from the phase sensitive detector were accumulated in a Fabritek 1062 signal averager, whence the resultant could be plotted on an X-Y recorder (Honeywell 550).

III.3.2 Electromagnet

This is a Varian V-3454, 9-inch diameter, Fieldial-regulated unit, equipped with cooling system. The drift of the magnet is less than 240 parts per million of maximum field over one day when operated continuously. In other words, this is the dominant source of error in the maintainance of the resonance condition. The frequency stability of the signal generator used is 2×10^{-6} per day.

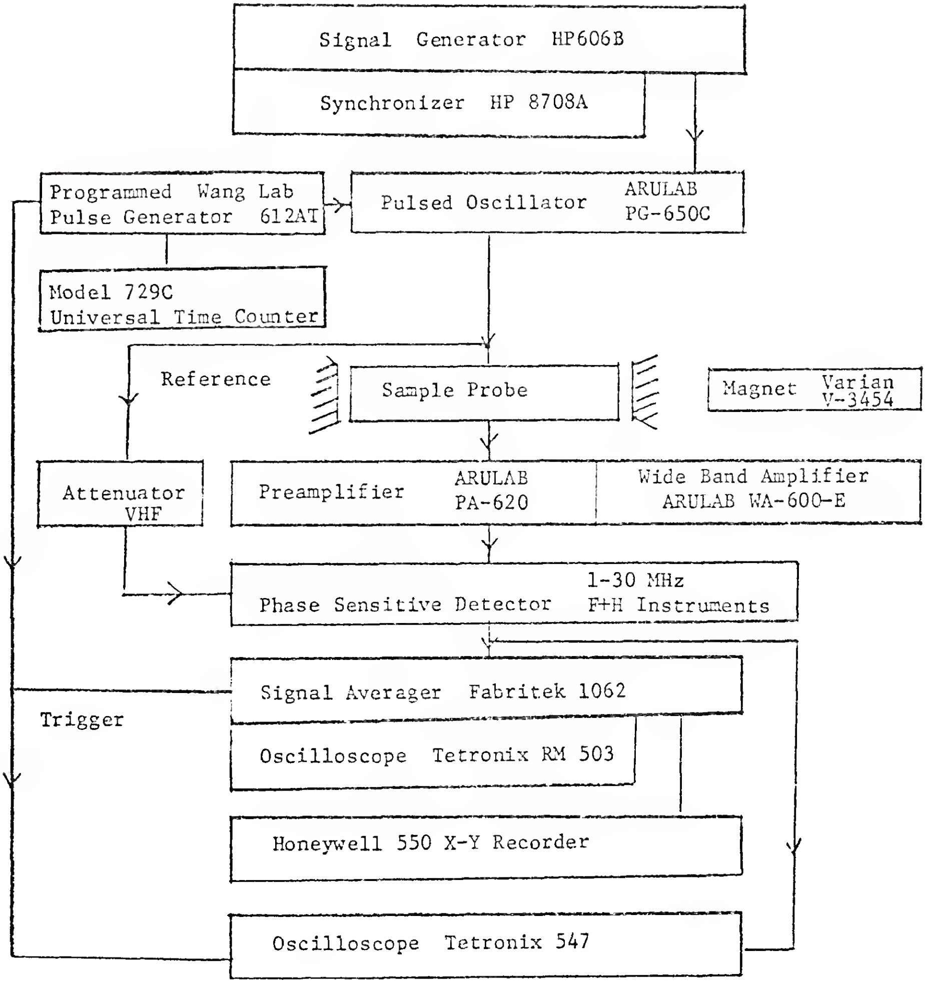

Fig.(30) Block diagram of pulsed NMR experiment with phase sensitive detector

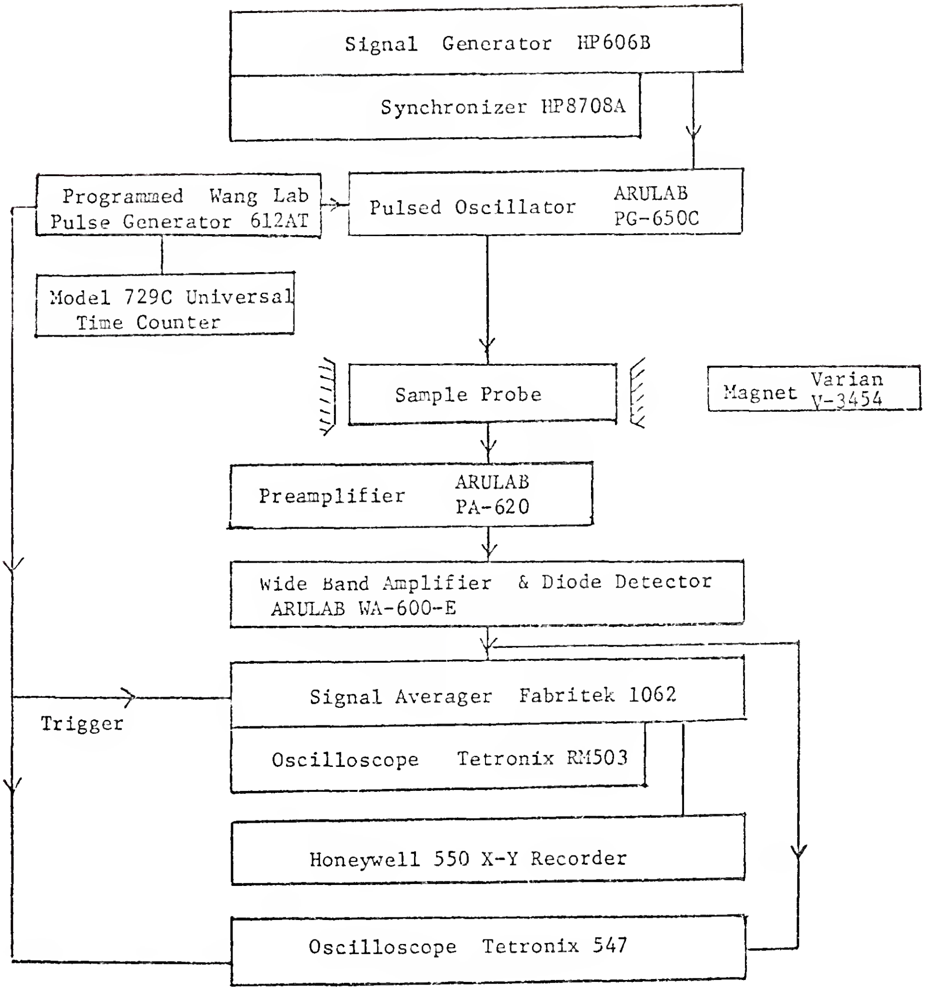
Signal Generator HP606B
Synchronizer HP8708A
Programmed Wang Lab Pulse Generator 612AT
Pulsed Oscillator ARULAB PG-650C
Model 729C Universal Time Counter
Sample Probe
Magnet Varian V-3454
Preamplifier ARULAB PA-620
Wide Band Amplifier & Diode Detector ARULAB WA-600-E
Signal Averager Fabritek 1062
Trigger
Oscilloscope Tetronix RM503
Honeywell 550 X-Y Recorder
Oscilloscope Tetronix 547

Fig.(31) Block diagram of pulsed NMR experiment with diode detector.

III.3.3 Signal Generator and Frequency Synchronizer

The signal generator is a Hewlett-Packard Model 606B unit, which provides a signal adjustable from 0.1 microvolt to 3 volts and which is applied to a 50 ohm resistive load.

The frequency synchronier is a Hewlett-Packard Model 8708A, which is designed to phase-lock the HP 606B signal generator.

III.3.4 Pulse Programmer and High Power Gated Amplifier

The pulse generator is a Wang Model 612 AT transistorized programmed pulse generator. This unit has two independent channels, each capable of delivering twelve pulses which are collectively adjustable in duration and timing as follows: the pulses in the first direct channel can be programmed at any or all of the first twelve equally spaced time marks established by an internal timing source; the pulses in the second delay channel can likewise, except that in addition the channel as a whole can be delayed with respect to the timing source. Since the period of the timing source is adjustable, a flexible pulse program is available. This unit has several disadvantages: The change of delay time affects the pulsing rate. There are only twelve delay pulses available for a Carr-Purcell sequence. Finally, the output impedance is fairly high, and the output voltage level of 10 volts maximum is marginal for the requirements of the transmitter. The last disadvantage is overcome by inserting a high power rf amplifier.

The high power rf amplifier is a Arenberg Ultrasonics Laboratories Instrument Company Model PG 650-C pulsed oscillator. The unit receives the rf signal from the rf signal generator, together with gate rectangular pulses from the pulser. The transmitter delivers a maximum rf amplitude of about 300 volts into 50 ohms.

III.3.5 Sample Coil and Probe

The sample coil consists of 16 turns of No.22 double cotton copper wire with a total inductance of 17μh.

The probe (including sample coil) serves as part impedance matching network to the transmitter and receiver. The capacitors of the probe, C_1, C_2, and C, are tuned so as to maximize the observed signal. The circuit diagram is given in Fig.(32).

III.3.6 Receiver

The preamplifier used is an ARULAB Model PA-620-L. This is a tuned amplifier, which provides voltage gain of approximately 60 db with a low noise figure. The output and input stages each has nine tuning coil caps. These are used to balance the capacitance existing between grid and plate of the vacuum tubes and thus limit the recovery time and optimize the system [Fig.(33)]. The frequency selectors must obviously be set in the proper range for sample resonance. The bandwidth selector can be used to adjust the resistance between grid and ground so that high gain with narrow bandwidth or low gain with broad width can be obtained depending on the frequency distribution of the sample signal. The well tuned narrowest bandwidth is about 200 kHz, which is wide enough for the quadrupole perturbation frequency range found in these studies.

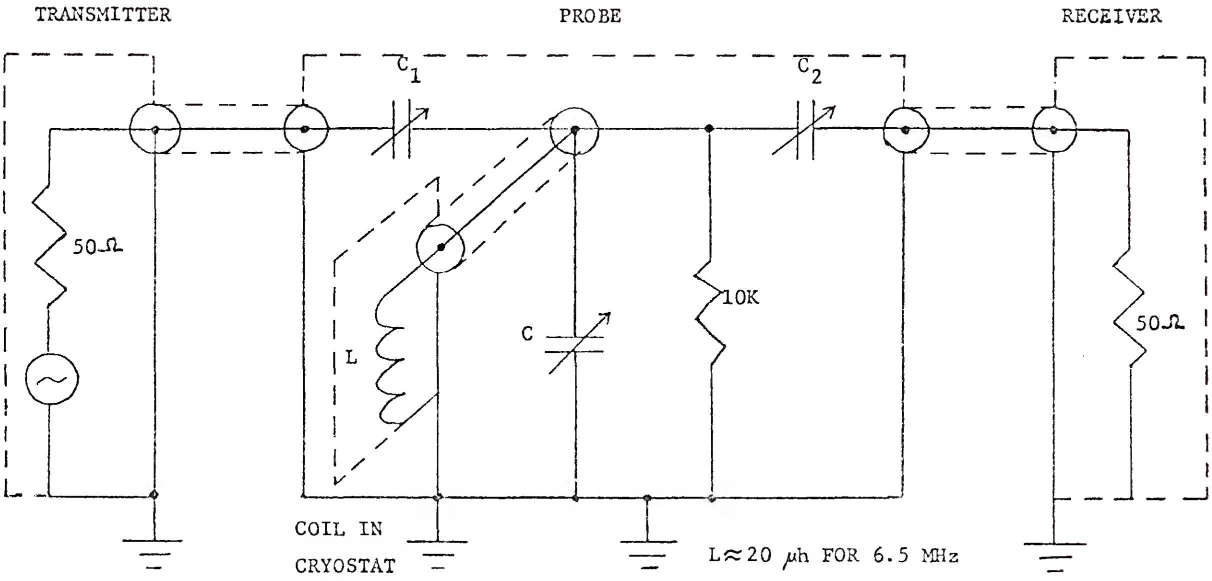

Fig. (32) Probe network

L ≈ 20 μh FOR 6.5 MHz OPERATION

$C_1, C_2 \approx 1 \sim 10$ pf

$C \approx 10 \sim 100$ pf

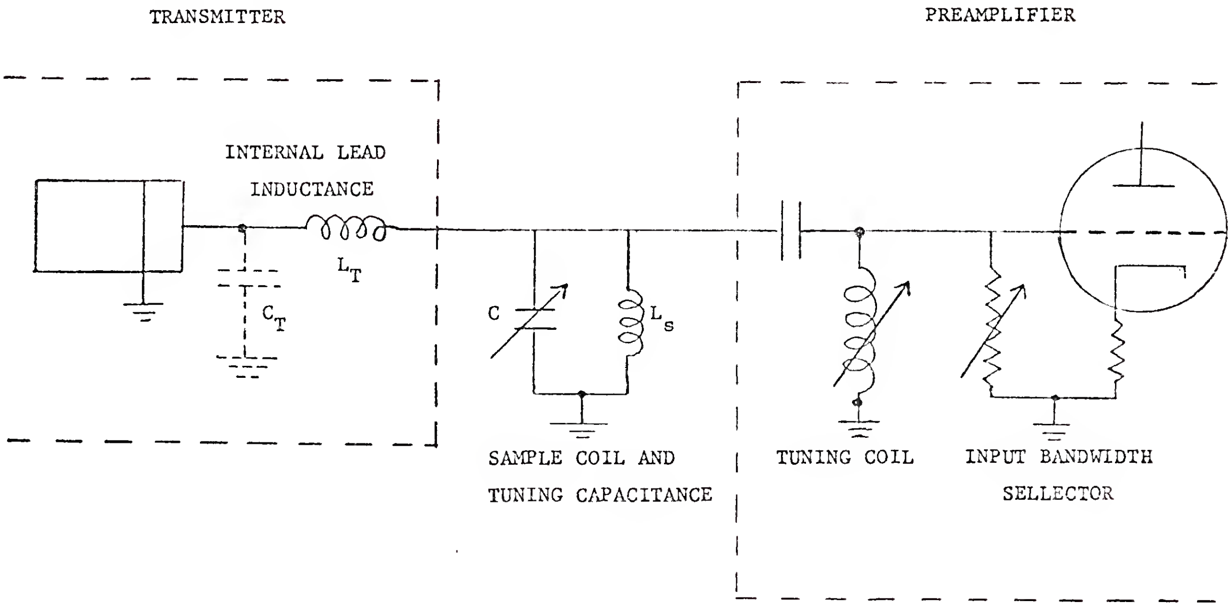

Fig.(33) Simple diagram for tuning of preamplifier

An ARULAB Model WA 600 E Wide Band Amplifier follows the preamplifier PA-620-L. This unit has an rf gain of about 60-65 db, flat to within +3db from 2 to 65 MHz.

The dead time is about 1.5 x 10^{-4} sec. The gain of the preamplifier is about 180 and the total rf gain of the receiver is about 10^{5}.

III.3.7 Phase Sensitive Detector

The following is a qualitative description of the ring diode phase sensitive detector. For a more rigorous treatment reference should be made to Arundell,L.,Clarendon Laboratory, Oxford memo.

The assumption is made that $V_R >> V_s$ and that the diodes when forward biassed have a resistance R and when reverse biassed have an infinite impedance.

Following the nomenclature of Fig.(34) in the half cycle when $V_B > V_D$ the circuit becomes

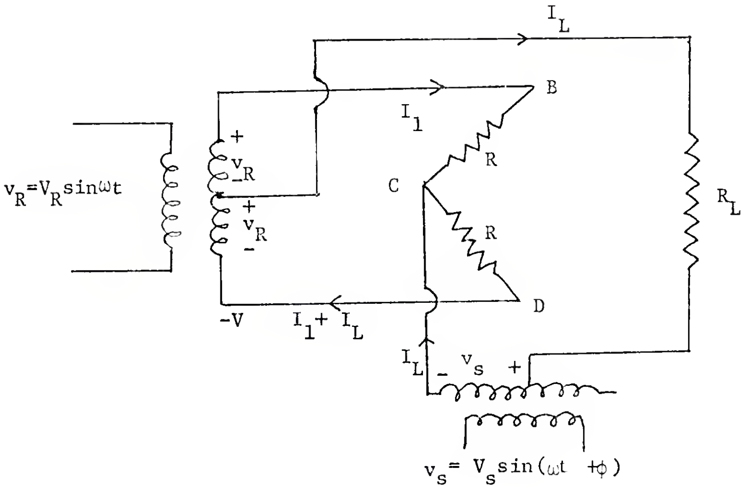

Applying Kirchoff's Laws,

$$2\ v_R = I_1R + (I_1 + I_L)\ R = 2\ I_1R + I_LR \qquad \text{(III.3.7.1)}$$

$$v_R - v_s = I_LR_L + (I_1 + I_L)\ R = I_1R + 2\ I_LR \qquad \text{(III.3.7.2)}$$

$$\therefore\ -2\ v_s = 3\ I_LR \quad \text{or} \quad I_LR = -\frac{2\ v_s}{3} \qquad \text{(III.3.7.3)}$$

In the other half cycle

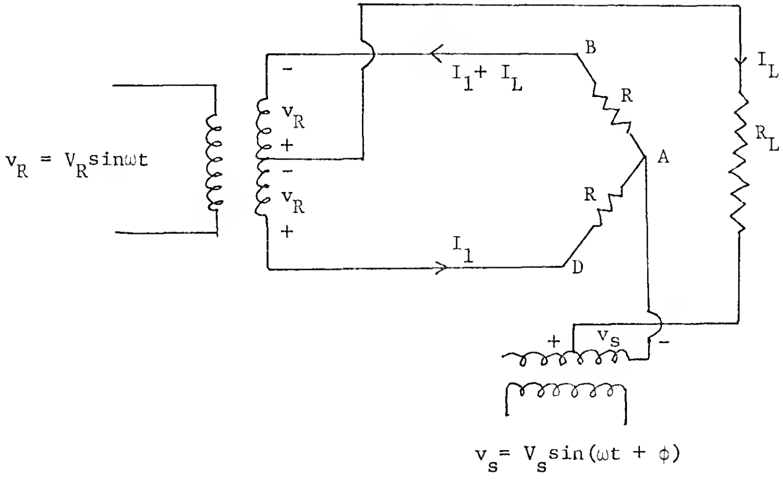

As before

$$2\ v_R = I_1R + (I_1 + I_L)\ R = 2\ I_1R + I_LR \qquad \text{(III.3.7.4)}$$

$$v_R - v_s = I_LR_L + (I_1 + I_L)\ R = I_1R + 2\ I_LR \qquad \text{(III.3.7.5)}$$

and $$-2\ v_s = 3\ I_LR \quad \text{or} \quad I_LR = -\frac{2\ v_s}{3} \qquad \text{(III.3.7.6)}$$

v_R: solid line

v_s: dashed line

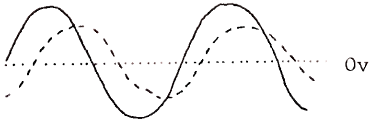

Output = $I_L R_L$

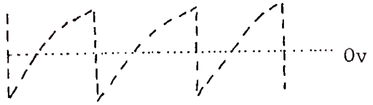

If the assumption is made that the switching is done by v_R the putput is proportional to

$$\frac{1}{\pi} V_s \int_0^{\pi} \sin(\theta + \phi)\, d\theta$$

$$= \frac{V_s}{\pi} \left[\cos\phi \int_0^{\pi} \sin\theta\, d\theta \;+\; \sin\phi \int_0^{\pi} \cos\theta\, d\theta \right]$$

$$= \frac{2}{\pi} V_s \cos\phi \qquad \text{(III.3.7.7)}$$

There may be a portion of the cycle when v_s exceeds v_R and at that time diodes CB and BA may conduct whilst CD and DA are switched off or vice versa depending upon the sign of v_s. The treatment is also neglecting non-linearities in the diode characteristic.

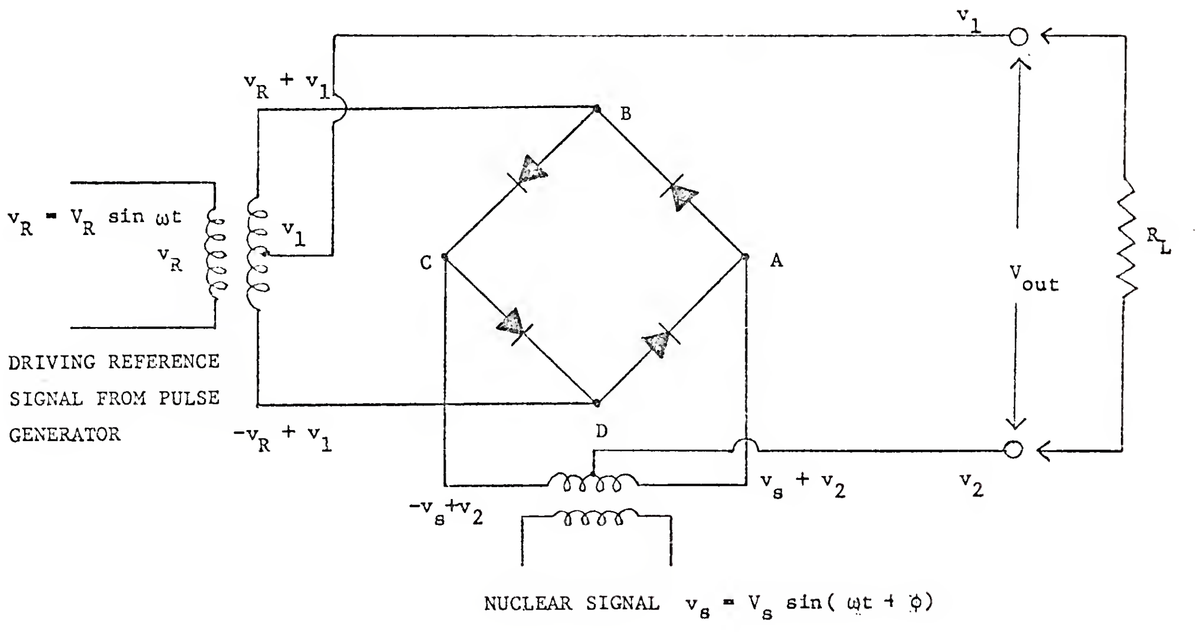
v_1
$v_R + v_1$
B
$v_R = V_R \sin \omega t$
v_1
v_R
C
A
V_{out}
R_L
DRIVING REFERENCE SIGNAL FROM PULSE GENERATOR
$-v_R + v_1$
D
$-v_s + v_2$
$v_s + v_2$
v_2
NUCLEAR SIGNAL $v_s = V_s \sin(\omega t + \phi)$

Fig.(34) Phase detection

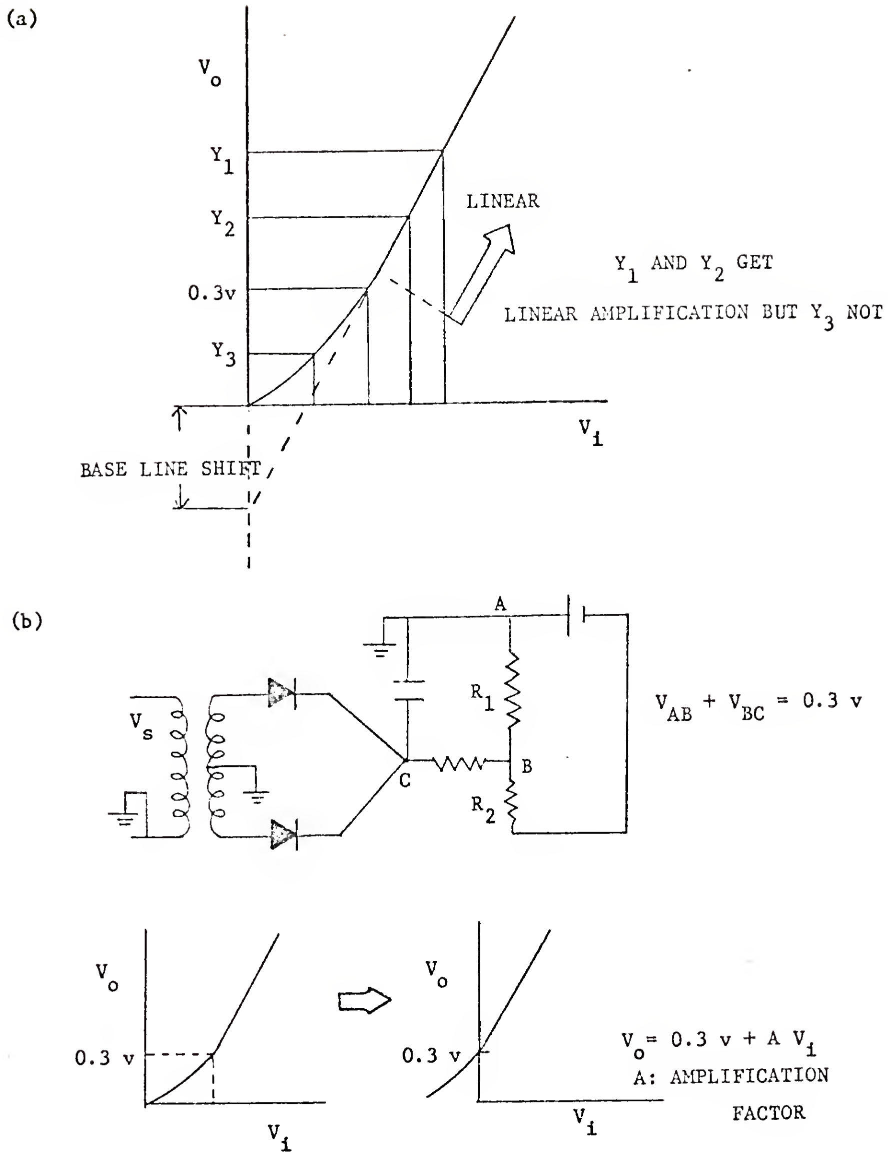

Fig. (35) (a) Nonlinear characteristic of a diode
(b) Modified circuit for diode detector

III.3.8 Diode Detector

The idea of amplification of diode detector comes from linear part of the diode characteristic of the current-voltage relation in a semiconductor.

The input signal V_i and output signal V_o characteristic of a diode is shown in Fig.(35a). In the case of small V_i, V_o the amplification V_o/V_i is reduced. This causes distortion on small spin echoes and gives a smaller T_2 than the true value. The modification of the diode detector is given in Fig.(35b).

For the system used in this dissertation study, an additional 0.3 volt reverse bias is applied to push the characteristic toward the left so that a linear amplification is obtained.

Since the diode has rectification property, the information collected gives only the magnitude. Thus the signal averager (Fabritek 1062) only accumulates positive input and fails to average out random noise. In Fig.(36), the basic structure of a diode detector is shown. The voltage V is used to shift the signal level.

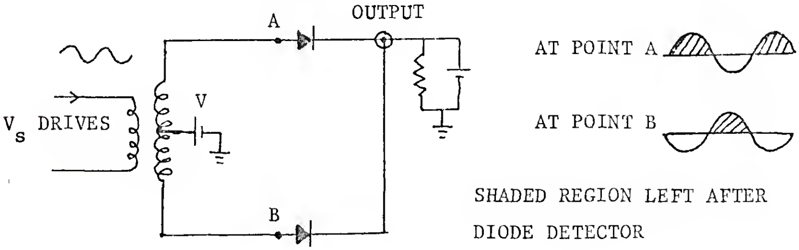

Fig.(36) Diode detection

A diode detector is also inferior in tuning. The resonant frequency is determined by mixing a reference signal (from the pulse generator) through an attenuator with the nuclear signal. The attenuator is used to shift the level of the signal to reduce the base line offset. When tuned off resonance, there are beats on the free induction decay. One can tune either field or rf frequency to remove this ripple thereby ensuring that the resonance condition is fulfilled. When making the measurements, reference signal is removed.

In diode detection, the requirement of stabilities for field and rf source are not as critical. Spin-spin relaxation times obtained from diode detection was generally smaller by about 30 % than that obtained from Gill-Meiboom-Carr-Purcell[36] pulse sequence phase detection.

III.4 Continuous Wave Method

A Varian DP-60 Wide Line spectrometer was used to record the narrow line of the liquid crystals and microemulsions. The wide line of the liquid crystals contributed by the deuteron quadrupolar splitting of the bound D_2O was also recorded by saturating the central narrow line.

III.4.1 Power Saturation and Line Width Broadening

Figure(37) shows the relation of signal to H_1(magnitude of rf field) and H_m(magnitude of audio modulation field). We will see diagram (a) and (b) being both similar. At low H_1 and H_m values the signal height is proportional to H_1 and H_m, but at high values saturation occurs followed by a decrease in signal amplitude.The corresponding line width is no longer a constant, being broadened by instrumental reasons. To avoid such saturation problem, one should check the magnitude of saturation field before running each sample and set both rf and audio field magnitude by 50 % below. When phase detected at the modulation frequency, the familiar derivative spectrum is observed. This applies to the frequency ω_m is less than the linewidth expressed in frequency unit.

In the severe saturation a series of sidebands are produced at $\omega_o \pm\omega_m$, $\omega_o \pm 2\omega_m$ etc.[Fig.(38)]. The effective H_1 at the sideband frequencies is affected by H_m and can be expressed as H_1 multiplied by a scaling factor. The scaling factor is a Bessel function of parameter ($\beta = \frac{\gamma H_m}{\omega_m}$) [37]. Figure (39) shows that increasing H_m requires higher H_1 to obtain the same signal height. In other words, smaller signal height is obtained if H_m is increased and H_1 is kept fixed. (Note: This is true for the central band but not for the sidebands, which will be discussed in next section.)

For the first sideband detected at the modulation frequency

$$H_1^{effective} = H_1 \, J_1^2(\beta)$$

when β is small: $J(\beta) = \beta$ and $H_1^{effective} = H_1 (\frac{\gamma H_m}{\omega_m})^2$

Change of H_m is basically equal to change of H_1. In practice, H_m is selected at some suitable (linear region) value and final adjustment are made using H_1.

Thus the frequency of audio modulation f_m determines whether the line shape is in derivative or absorption mode. For the convenience

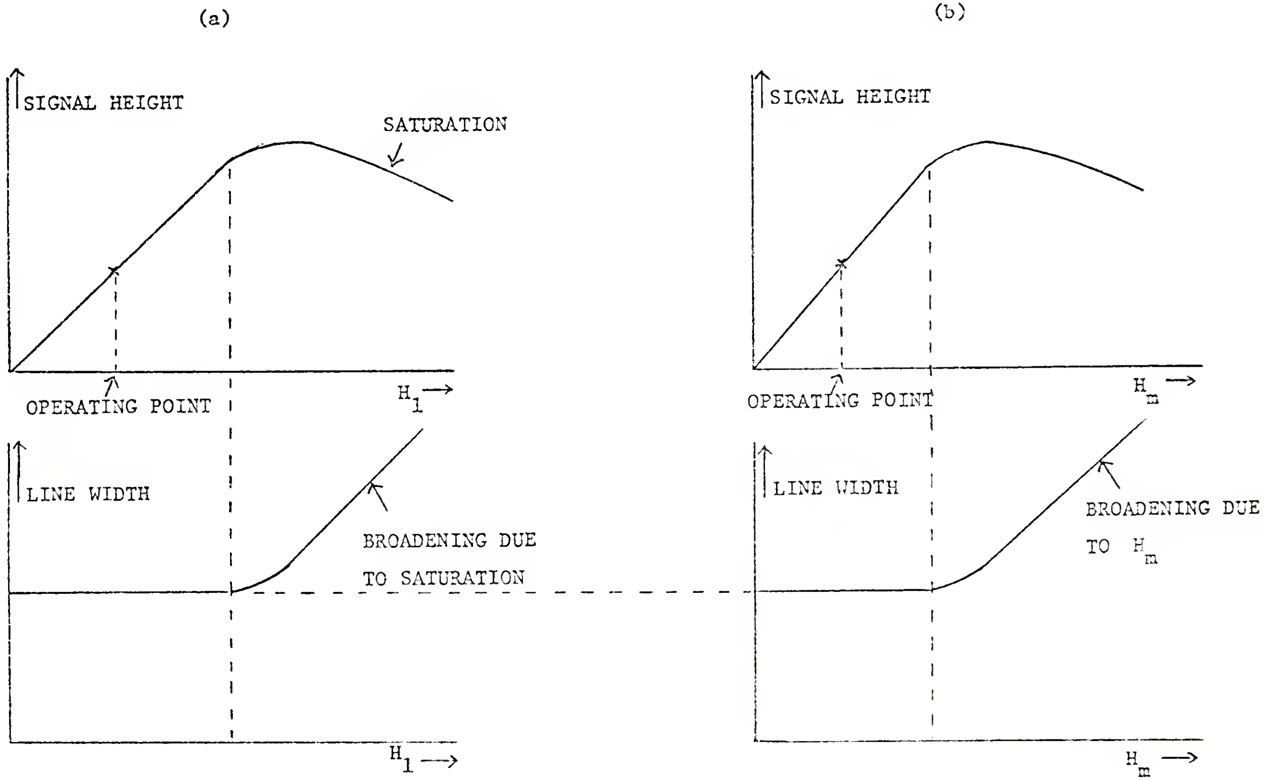

Fig. (37) The relation of the signal height to H_1 and H_m

(a) $f_m < \Delta f$ [DERIVATIVE MODE]

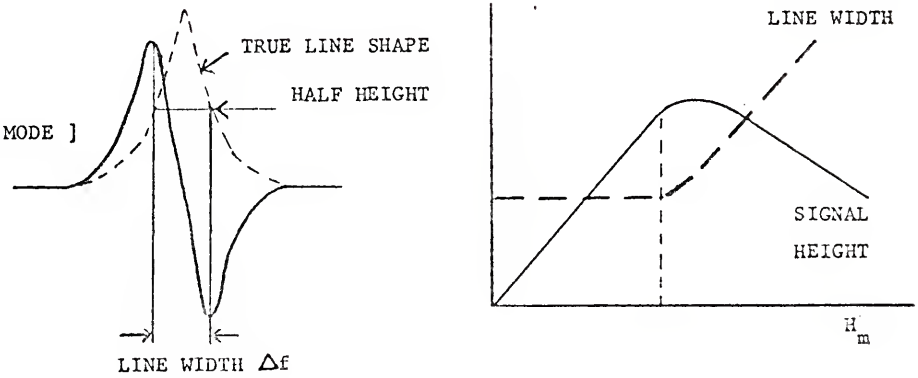

(b) $f_m > \Delta f$ [ABSORPTION MODE]

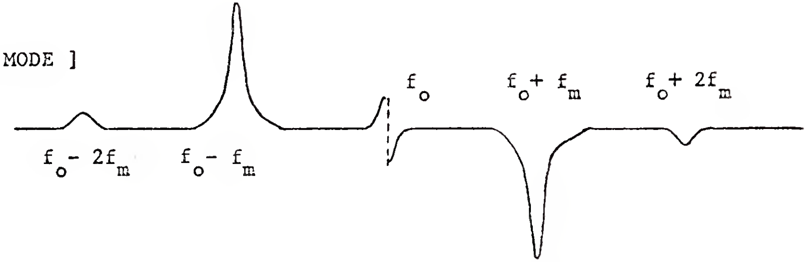

Fig. (38) The relation between audio modulation frequency f_m and line shape

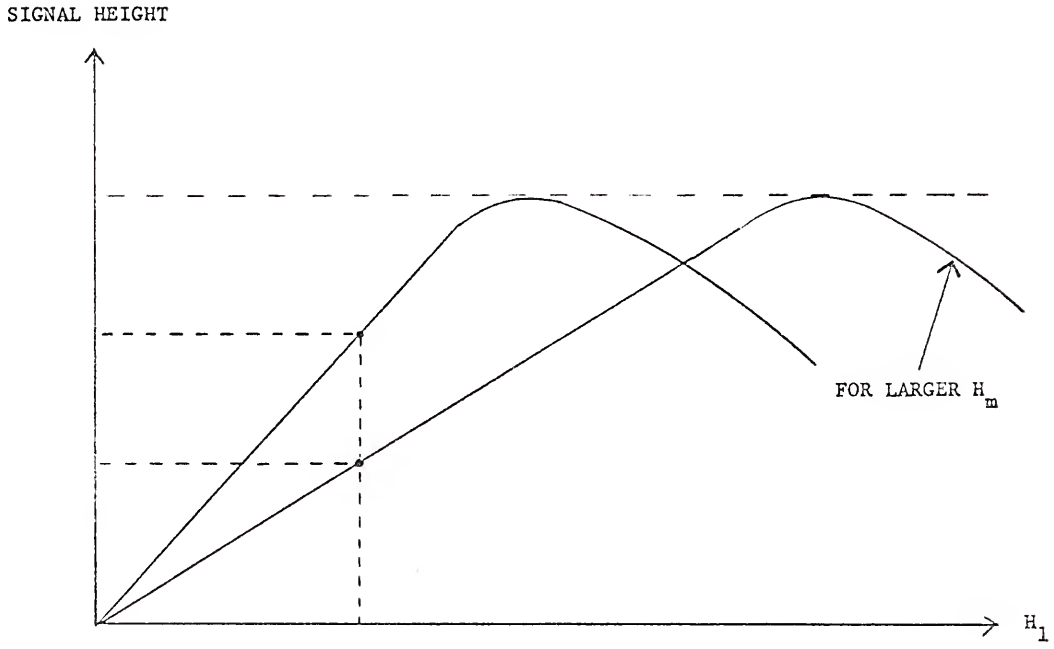

Fig. (39) The affection of change of H_m upon H_1

of comparison, we can convert the spectral line width (half height width of spectral line) to corresponding Δf. When phase detected at the field modulation frequency, the familiar derivative spectrum is obtained. The discussion thus far applies to the situation where the modulation frequency ω_m is less than the linewidth expressed in frequency units. In the phase angle ϕ between the audio output and reference is adjusted to $\frac{\pi}{2}$, the largest central peak is expected [graph(a) of Fig.(40)]. The change of polarity of the central peak in this graph is not a 'derivative' case; this must be noted during data analysing. Graph(b) of Fig.(40) shows the correct audio phasing at $\phi=0^o$ removes the central narrow line and obtains prominant side bands if the effective H_1 is large enough. Under this condition the first sidebands are the undifferentiated absorption spectra, which are subject to saturation by $H_1^{effective}$ in the usual manner. The line width and signal height of each side-band depend on different characteristic curves shown in Fig.(41).

Suppose spectrum is more complex as shown in graph(a) of Fig.(42). If f_m is much larger either Δf_1 or Δf_2, we expect to see both line shapes are in absorption mode as shown in graph(b). If f_m is smaller than Δf_2, we will see both in derivative mode as shown in graph(c). If f_m is between Δf_1 and Δf_2, then the narrow line is in absorption mode and the wide line is in derivative mode; the spectrum is expected as shown in graph(d), and the frequency between the two narrow lines is still $2f_m$. Graph(e) shows that misphasing of the third case can cause other sidebands besides the first sidebands and each of them with same width in the case of no saturation.

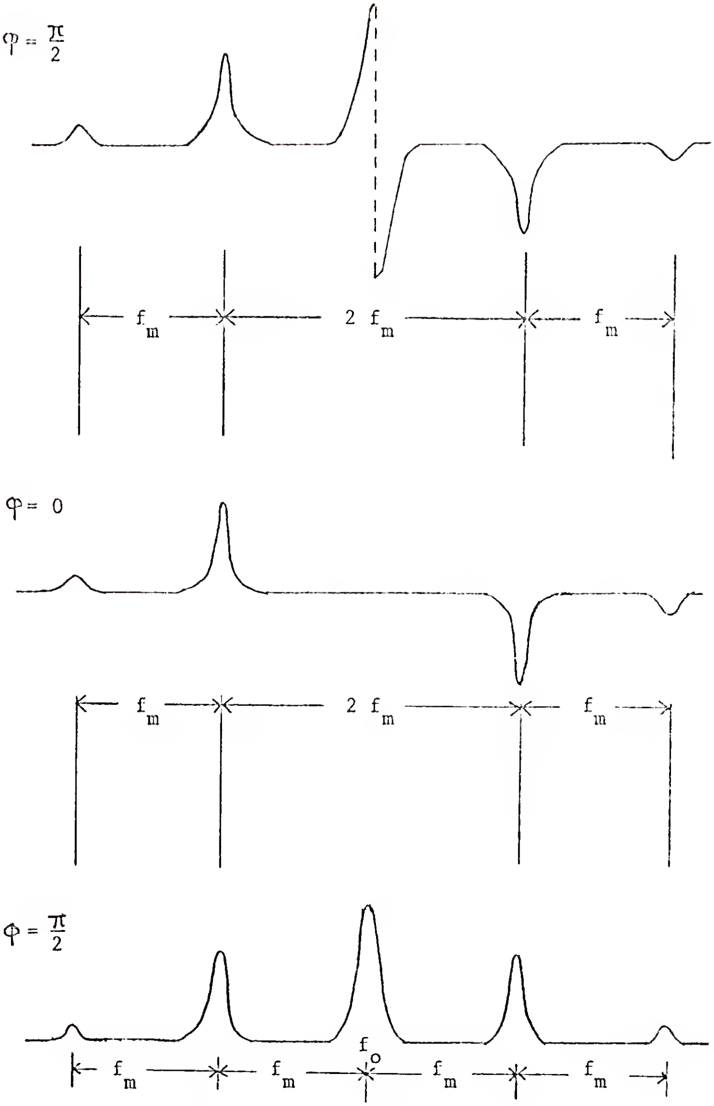

(a) $f_m > \Delta f, \quad \varphi = \frac{\pi}{2}$

(b) $f_m > \Delta f, \quad \varphi = 0$

(c) $f_m \gg \Delta f, \quad \varphi = \frac{\pi}{2}$

Fig. (40) Line shapes of the case : $f_m > \Delta f$

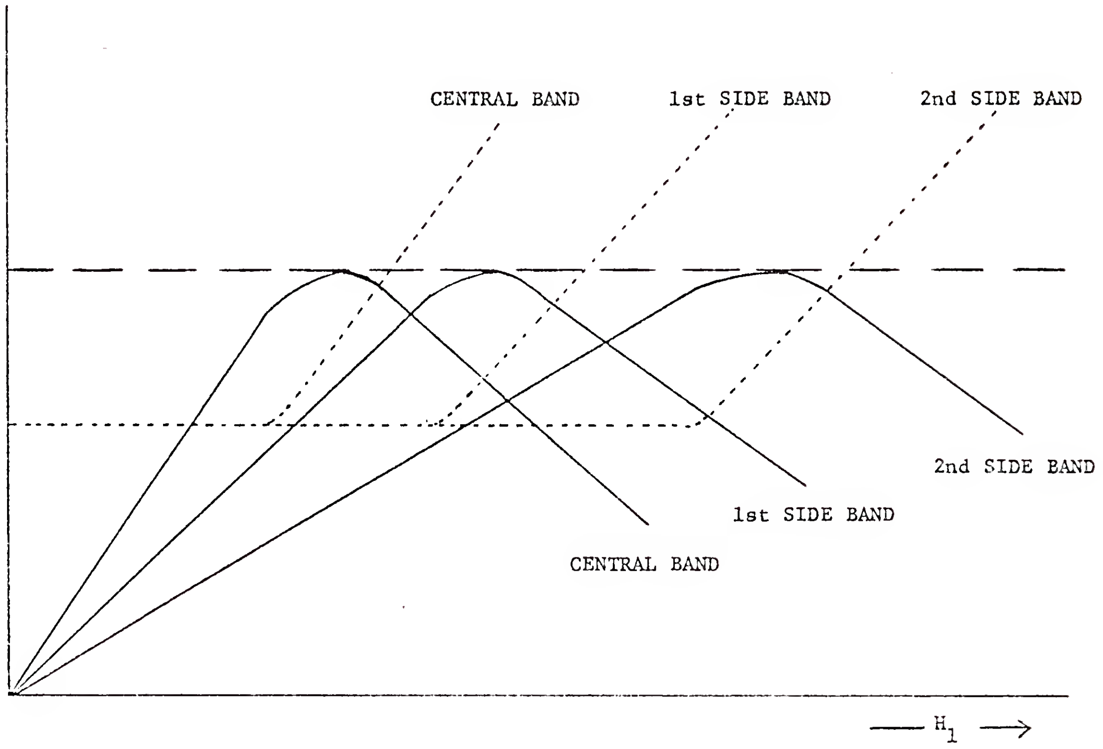

Fig.(41) Characteristic curve for different side bands (The solid line indicates signal height and dotted one line width.)

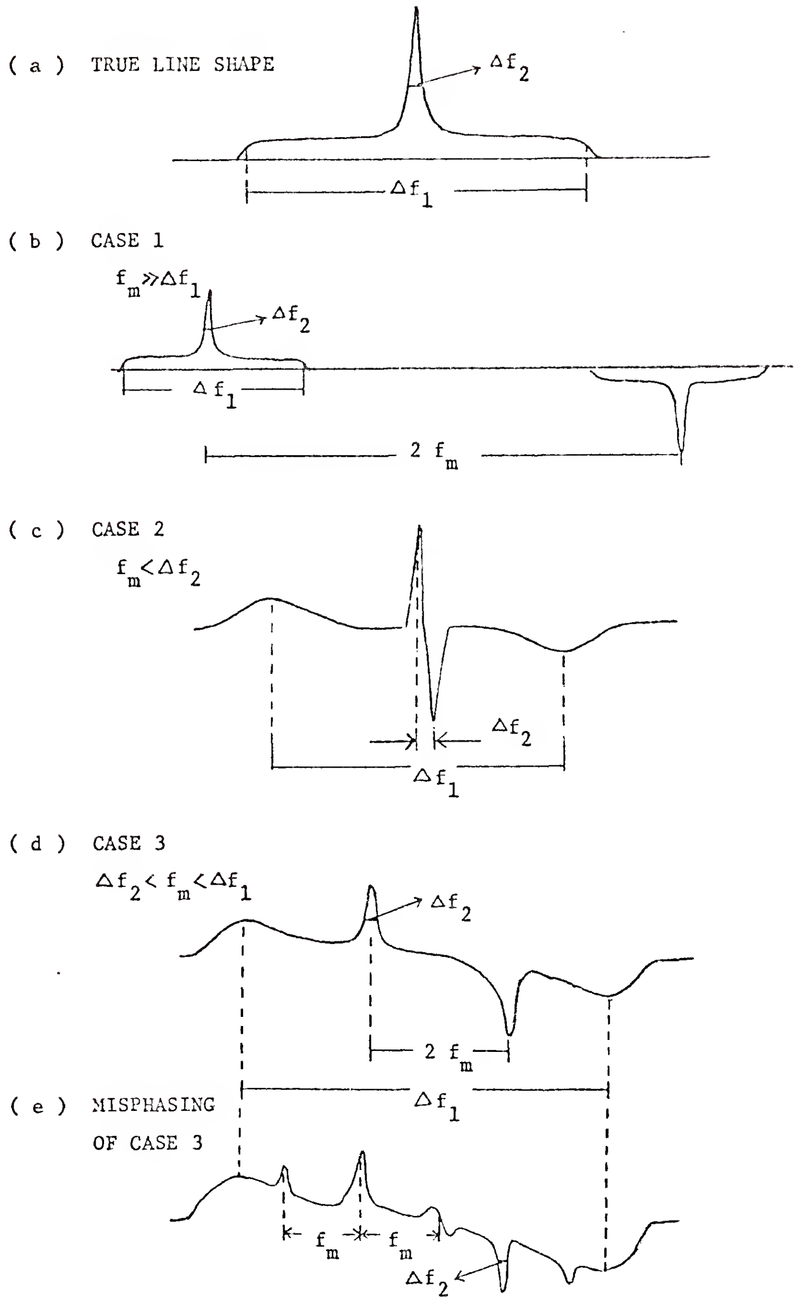

Fig. (42) Line shapes corresponding to different modulation frequency f_m of signal composing both narrow and wide line

III.4.2 Rate of Sweep and Magnetic Field Inhomogeneity

The line shape also depends upon the time taken to sweep through resonance. We may use $\Delta T = \Delta H/(\frac{dH}{dt})$ to characterize this time, where ΔH is the line width in magnetic field units and $\frac{dH}{dt}$ the sweep speed. Figure(43) shows how th sweep rate affects the line shape. In case(I), we obtain normal derivative spectra when ΔT is much larger than the time constant, and distortion of spectra when ΔT is close to the time constant. In case (II), we obtain further distortion of spectra when ΔT is smaller than the time constant. The symptom will also be observed if ΔT is smaller than the spin lattice relaxation time T_1. Thus the sweep rate has to be sufficiently slow that ΔT is slightly in excess of the time constant or T_1 whichever is the larger, whereas the noise is inversely proportional to the square root of the time constant. For optimum performance the time constant should not be less than T_1. Noise can be reduced by increasing the time constant and scanning more slowly or by making the two times comparable, scanning as rapidly as possible, and signal averaging.

Complication also arises from magnetic field inhomogeneity. Figure(44) shows that distortion due to magnetic field inhomogeneity may have a similar symptom e.g., if the field has a quadrupole component which produces an asymmetric line shape. We can distinguish this by checking the scan in both directions. If the polarity of the spectra does not change,this is due to magnetic field inhomogeneity. If only polarity change and distortion is in the same side as before, this is due to rapid passage.

The CW measurements recorded in this dissertation employed only slow passage conditions. Though the fast passage condition is not

CASE (I) $\Delta T >$ TIME CONSTANT

(a) $\Delta T \gg$ TIME CONSTANT

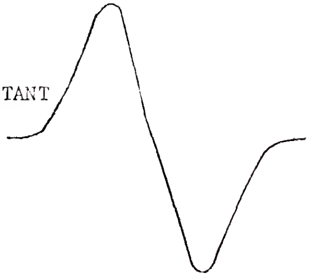

(b) $\Delta T \approx$ TIME CONSTANT

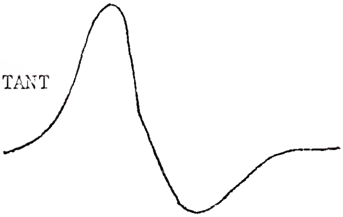

CASE (II) $\Delta T <$ TIME CONSTANT

(SAME SYMPTOM, IF $\Delta T < T_1$, WHERE T_1 IS SPIN-LATTICE RELAXATION TIME)

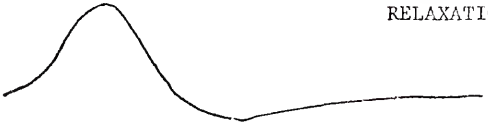

Fig.(43) The effect of slow and fast sweep upon the spectrum

CASE A DUE TO FIELD INHOMOGENEITY

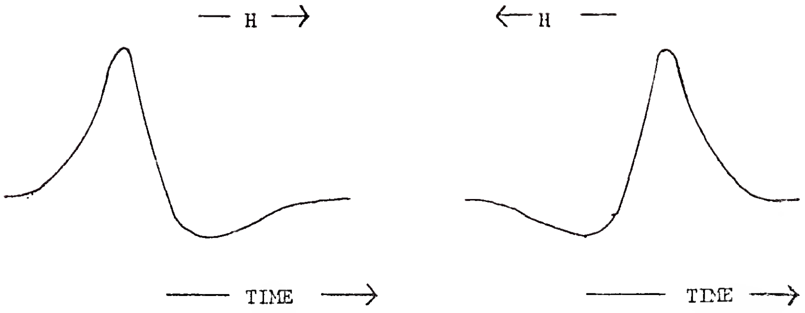

CASE B DUE TO RAPID PASSAGE

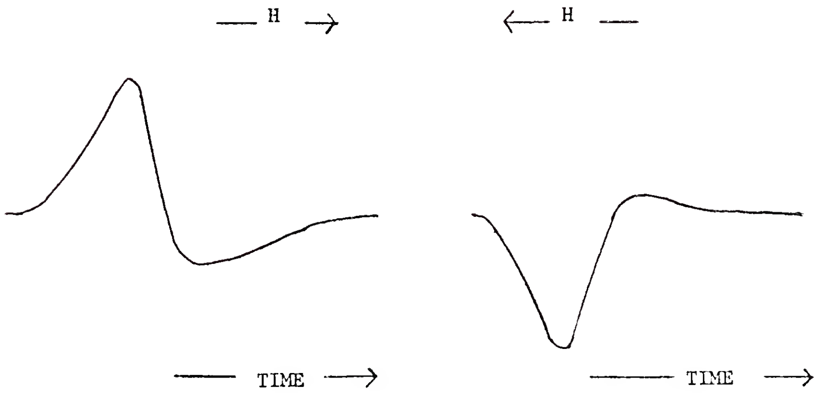

Fig.(44) The distinction of line distortion due to magnetic field inhomogeneity and rapid passage strictly relevant, we still discuss it a little. This is the case when ΔT is smaller than T_1. Under these conditions the initial signal height is proportional to the amplitude of the rf field. Before a new equilibrium (i.e. saturation) can be established the field has passed through the resonance condition. In practice this condition cannot be completely achieved, the later parts of the signal will be saturated and appear with reduced value. In this circumstance, fast passage will increase the linear region of signal height versus H_1 characteristic and allow the observation of a bigger signal than would otherwise be possible but it will have distorted line a shape as shown in case (II) of Fig.(44).

III.5 Noise

A major problem encountered by the NMR spectroscopist is the extraction of the signal from a noisy spectrum. Noise originates at each stage, but obviously that produced in the early stages of a high gain amplifier is the most significant. In NMR transmitter noise tends not to be significant as (i) in pulse NMR the signal is observed only when the transmitter is disconnected (ii) in CW-NMR the bridge, mechanical or electrical, attenuates the transmitter power and noise coupled into the receiver. There are usually some tuning elements in the receiver,which give it a bandwidth Δf_1. The noise is proportional to $(\Delta f_1)^{1/2}$, and in principle could be reduced by reducing Δf_1, but as this would raise problems in maintaining the alignment of the receiver, Δf_1 is usually made large. The output of the radio receiver is then detected by either diode or phase detector. The effect is to mix the output of the radio receiver, signal noise, with a reference signal at frequency f_o or with a leakage signal at frequency f_o. Application to a non-linear stage results in the generation of sum and difference frequencies and multiples thereof. The components near zero frequency are detected. This procedure results in a signal at zero frequency, in the absence of field modulation or at the field modulation frequency in it's presence, together with noise up to a frequency of Δf_1. This assumes that the additional noise introduced in the detector stage is negligible. In pulsed NMR this signal is then displayed, a low pass filter with cut-off at Δf_2 can be inserted to limit the bandwidth and thus the noise. To prevent signal distortion Δf_2 should exceed the highest significant frequency components of the Fourier Transform of the signal, i.e. if the characteristic time of the free induction decay is T_2^* , $\Delta f_2 > \frac{1}{T_2^*}$.

In CW-NMR field modulation is usually employed and in order to eliminate changes in receiver output arising from changes in transmitter power bridge balance, amplifier gain etc. use is made of the fact that the signal depends upon magnetic field whereas these other factors do not, and that a sinusoidal change in magnetic field at frequency f_m will produce a sinusoidal change in NMR signal at frequency f_m. Mixing with a reference signal at frequency f_m again generates sum and difference frequencies and the zero and near zero frequency components can be selected using a suitable phase detector. It is then convenient to limit the bandwidth Δf_3 in the subsequent d.c. stage. Again care must be taken to ensure that Δf_3 is sufficiently large not to distort the lineshape. If the sharpest spectral feature has a width ΔH and the sweep rate is dH/dt, then $\Delta f_3 > (\Delta H)^{-1}(dH/dt)$.

Because of problems of receiver alignment it is invariably more convenient to limit the bandwidth at the receiver stage. Sources of noise are (i) Johnson, (ii) Shot, (iii) Partition, (iv) Flicker. The first three are white broad band noise, whereas the last comprises low frequency components. The modulation frequency is made as high as possible to minimise it's contribution.

III.6 T_1 Measurement with $\pi \sim \tau \sim \frac{\pi}{2}$ Pulse Sequence

III.6.1 Disadvantage of Cross-Over Method

The easiest way to measure T_1 is by using the cross-over method, which finds the delay time giving a null signal after the $\pi/2$ pulse. If the magnetization $\vec{M}_o$ is flipped by a precise π pulse, we can adjust the delay time t to give a null free induction decay after the following $\pi/2$ pulse. It is easy to show that T_1 is equal to t/ln2. However, in practice it is difficult to tune a precise tilting angle of π and this affects the measurement of T_1 as shown by the analysis given below.

From the Bloch equation, the rate of change of the z component of magnetization is

$$\frac{dM_z}{dt} = \frac{M_o - M_z}{T_1} \quad \text{or} \quad \frac{dM_z}{M_o - M_z} = \frac{dt}{T_1} \qquad \text{(III.6.1.1)}$$

$$-\ln[M_o - M_z(t)] = \frac{t}{T_1} + C$$ where C is a constant depending upon initial condition.

$$M_o - M_z(t) = \exp(-\frac{t}{T_1})\ \exp(-C) \qquad (III.6.1.2)$$

Initially: after a pulse of θ [Fig.(45)]

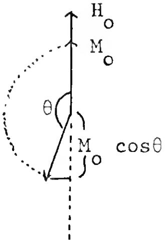

Fig.(45) Magnetization flipped down by an angle θ from initial direction

$$M_o - M_o\cos\theta = \exp(-C)$$

$$M_o - M_z(t) = M_o(\ 1 - \cos\theta\ )\ \exp(-\frac{t}{T_1}) \qquad (III.6.1.3)$$

Therefore

$$M_z(t) = M_o(\ 1 - (\ 1 - \cos\theta\ )\ \exp(-\frac{t}{T_1}) \qquad (III.6.1.4)$$

The cross-over method measures the time when $M_z(t) = 0$

i.e. $0 = M_o[\ 1 - (\ 1 - \cos\theta\ )\ \exp(-\frac{t}{T_1})]$

This gives $T_1 = \dfrac{t}{\ln(\ 1 - \cos\theta\ )}$ (III.6.1.5)

Thus the answer depends on θ.

If $\theta = \pi$ then $T_1 = t/\ln 2$

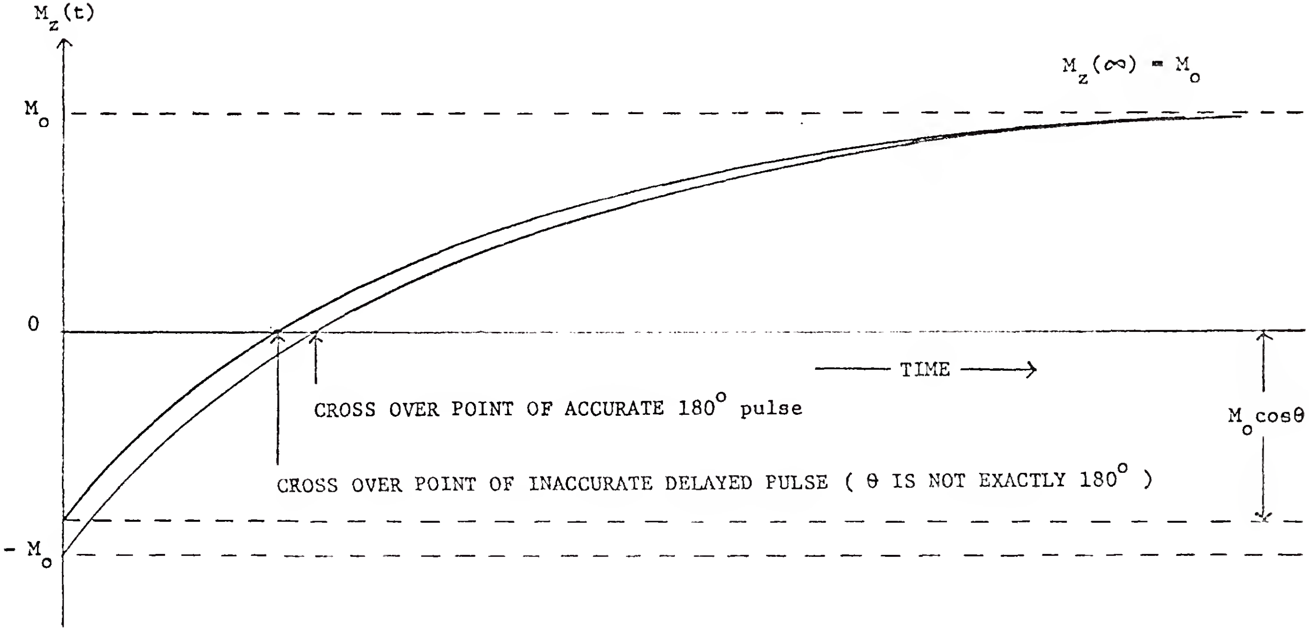

Fig. (46) Comparison between first pulses of $\theta = 180^\circ$ and $\theta \neq 180^\circ$ in T_1 measurement

Suppose the tilt angle θ is not π, then the existing error is

$$T_1 = t \left(\frac{1}{\ln 2} - \frac{1}{\ln(1 - \cos\theta)} \right) \qquad \text{(III.6.1.6)}$$

Figure(46) shows that two curves give different cross-over position, even though subject to same T_1 relaxation scheme.

III.6.2 Ringing

One of the errors of measuring the free induction directly comes from ringing of the pulse. Figure(47) shows how the tail of the pulse can mix with the free induction decay. The procedure used was to find the intercept of the extension of the FID with an "ideal" pulse and then measure the amplitude between this intercept point and the base line. The width of the FID of the same sample varies at different temperatures. A narrow FID with steep slope enhances the error. Failure to compensate will result in error, e.g., a 20 % smaller T_1 in severe case [Fig.(48)].

Ringing is a basic damping problem of the LRC circuit. For simplification of the problem, one can denote the total resistance, capacitance and inductance as R, L and C respectively. The damping for $t < 0$ can be ignored because of the large driving power of the rf source. For $t > 0$, there are three types of damping, namely:

(i) $R^2/4L^2 > (LC)^{-1}$ This is the condition for OVER DAMPING. The voltage has two mixed exponential decay schemes and decreases to zero at $t = \infty$.

(ii) $R^2/4L^2 = (LC)^{-1}$ This is the condition for CRITICAL DAMPING, the system is said to be DEAD BEAT. The

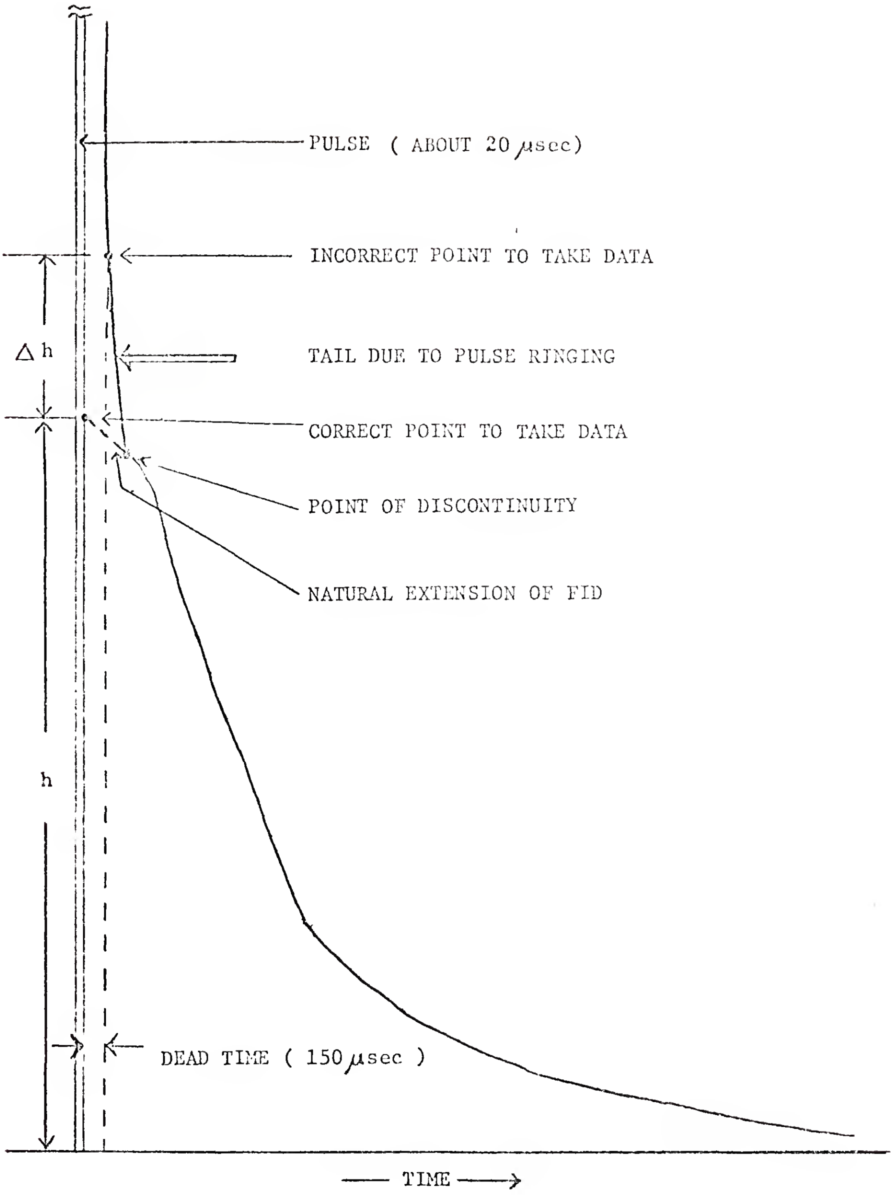

Fig.(47) The observed FID as displayed on the X-Y recorder

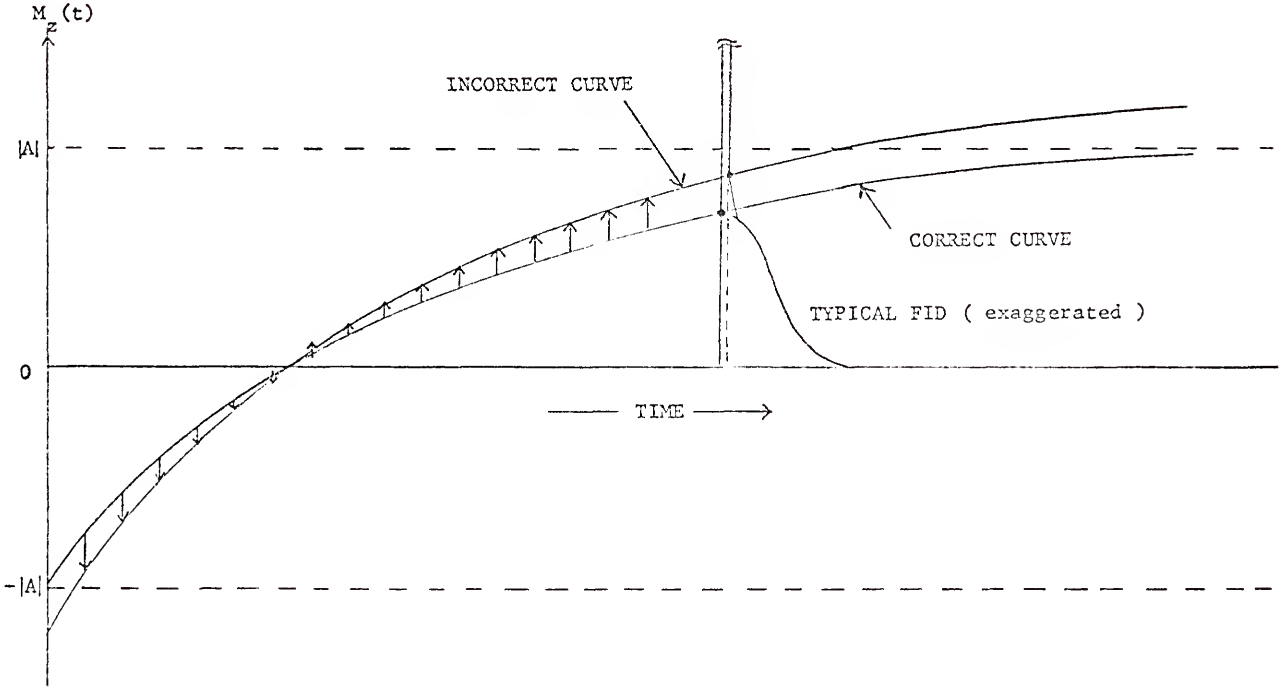

Fig.(48) Effect of ringing on T_1 measurement voltage has only a single exponential decay scheme and decreases to zero in the shortest time. This is what we prefer.

(iii) $R^2/4L^2 < (LC)^{-1}$ This is the condition for DAMPED OSCILLATION, and the case we are most concerned with. If the R/2L is small, the voltage takes a long time to damp out, thus causes serious ringing.

Since the phase at which the radio wave(contained within the $\pi/2$ pulse envelope) is cut by the pulsing gate is beyond control, it is difficult to provide an initial condition to remove ringing. Therefore we must increase the R/2L ratio to have fast damping. The resistance R comes predominantly from the probe in most cases, but other resistance from the transmitter and receiver contributes also. To construct a coil with finer coil wire can increase resistance dramatically, but decreases the quality factor $\omega_o L/R$. Fortunately, the deuteron signal is strong, and the signal-to-noise ratio in most of the temperature range is good; hence a large quality factor is comparatively not so critical.

III.6.3 Dead Time

If a $\pi/2$ pulse of time duration Δt is given to a resonant sample, the free induction decay starts from $\Delta t/2$ in principle. In practice the FID is observed starting from$(\Delta t/2)+b$. No information is observable within the period b. This time interval is called DEAD TIME. The dead time is caused by the recovery of the system. Bad tuning increases the dead time tremendously; therefore, one must accurately tune the system to reduce dead time and preserve more information. A well tuned pulse must have the shortest decay and rise time by decreasing time constant. Unfortunately, there is a limit for doing this. Large capacitance needs large inductance of the sample coil for balance to avoid serious ringing, as has been discussed in the last subsection. To obtain a strong signal, we made the sample as large as the physical dimensions of cryostat permitted; hence the geometrical size of the sample coil was predetermined. A large inductance then requires finer wire if the geometry of the coil is fixed and this increases resistance which in turn reduces gain. Therefore we can only tune the system by a compromise among L, R, and C.

The signal developed in the receiver coil is proportional to the Q factor of the coil and should therefore be high. The dead time is inversely proportional to the bandwidth and therefore the bandwidth should be high and the Q factor low. Design of a suitable coil system requires a compromise between these competing factors.

For the 20 μsec pulse of this experiment, the dead time is about 150 μsec. This is short compared with the relaxation time of ten to a few hundred msec over most of the temperature range. Below $-40^{\circ}C$, most of the samples studied have their relaxation time below 2 msec, and a larger error is expected.

III.7 T_2 Measurement with $\frac{\pi}{2} \sim \tau \sim \pi$ Pulse Sequence

The $\frac{\pi}{2} \sim \tau \sim \pi$ pulse sequence was employed to measure the envelope of the spin echoes. The formation of spin echoes has been mentioned in the basic theory in chapter II. To obtain a good echo, correct tuning in both pulse and signal is essential. In this section, we shall discuss the analysis of the data for the liquid crystal which exhibits two different relaxation times.

Since a diode detector was used to measure the spin-spin relaxation time T_2, all echoes are subject to a basic line shift (chapter III, section III.3.8); the shift can be removed by self adjustment in computer programming. In graph(a) of Fig.(49), we can see two types of distortion causing a non-exponential decay curve of the spin echo in the liquid crystals phase. The distortion in the tail is especially subject to the base line shift and non-linearity of the diode for small input signal. The second factor is much improved by using a DC voltage supply of approximate 0.3 volt to shift the input signal (section III.3.8). The distortion near the origin arises is because two pulses are too close.

In graph(b) of Fig.(49), liquid crystal, a typical example, is shown for the hexanol W/O = 1.2 with S/O = 0.2. There are two features, one for tightly bound water of the same kind as shown in graph(a), the other due to isotropic water. Therefore data taken for least square fit must be treated separately. When we take height of echoes, the distortion area of graph(b) must be excluded, otherwise larger T_2 for tightly bound water and smaller T_2 for isotropic water are expected.

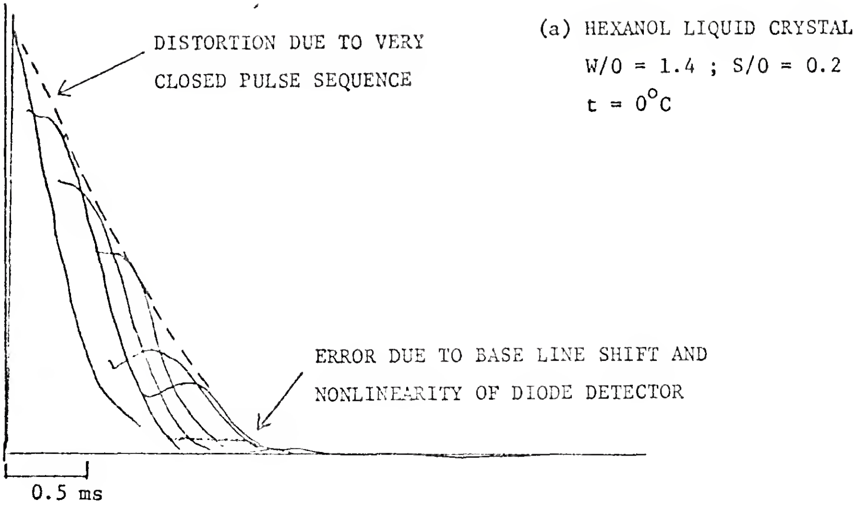

(a) HEXANOL LIQUID CRYSTAL
W/O = 1.4 ; S/O = 0.2
t = 0°C

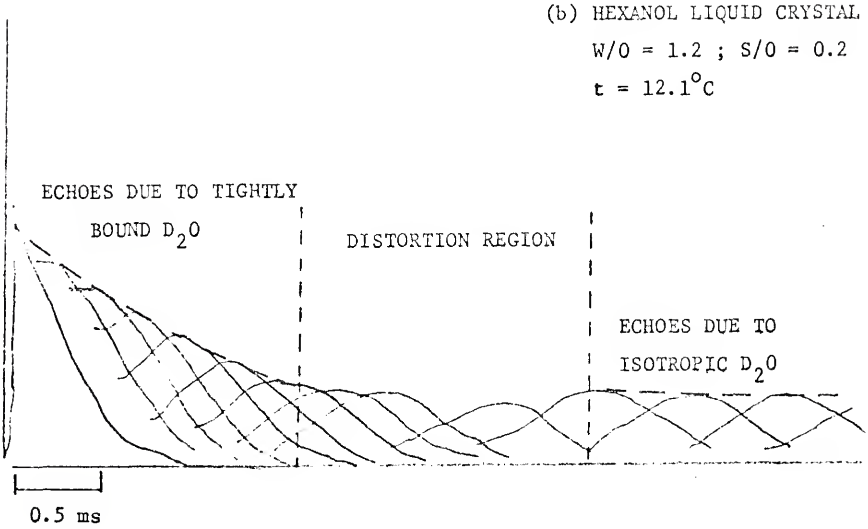

(b) HEXANOL LIQUID CRYSTAL
W/O = 1.2 ; S/O = 0.2
t = 12.1°C

Fig.(49) Envelope of spin echoes of two typical liquid crystals

III.8 Least Square Fit

The amplitude of the free induction decay following a pulse is given by $y = A - B\exp(-\frac{t}{T_1})$. T_1 was deduced from a least square fit of this equation to experimental data following a procedure described by Sass and Ziessow[38].

The least square fit is based on the assumption that the error of the measured signal has a Gaussian distribution. The error square sum[39][40] is given by

$$E = \sum_{i=1}^{N} [\ y_i - A - B\exp(\ \alpha t_i)] = 0 \qquad \text{(III.8.1)}$$

where y_i is the ith measurement of the magnetization at delay time t_i, and $\alpha = -\frac{1}{T_1}$. To minimize E, the three partial derivatives $\frac{\partial E}{\partial A}$, $\frac{\partial E}{\partial B}$, and $\frac{\partial E}{\partial \alpha}$ are set to zero.

$$-\frac{1}{2}\frac{\partial E}{\partial A} = \sum_{i=1}^{N} [\ y_i - A - B\exp(\ \alpha t_i)] = 0 \qquad \text{(III.8.2)}$$

$$-\frac{1}{2}\frac{\partial E}{\partial B} = \sum_{i=1}^{N} [\ y_i - A - B\exp(\ \alpha t_i)]\exp(\ \alpha t_i) = 0 \qquad \text{(III.8.3)}$$

$$-\frac{1}{2B}\frac{\partial E}{\partial \alpha} = \sum_{i=1}^{N} [\ y_i - A - B\exp(\ \alpha t_i)]\ t_i\exp(\ \alpha t_i) = 0 \qquad \text{(III.8.4)}$$

One then solves for equations (III.8.2) and (III.8.3) as a function of α. Introducing the abbreviations

$$\sum_{i=1}^{N} x_i \equiv \{x\} \qquad e_i \equiv \exp(\ \alpha t_i)$$

one obtains $$A = \frac{\{y\}}{N} - \frac{\{y\}\{e\} - N\{ye\}}{N^2\{e^2\} - N\{e\}^2}\{e\} \qquad \text{(III.8.5)}$$

$$B = -\frac{\{y\}\{e\} - N\{ye\}}{N\{e^2\} - \{e\}^2} \qquad \text{(III.8.6)}$$

Substitute A and B in equation (III.8.4) yields

$$G = (N\{e^2\} - \{e\}^2)\{yte\} + (\{ye\}\{e\} - \{y\}\{e^2\})\{te\}$$
$$+ (\{y\}\{e\} - N\{ye\})\{te^2\} = 0 \qquad \text{(III.8.7)}$$

where G is a refined value of αs

The null position of G is iteratively determined with the Newton method:

$$\alpha(k+1) = \alpha(k) - [\ G(k)/G'(k)], \qquad \text{(III.8.8)}$$

where the index k indicates the k th choice of α and G' is the partial derivative $\frac{\partial G}{\partial \alpha}$:

$$G' = (N\{te^2\} - \{te\}\{e\})\{yte\} + (N\{e^2\}\{yt^2e\}$$
$$+ (\{ye\}\{te\} - \{y\}\{te^2\})\{te\} + (\{ye\}\{e\} - \{y\}\{e^2\})\{t^2e\}$$
$$+ 2\ (\{y\}\{e\} - N\{ye\})\{t^2e^2\}\ . \qquad \text{(III.8.9)}$$

The iteration (III.8.8) was programmed in BASIC for a PDP-8/A CLASSIC computer. Input data are the number of signals N, the free induction decay amplitude y_i, the delay time t_i and a guessed initial value for T_1. If the choice of T_1 is within ±50 % of the final T_1 value, no more than 5 iteration steps are usually required to fit T_1, A and B with an accuracy of ±1 %.

Two programs are attached in the appendix. The second program is the same as the first one except that provision is made for entering data from a large number of measurements at one time rather than one set separately for each fit. The program selfadjusts the base line and does not need to know y at $t = \infty$. For fast convergence the data should include points in the region of fast change of signal, i.e. roughly from $t = 0$ to T_1. The correspondence of notation between the analysis above and the program is given by the following equivalences:

$$y_i \equiv A(I), \quad t_i \equiv T(I), \quad \{e\} \equiv S(0), \quad \{e^2\} \equiv S(1)$$

$$\{y\} \equiv S(2), \quad \{ye\} \equiv S(3), \quad \{yte\} \equiv S(4), \quad \{te\} \equiv S(5),$$

$$\{te^2\} \equiv S(6), \quad \{yet^2\} \equiv S(7), \quad \{et^2\} \equiv S(8), \quad \{e^2t^2\} \equiv S(9),$$

$$A \equiv H, \quad B \equiv M, \quad \alpha \equiv G, \quad G \equiv G1, \quad G' \equiv G2$$

The program assumes an exact determination of t_i. The error in t_i is within 1×10^{-5} sec; therefore, the influence on y_i can be negligible. The least square fit method is independent of tilt angle θ.

The Wang pulse programmer used in this study gives an unstable delay time for t_i larger than 216.15 ms. This causes slow converge and errors in the case T_1 is larger than 200 ms. Therefore the semilogarithmic graphical method was employed also by plotting $[\, y(\infty) - y_i(t)]$ on a semilogarithmic scale against delay time and calculating T_1 from the slope. This method is also free from the inaccurate adjustment of the tilted angle θ, but needs to know y_i at $t = \infty$, which equals y_1 at $t = 0$.

The same computer program was used for the least square fit of the spin envelope to calculate T_2 values. The program selfadjusts the base line and does not need to know the very small echo amplitude for the very large delay time. The semilogarithmic method was also employed for T_2 larger than 250 ms for the same reason mentioned in the last paragraph.

III.9 Visual Observation

The purpose of the visual observations was to check birefringent phenomena and phase separation in order to compare with the relaxation time measurements, which were performed in a metal cryostat where the samples were not visible. A limitation of the visual observations occurs at lower temperature. Below the melting point of hexadecane $18^{\circ}C$, the samples become an opaque milk-like liquid and visual observation is no longer possible.

The apparatus used is very simple, as is shown in Fig.(50). The system is basically a gas flow cryostat in which gas at a regulated temperature is passed through a glass U tube containing the sample inside a copper can. For observation above room temperature, we passed air through a high power electrical heater and then through the cryostat. Both flow rate and current of the heater were controlled to raise the temperature of the copper cryostat. For the observation below room temperature, we introduced cold nitrogen gas flow by controlling the current is a resistor submerged in an external liquid nitrogen bath. The pyrex glass U tube was mounted inside a large glass dewer. Diagram of the copper cryostat is shown in Fig.(51). It has an external diameter of one inch and internal one of 0.5 inch to contain the sample. Glass slits with a width 1/8 inch located diametrically opposite on the cylinder provide a light path for viewing the sample.

Two polarized plates were located in opposite sides of the slits.

The copper cap limits heat radiation. Two pairs of thermocouples are located inside to measure temperature of the sample at different positions. This cryostat gives a homogeneous temperature distribution all over the sample because of the excellent thermal conductivity of copper. The axial temperature gradient can be reduced if the time for heating or cooling is sufficiently long. In general, it takes 5-10 minutes to reach thermal uniformity near room temperature and 25-40 minutes at 70 degrees from room temperature. The glass dewer in Fig.(50) is sealed with tape and a vapor absorber material is placed on the bottom to prevent ice crystalization on the surface of the glass U tube when the temperature is reduced. The thermocouples were connected to a potentiometer by a DPDT switch. An ice water mixture was used as reference junction.

In the case of the microemulsions, light is scattered isotropically by the small water droplets; hence we expect to see uniform illumination as the polarized plates are rotated and to have maximum intensity when the plates are orthogonal to each other.

In the case of the liquid crystals, the light is reflected anisotropically because of their grating-like structure. When the path difference of light is an intefral multiple of the wavelength, there is interference and we observe colorful birefringence. Since the gap between two layers is of the order 10^2 Å, which is small compared with the wavelength of visible light, the expected angular distribution is close to 90°. If we observe a completely dark sample with two plates orthogonal to each other, this means that the gap between layers is so narrow that the light beam is not transmitted.

This special case has been observed for a pentanol sample of W/O=0.6 with S/O=0.2.

After phase separation at high temperature, the liquid crystal takes 2 to 10 hours to return to its original structure. If the sample is taken out of the cryostat and shaken well, the structure is restored immediately. This is consistant with the experience that T_2 measurement of the liquid crystals in the phase separation region at high temperature shows thermo-hysterisis.

The visual observations were carried out from room temperature down to the freezing point of hexadecane(18^oC) and from room temperature up to 100^oC.

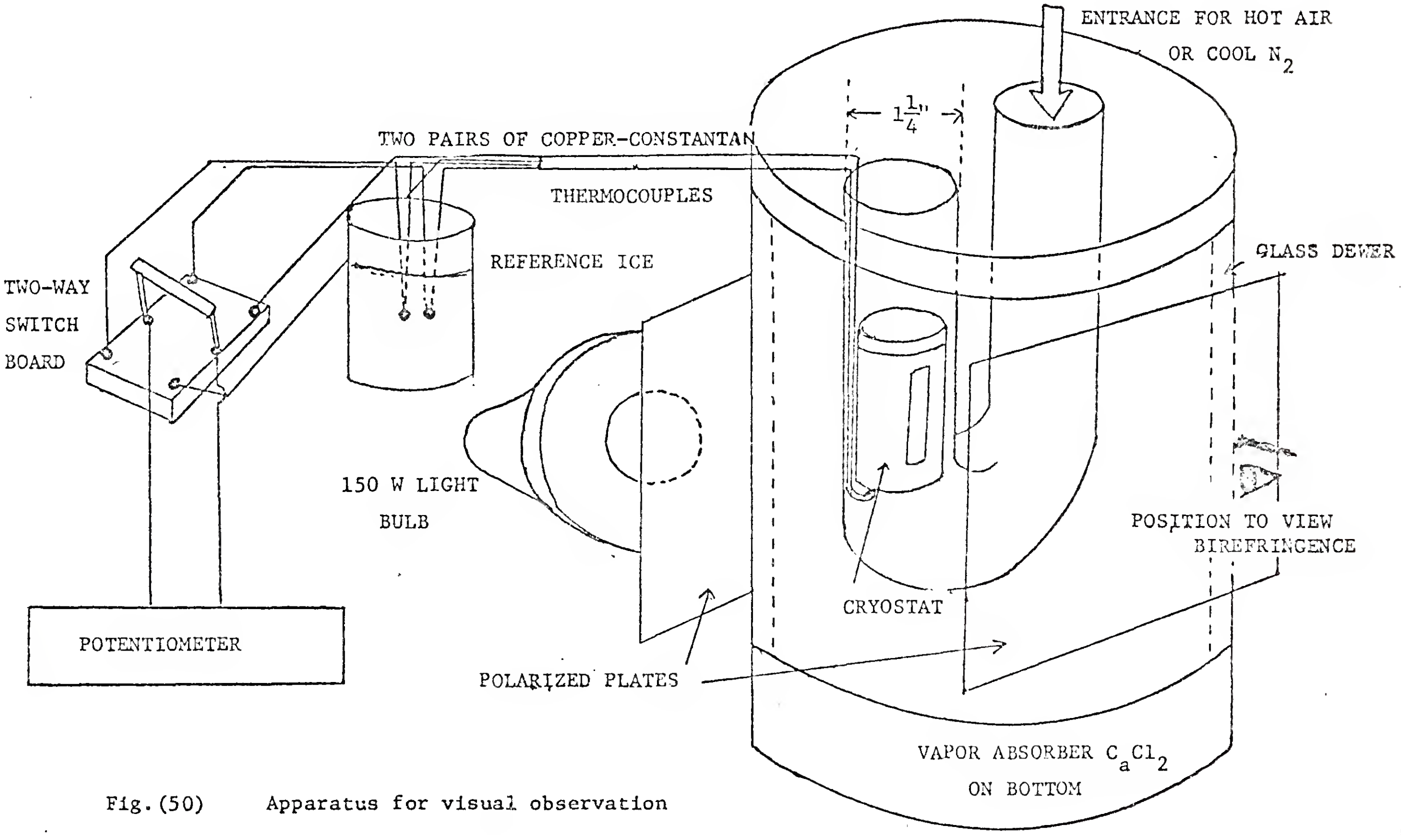

Fig. (50) Apparatus for visual observation

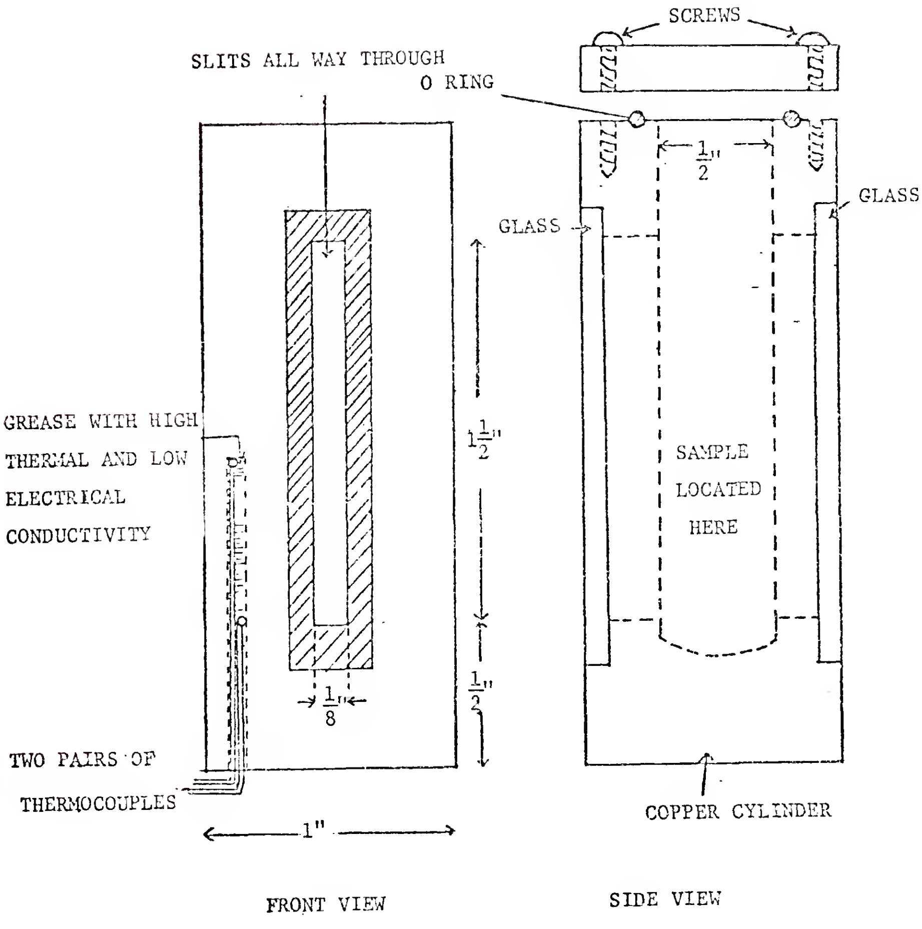

Fig.(51) Cryostat for visual observation

CHAPTER IV RESULTS AND CONCLUSIONS

IV.1 The Microemulsions

IV.1.1 The Validity of Bound Water Model

The bound water model proposed has been discussed in section II.4 of chapter II. Figure(52) shows the relationship between line width and radius of the microemulsion spheres. The volume ratio of oil/water (O/W) can be converted as in the following:

$$\frac{O}{W} = \left(\frac{O}{S}\right)\left(\frac{S}{W}\right) = \left(\frac{S}{O}\right)^{-1}\left(\frac{S}{W}\right) \qquad \text{(IV.1.1.1)}$$

where S/O is the ratio of surfactant to oil in gm/cm^3, and has the value 0.2.

If there are n water droplets, the total water volume will be $n\frac{4\pi r^3}{3}$, where r is the radius of each spherical droplet. Since potassium oleate has a highly polar terminal group and a hydrophobic alkyl chain, it is localized on the interfacial surface of the water droplet. Its weight will be $nM_s 4\pi r^2 C/A_s$, where M_s is the molecular weight, C the fraction of the total area occupied by the potassium oleate, and A_s the effective area occupied by each potassium oleate. The reason for introducing this is because, the localized cosurfactant hexanol may occupy the remainder of the area.

Therefore, $\frac{S}{W} = (n4\pi r^2 CM_s/A_s)/(n4\pi r^3/3) = 3M_s C/A_s r \qquad \text{(IV.1.1.2)}$

So, the ratio

$$\frac{O}{W} = \frac{15\ M_s\ C}{A_s} \cdot \frac{1}{r} \qquad \text{(IV.1.1.3)}$$

is proportional to r^{-1}.

Since simple exponential relaxation is observed for water in all the microemulsion samples, exchange between this "bound," or motionally restricted layer at the interfacial film and the "free"(or bulk liquid-like) water in the droplet interior must be rapid[41]. In this case, the observed water relaxation time will be a weighted average of the relaxation time of "free" and "bound" water as given by

$$< \frac{1}{T_2} >_{obs.} = P_b \frac{1}{T_2^b} + (1 - P_b) \frac{1}{T_2^f} \quad . \qquad \text{(IV.1.1.4)}$$

Substituting $P_b = \dfrac{4\ \pi r^2\ \Delta r}{\frac{4}{3}\pi\ r^3}$ (IV.1.1.5)

where Δr is the thickness of bound water, one obtains

$$< \frac{1}{T_2} >_{obs.} = \frac{1}{T_2^f} + 3\ \Delta r (\frac{1}{T_2^b} - \frac{1}{T_2^f}) \frac{1}{r} \qquad \text{(IV.1.1.6)}$$

A linear relationship between observed relaxation rate (or line-width) and the reciprocal of the drop radius is therefore predicted. This equation also predicts that if a range of drop radii occurred in a given sample at a fixed temperature there would be a range of T_2 values. The relaxation data, however, provide no evidence of multicomponent relaxation and thus indicate that the drops are of rather uniform size for fixed composition and temperature. This has been confirmed by a light scattering experiment[8]. If the exchange of water molecules between droplets is slow, non-exponential relaxation would be predicted. The slopes of Fig.(52) depend upon both $\frac{1}{T_2^b}$ and Δr. If either is known independently, the other could be calculated.

Mathematically, the relationship(IV.1.1.5) is no longer true when r is comparable with Δr. If the outer radius of the droplet is r_1 and the radius of the bulk water core is r_2, then the probability to be "bound" in the limiting case will be

$$\lim_{r_2 \to 0} P_b = \frac{\frac{4}{3}\pi(r_1^3 - r_2^3)}{\frac{4}{3}\pi r_1^3} = 1 \qquad (r_1 \to \Delta r)$$

Since the quantity of the bulk water then becomes negligible, the second term of formula(IV.1.1.4) vanishes. Therefore $\langle \frac{1}{T_2} \rangle_{obs.} = \frac{1}{T_2^b}$. When we plot log $\langle T_2 \rangle_{obs.}$ against radius of the droplet at fixed temperature for different microemulsion samples, we can extend the line (fairly linear) to intercept the ordinate to obtain T_2^b.

From Fig.(52), we can see that graphs of the line width against O/W ratios at fixed temperature are linear. If we extend this line, the interception at $r^{-1} = 0$, should be the same as the intrinsic line width of D_2O. Those data obtained by the pulsed method are calculated as the full width at half height = $(\pi T_2)^{-1}$, by assuming a Lorentzian shape. As the observed deuteron spin-spin relaxation was single component exponential this seems to be a valid assumption. Linewidth data from the continuous wave measurement are somewhat larger, but exhibit the same linear relation. The most likely explanation for this difference in linewidth between the CW and pulse methods is that the CW measurements are broadened by magnetic field inhomogeneity, whereas the Carr-Purcell pulse sequence compensates for field inhomogeneity. Another factor influencing the accuracy of the CW measurements was the temperature control. The gas flow type controlling system only gave a fairly uniform temperature in a small region of about 1 cm, and therefore a thermal gradient exists inside the sample.

The radii of different microemulsions are listed in Table(2) in chapter I. From the known T_2^b , T_2^f (obtained from intrinsic bulk D_2O sample), $< T_2 >_{obs.}$, and r, we may obtain $\Delta r \simeq 1$ Å for each sample. The calculated result is listed in Table(5). T_2^b is 8, 12, 20, and 50 ms at 5, 15, 28, and 57°C, which are plotted in Fig.(53). Thus, the water relaxation time data suggest that on the average, about 1 Å thick layer of water molecules in the water droplet is restricted in motion by interaction with the surfactant polar groups. This corresponds roughly to a "monolayer" of water. This is also true over a wide range of temperature. The apparent deviation of the sample W/O = 0.1 can be explained that the composition was affected by the freeze-pump-thaw technique in such a case of small water content.

The experimental data strongly support the simple geometrical bound water model for microemulsions.

Table(5) The thickness(in Å) of the motional restricted layer of the microemulsions at different temperatures and various radii

r in Å at	5°C	15°C	28°C	57°C
W/O=0.1 (r = 16 Å)	1.80	2.03	1.98	1.78
0.2 (r = 23 Å)	1.06	0.98	1.10	1.15
0.4* (r = 28 Å)	0.92	0.86	1.02	1.10
0.6 (r = 36 Å)	0.90	0.93	1.04	1.22

* A reasonable guess from other sizes calculated by L.Prince and J.Schulman

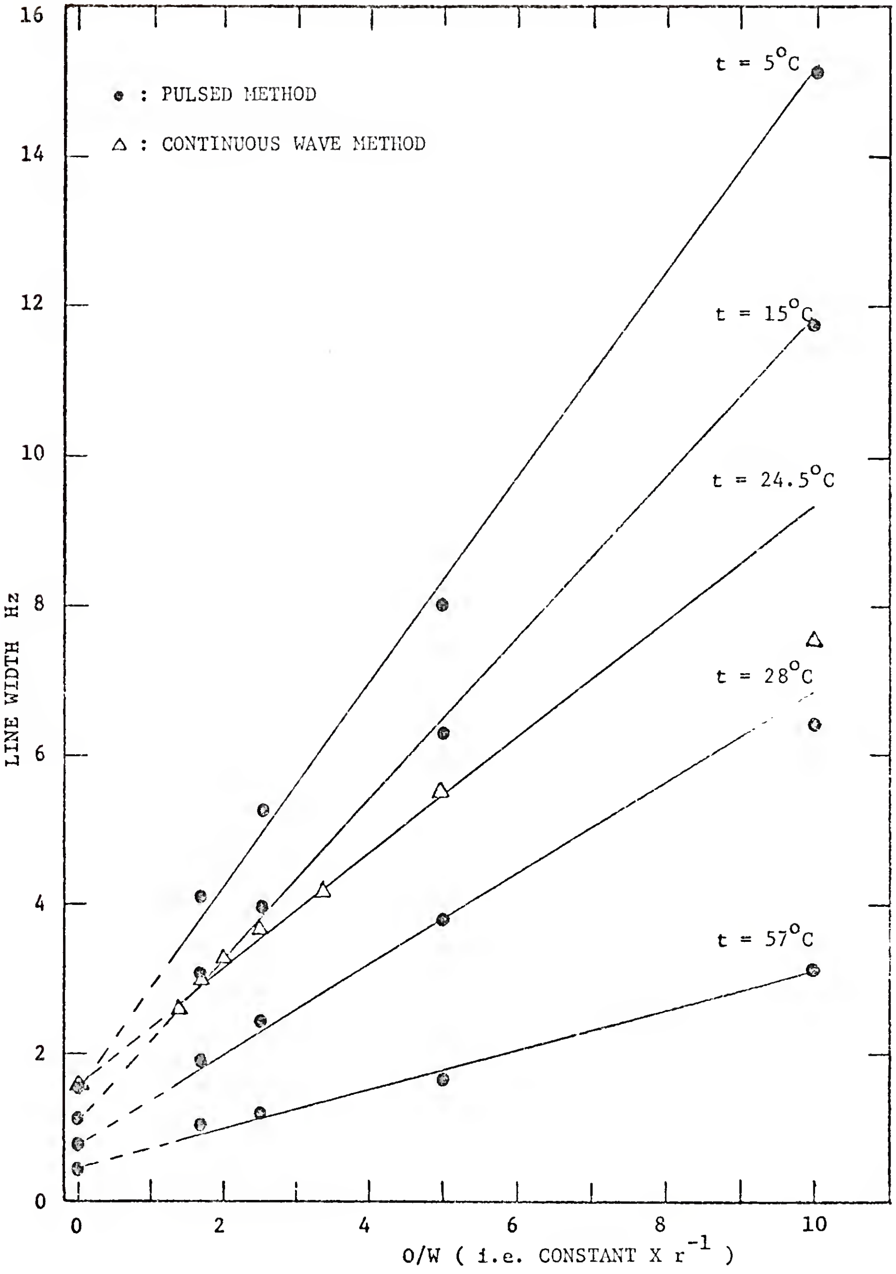

Fig. (52) The relation between line width and radius of the microemulsions

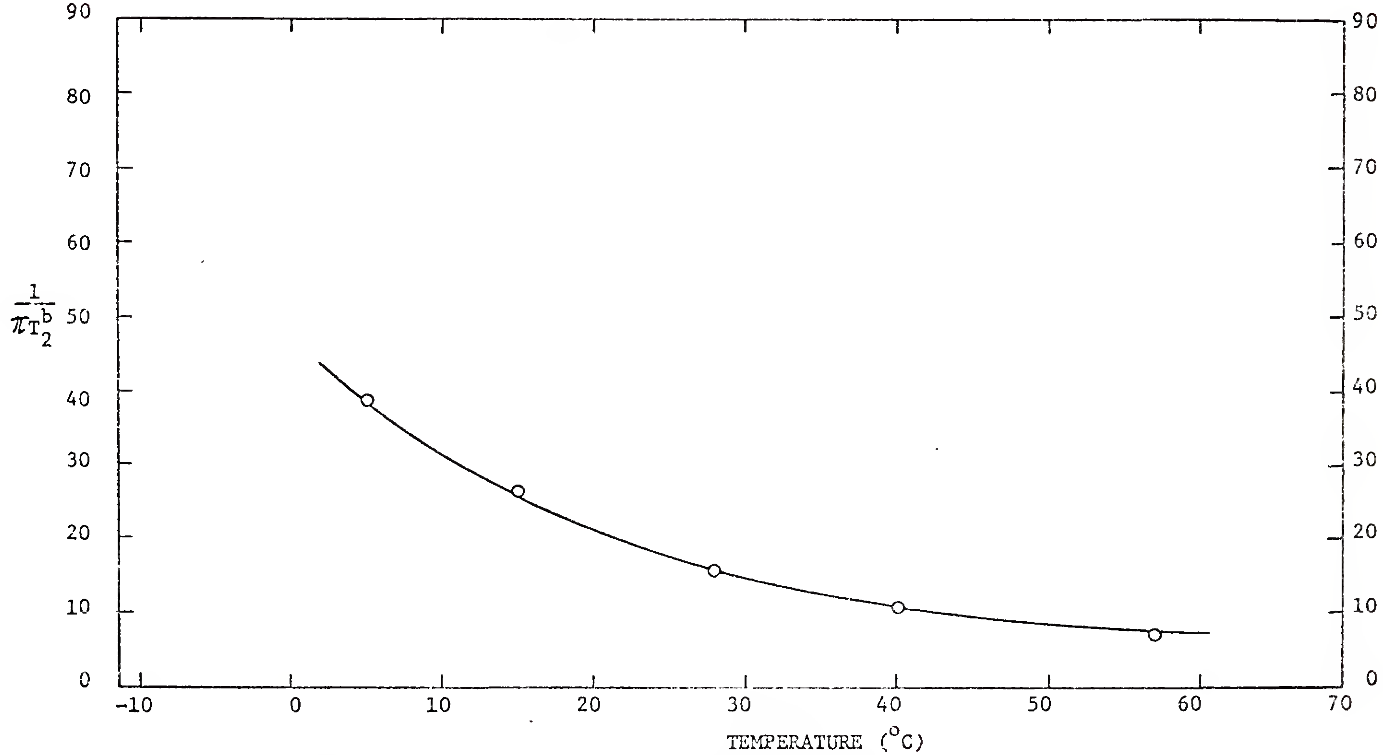

Fig.(53) Temperature dependence of the spin-spin relaxation rate due to the bound water

IV.1.2 The Rotational Diffusion and Chemical Exchange

The T_1 measurement as a function of temperature for pure D_2O(99.8%) compared with the typical microemulsion W/O = 0.1 is shown in Fig.(54). The calibration data (indicated by ■) is about the same as that obtained by Hindman[25]. Below the freezing point, the pure D_2O sample does not provide a visible signal, because quadrupolar and dipolar interactions in the rigid lattice of D_2O give a broad line on the order of 250 kHz wide. The microemulsion curve is generally parallel to the calibration curve except in the wide range of supercooling from -4°C to -44°C. Supercooling is expected to be prevalent because in bulk water freezing is normally induced by heteronuclei. In the microemulsions the water is distributed in the form of droplets, most of which will not possess a suitable impurity. The parallelness of the relaxation behavior implies that the core water in the droplets also experience the same two processes as demonstrated in bulk water[25], namely, (I) hydrogen bond breaking process at lower temperature and (II) Brownian rotational diffusion process. The difference in relaxation occurs because, motion of molecules in the bound layer is restricted even though the exchange between bound and free molecules is rapid. We assume that the influence of paramagnetic impurities is negligible. Let us look at the T_2 behavior of four microemulsions with W/O volume ratio 0.1, 0.2, 0.4, 0.6 shown in Fig.(55), Fig.(56), Fig.(57) and Fig.(58). All values of T_2 above 40°C have tendencies to a decreased temperature gradient; this is caused by rotational motion. When the temperature increases, the thermal expansion increases the intermolecular distance; the rotational barrier (indicated by activation energy) becomes smaller[Fig.(16)]; therefore, the rapid rotational motion dominates. The thermal rotational diffusion

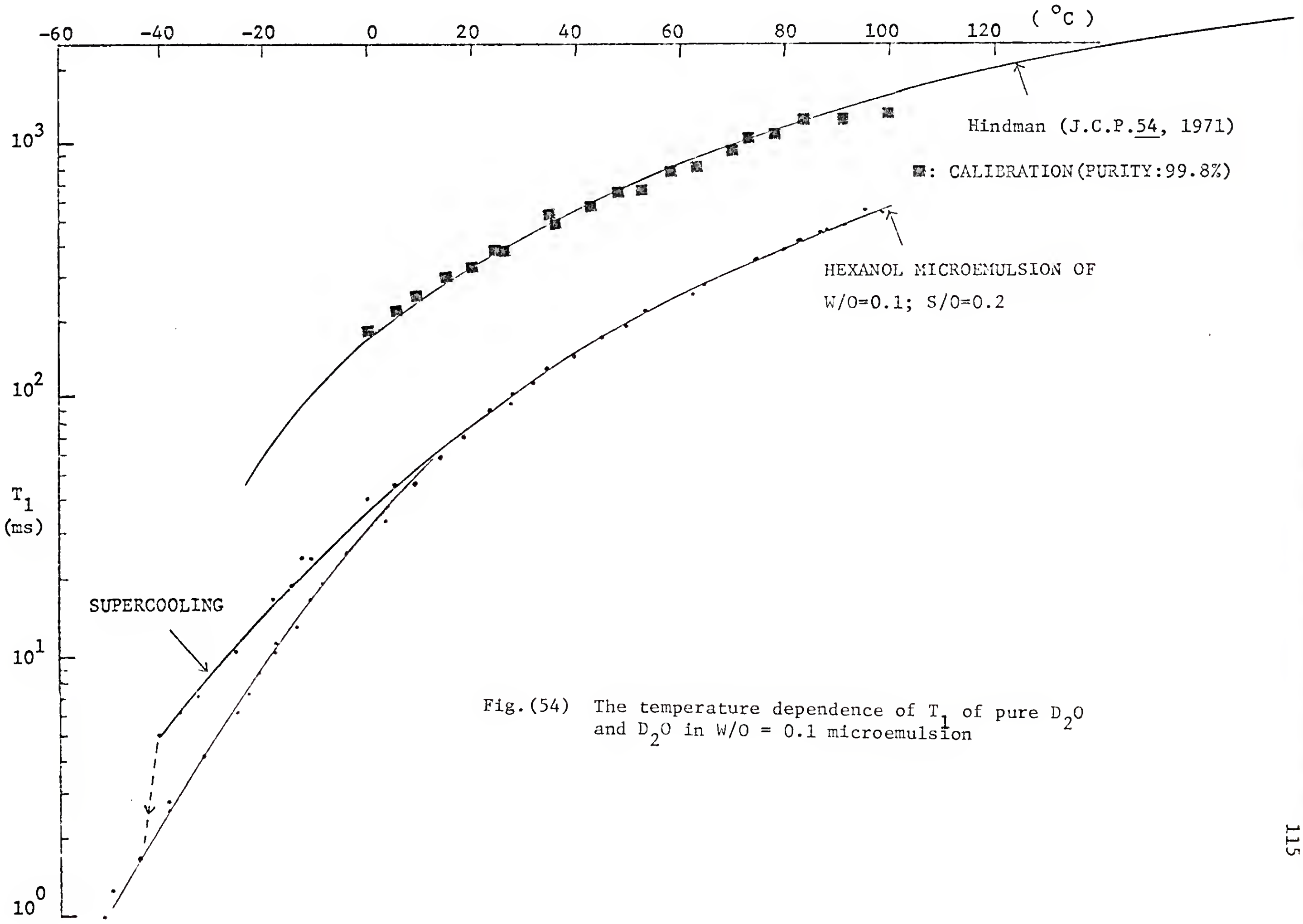

Fig.(54) The temperature dependence of T_1 of pure D_2O and D_2O in W/O = 0.1 microemulsion

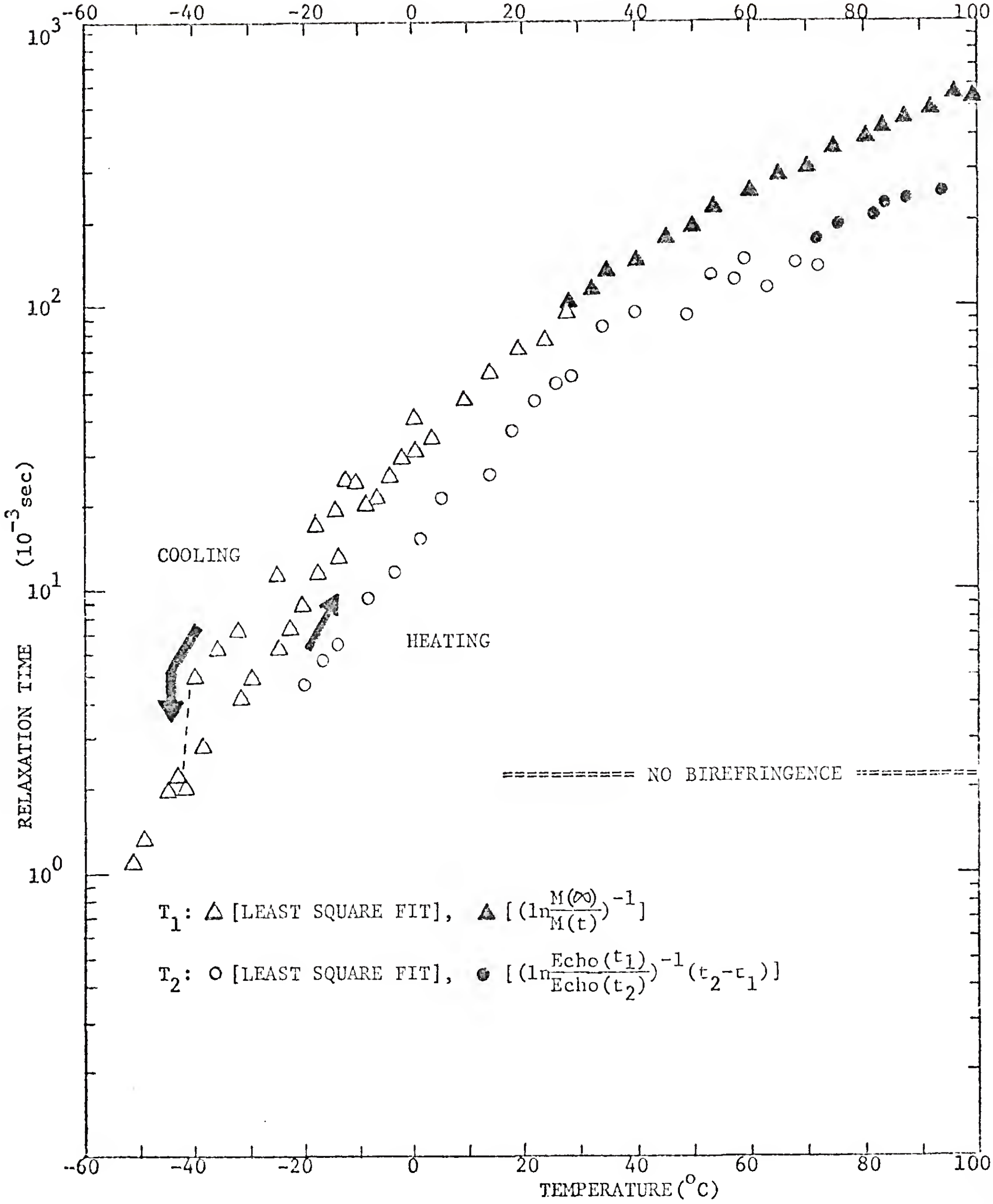

Fig. (55) The temperature dependence of relaxation times of the hexanol microemulsion W/O = 0.1 with S/O = 0.2

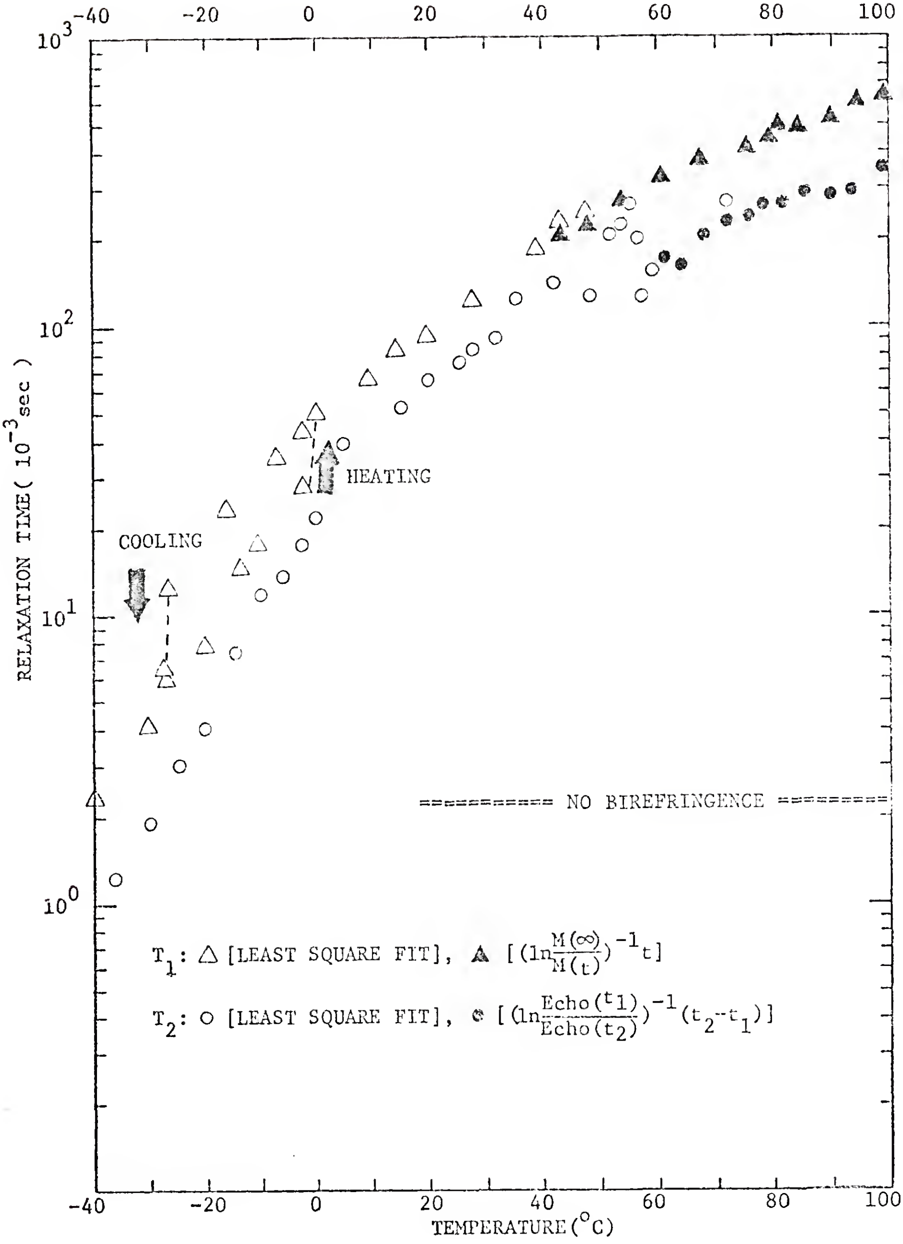

Fig.(56) The temperature dependence of relaxation times of the hexanol microemulsion W/O = 0.2 with S/O = 0.2

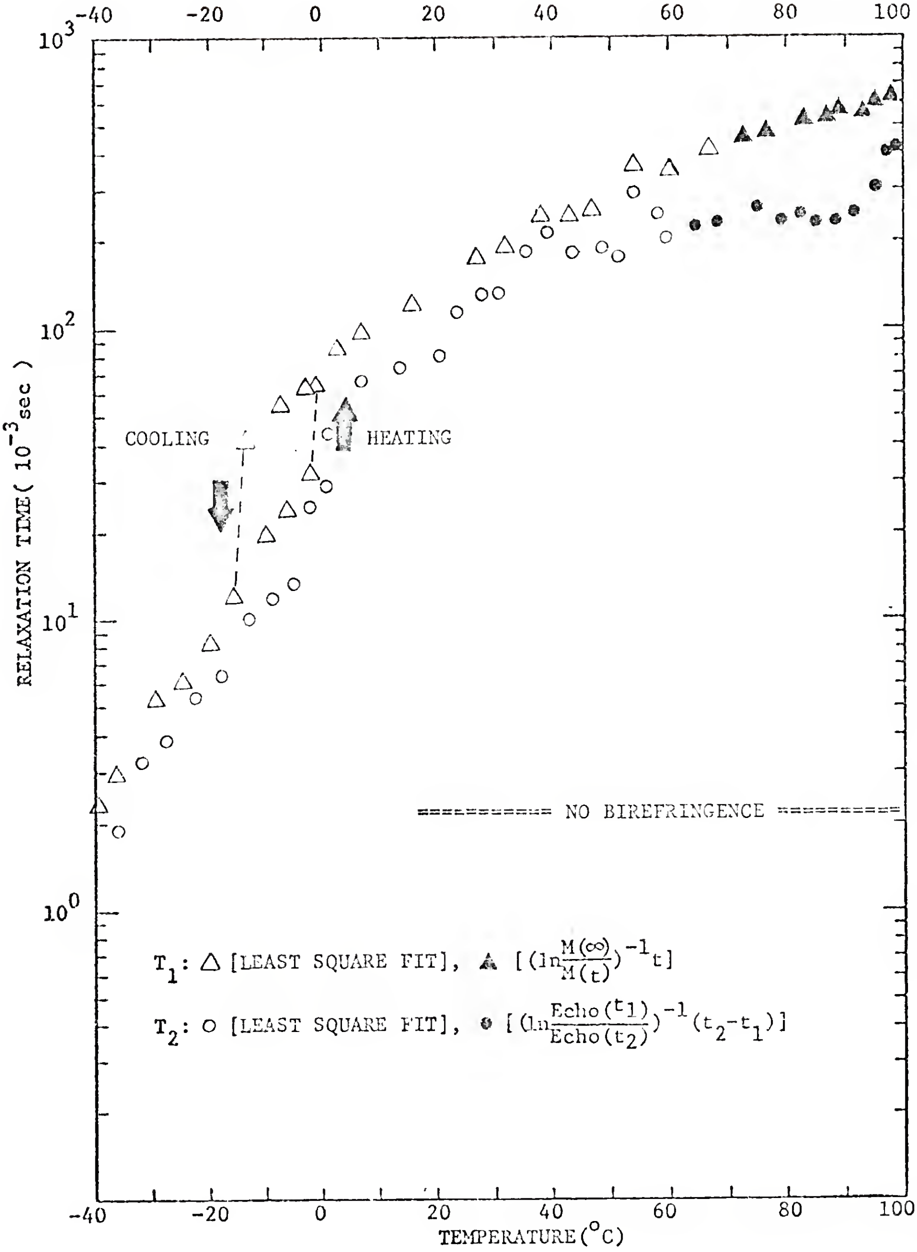

Fig.(57) The temperature dependence of relaxation times of the hexanol microemulsion W/O = 0.4 with S/O = 0.2

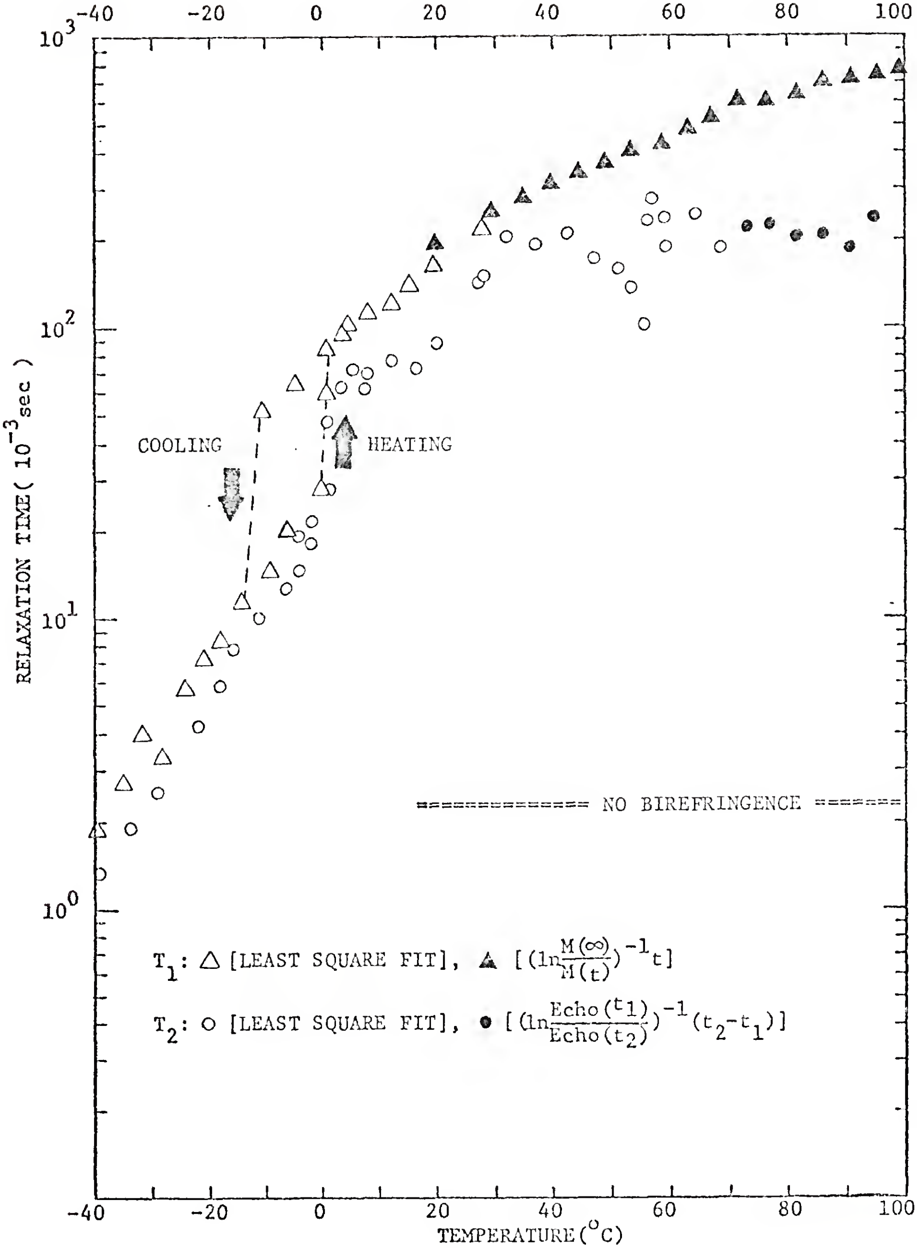

Fig.(58) The temperature dependence of relaxation times of the hexanol microemulsion W/O = 0.6 with S/O = 0.2

is a continuous T_2 decreasing process apparently as compared with figure(16).

An anomaly occurs in the T_2 data of hexanol microemulsions in the region of 50°C. The most probable explanation for this rapid change of T_2 values as shown in Fig.(59) is chemical exchange between the OH group of hexanol and the OD group of D_2O water. The Anderson-Fryer exchange, namely the deuteron exchange between bound and free D_2O molecules, may be another possibility but it would be hard to confirm. In order to investigate chemical exchange, a sample of hexanol microemulsion with composition $W/O = 0.6$; $S/O = 0.2$ was prepared with a mixture of 10% D_2O and 90% H_2O by volume for high resolution NMR(FT) study. High resolution proton spectra were obtained as a function of temperature on a Bruker HX90 spectrometer. The spectrometer was operated at a resonance frequency of 90 MHz. Each spectrum is the result of Fourier transformation of a large number of signal averaged scans.

These spectra are displayed in Figs.(60-64). The complete spectrum as it appears at 80°C is shown in Fig.(60). Only the protons from HC of potassium oleate, the OH of hexanol and water, and the CH_2 of the CH_2OH group in hexanol are well resolved at this temperature. The remaining protons contribute the high intensity structure on the right. At 80°C the OH produce a single narrow peak and thus chemical exchange is rapid and complete between the water and hexanol OH. Figure(61) shows the relevant left portion of the spectrum at 23°C on a 250 Hz full scale sweep [1/4 of the scale of Fig.(60)]. The important fact is that the OH of hexanol and DOH are now partially resolved, with the hexanol appearing as a shoulder on the stronger DOH peak. The fact that these peaks are not completely resolved means that even at room temperature a significant amount of exchange takes place. However, the averaging is only partial and this is therefore a region of intermediate exchange. As the temperature is raised to 60°C, the shoulder disappears [Fig. (62)] and the line shape becomes symmetric. This means that exchange between the two different OH groups becomes rapid enough to cause complete averaging and the two peaks are completely overlapped. As the temperature is further increased to 80°C [Fig. (60) and Fig. (63)], the lines become narrower due presumably to decreasing viscosity of the liquid. The spectra are completely reproducible on thermal cycling. Figure (64) obtained at 23°C only 30 minutes after the 80°C spectrum is again identical with Fig. (61). These results clearly demonstrate that chemical exchange is taking place and is changing in the region where T_2 data show anomalous behavior.

The numerical chemical shift and line width data for the OH are given in Table (6). The shifts are given in ppm relative to the $\underline{CH_2}OH$ peak of hexanol. The strong temperature dependence of the shifts and of the linewidth is to be noted. The chemical shift decreases by about a factor of four. The linewidth reduction occurs mostly above 60°C.

These chemical shift data can be used to estimate the lifetime of the hydroxyl protons bound to hexanol. From Table (6) the average chemical shift difference at 23°C between the two OH peaks is approximately 0.045 ppm, equivalent to 4 Hz at 90 MHz. Therefore the lifetime of the OH is about 250 ms.

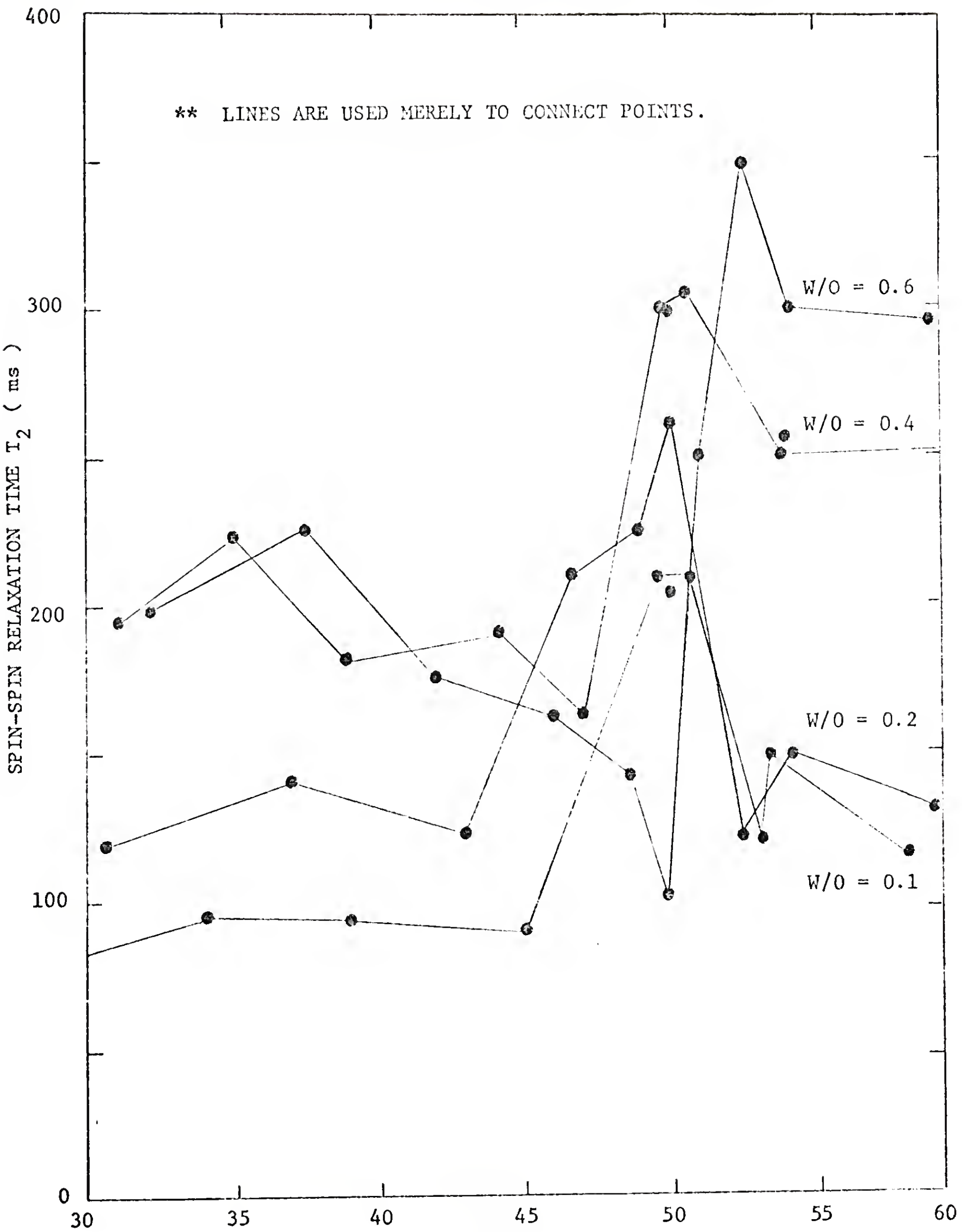

Fig.(59) The temperature dependence of spin-spin relaxation time of the hexanol microemulsions above room temperature

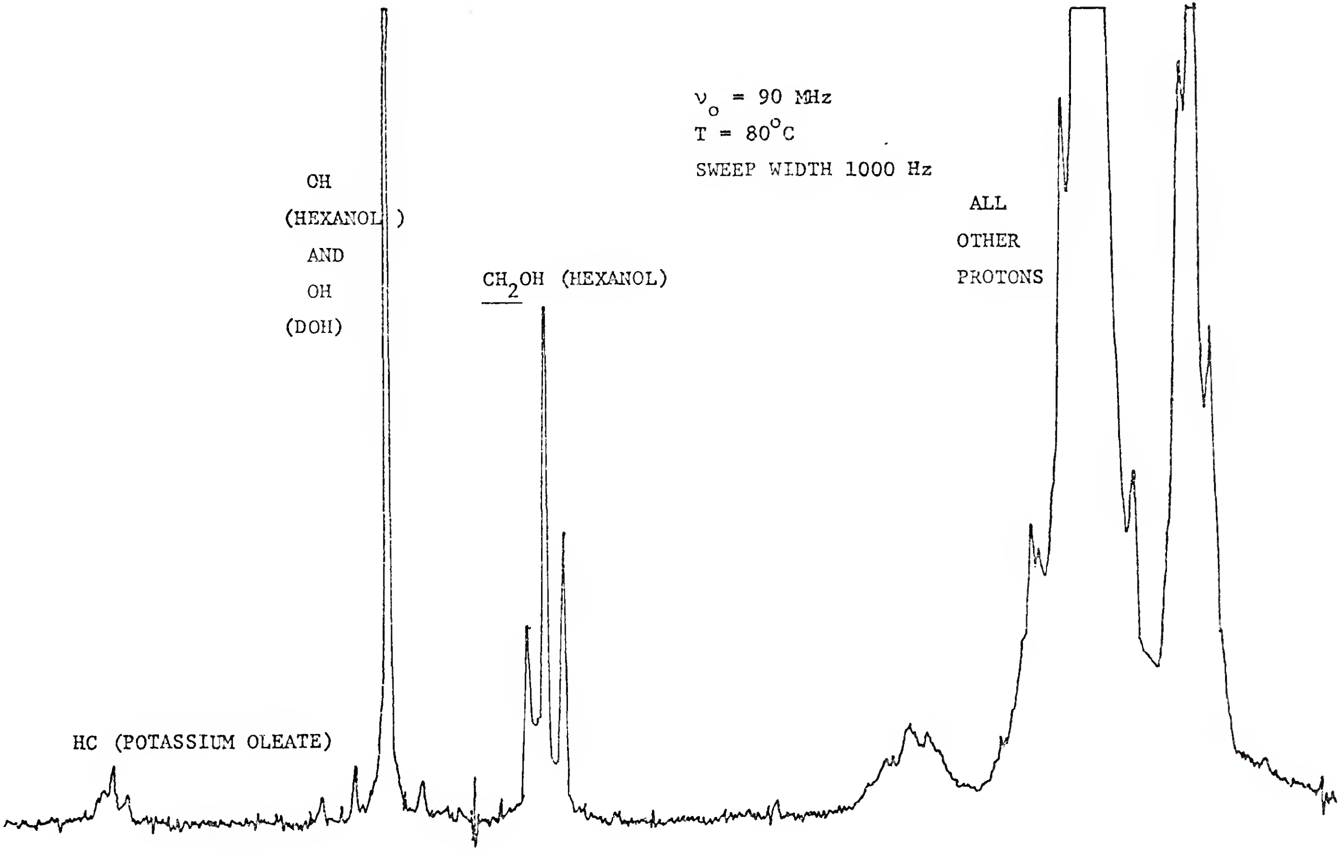

Fig.(60) High resolution NMR spectrum of the hexanol microemulsion W/O=0.6, S/O=0.2 at 80°C

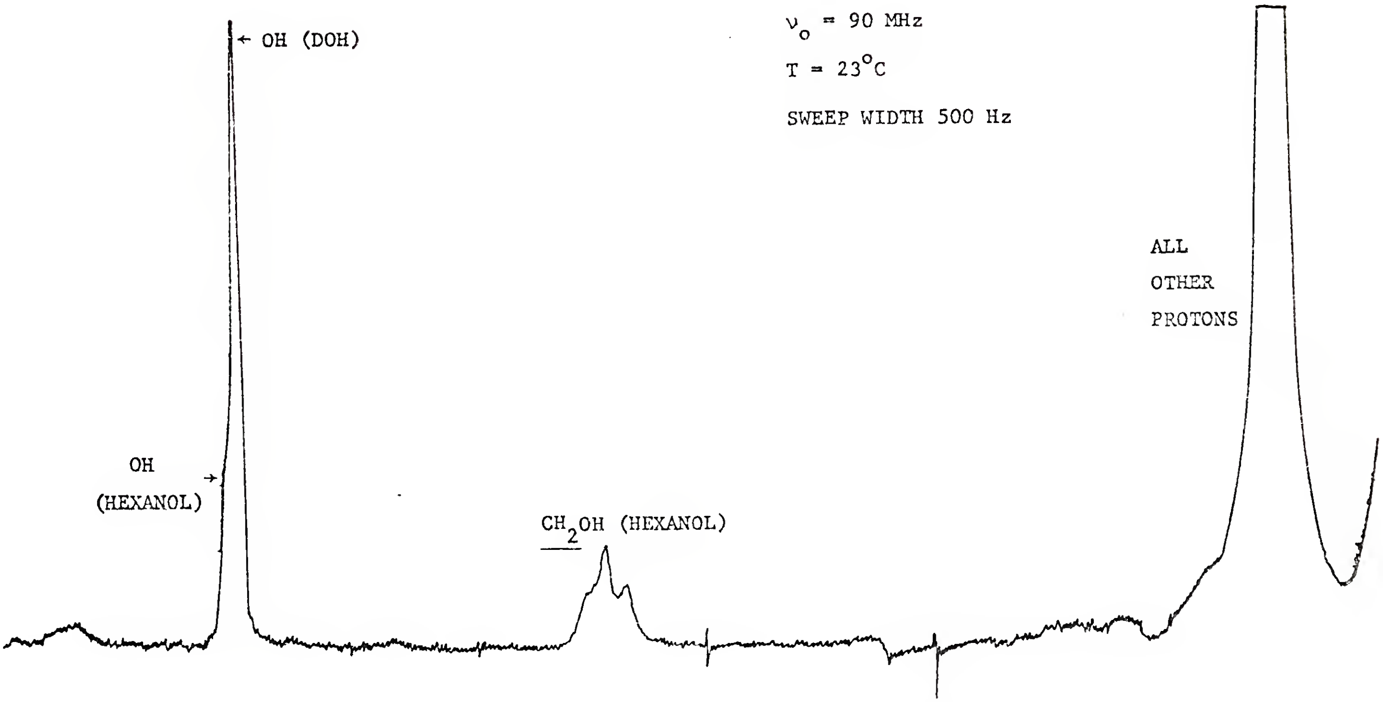

Fig.(61) High resolution NMR spectrum of the hexanol microemulsion W/O=0.6, S/O=0.2 at 23°C

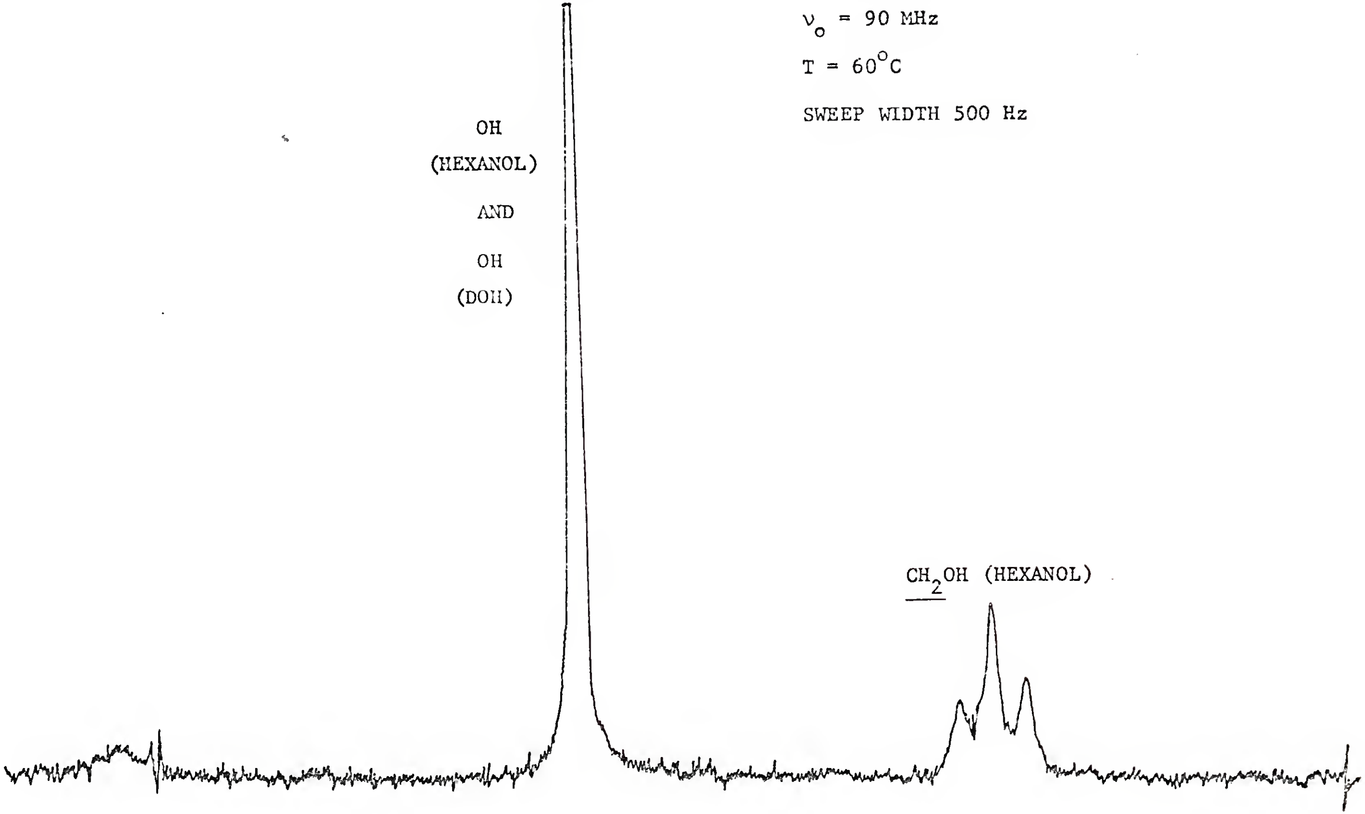

Fig.(62) High resolution NMR spectrum of the hexanol microemulsion W/O=0.6, S/O=0.2 at 60°C

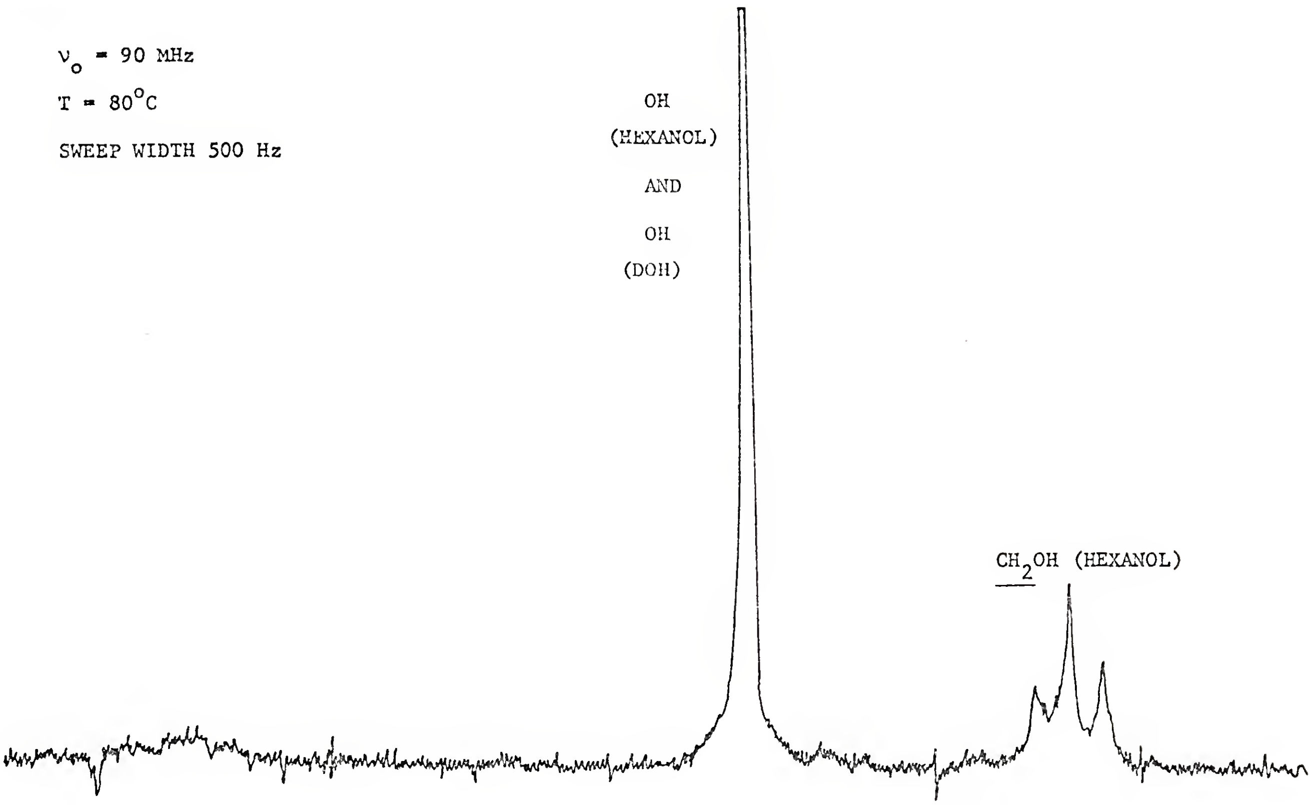

Fig.(63) High resolution NMR spectrum of the hexanol microemulsion W/O=0.6, S/O=0.2 at 80°C

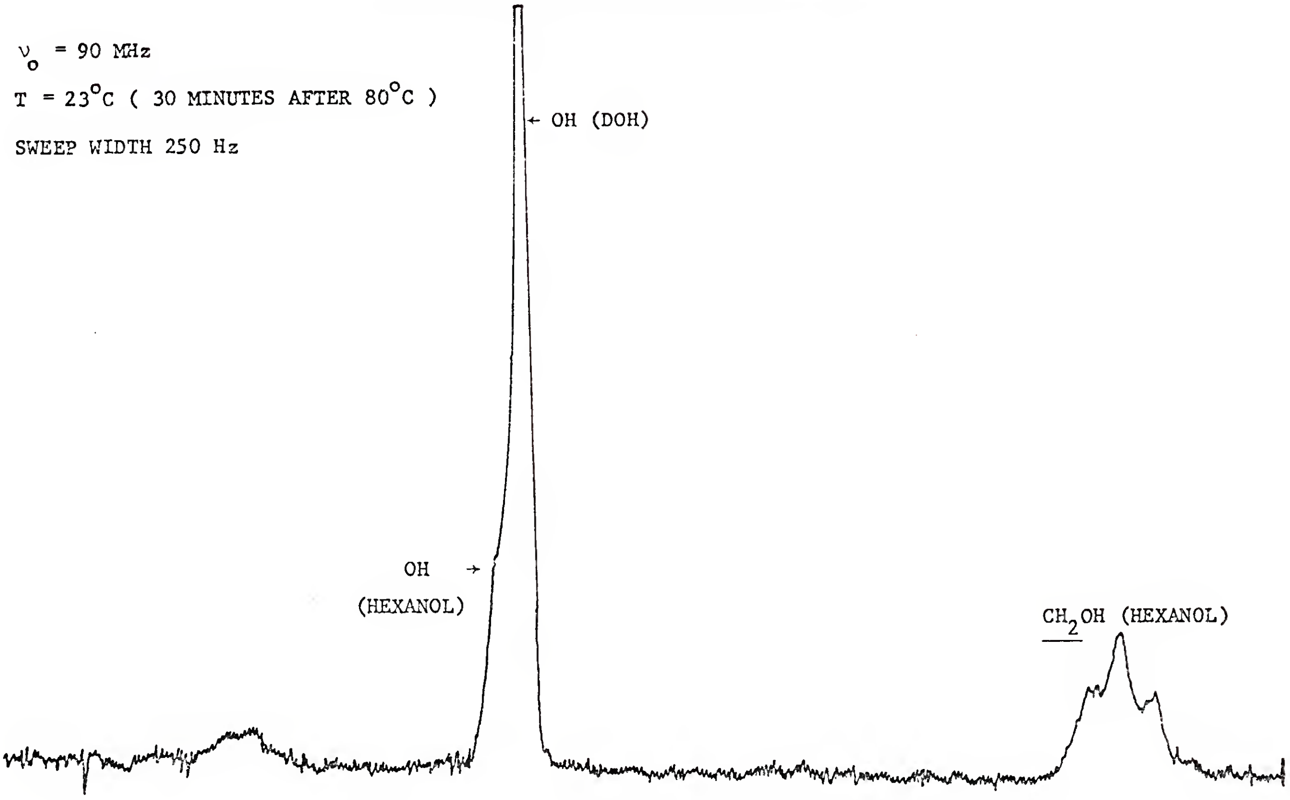

Fig.(64) High resolution NMR spectrum of the hexanol microemulsion W/O=0.6, S/O=0.2 at 23°C (30 minutes after 80°C)

Table(6) Temperature dependence of the OH peaks in the proton spectrum of the hexanol microemulsion system[*]

Temperature (°C)	Chemical Shifts[†]		Full Width of DOH peaks at 1/2 maximum intensity (Hz)
	OH(of hexanol)	OH(of DOH)	
+ 23	∿1.25[§]	1.215	2.2 ± 0.3
+ 60	0.841		∿2.1
+ 80	0.654		0.8 ± 0.3
+ 23	∿1.27[§]	1.215	2.4 ± 0.3

[*] Water/Oil = 0.6 (V/V) (Oil = Hexadecane)

Hexanol/Oil = 0.4 (V/V)

Potassium Oleate/Oil = 0.2 $\mathrm{gm/cm^3}$

[†] ppm from $\underline{\mathrm{CH_2}}\mathrm{OH}$ of hexanol

[§] Shoulder on DOH peak

IV.2 The Liquid Crystals

IV.2.1 Explanation of Line Spectra and Relaxation

In the liquid crystal phase a quadrupole splitting was observed as discussed in section II.5 of chapter II. The quadrupole splittings are on the order of a few hundred Hz, which is much less than the static e^2qQ values of deuterons in H bonds, showing that some degree of motional averaging is effective. This motion is anisotropic, i.e., the D_2O molecules maintain a small degree of preferential orientation, or else e^2qQ would be zero. The observation that the spectra are powder patterns indicates an interpretation where the water molecules are mostly contained in lamellae comprising domains. Within these domains water molecules may be "free," having no preferential orientation and zero quadrupole interaction, or bound to the surfactant layer with a prefered orientation and a net interaction. Therefore, the observed quadrupolar interaction $< X > = P_f X_f + P_b X_b = P_b X_b$. The orientation of the domains relative to the laboratory, i.e. the applied magnetic field, is random. As the quadrupole splitting is orientation dependent a characteristic powder pattern is observed. The patterns observed are characteristic of a system possessing axial symmetry. The dimensions of the domains are sufficiently extensive that water molecules evidently do not diffuse from one domain to another during the characteristic time of the NMR experiment. At junctions between domains there will be regions of disorder where D_2O molecules will tumble isotropically. X_b is expected to be a function of temperature decreasing with increasing temperature whereas P_b is expected to be a function of composition, proportional to the area of the water/oil interface.

Figure(65) and Fig.(66) show the wide line shape of a typical lamellar hexanol liquid crystal W/O = 1.4 at different temperatures. The two types of water have different relaxation times which are temperature dependent. Below the freezing point of about 4°C, the formation of ice crystals evidently disrupt the surfactant layer, and releases some of the trapped water which then becomes mobile and gives rise to the prominant narrow central line. Eventually the wide line completely disappears. The relatively broad central line is actually a collection of many narrow lines which are overlapped by broadening at lower temperature. The central line will disappear also when the temperature is cooled further. The unobserved intensity is presumably spread over several hundred kHz, characteristic of rigid D_2O.

In a heating measurement above room temperature we also observe growth of the central line due to thermal agitation. Above a certain temperature, the wide line disappears due to phase separation and disruption of the lamellar structure resulting in smaller domains with an increased probability of water molecule transfer between domains.

For further quantitative comparison, we introduce Fig.(67) to show the correspondence of the true line shape to the derivative mode. Therefore, we can calculate T_2 by using the formula $T_2 = (\pi\ 3^{1/2}\ W)^{-1}$. W is the line width of a single line, $\Delta\nu$ is the line splitting corresponding to $\frac{3}{4}(e^2qQ)_{obs.}$ as shown in Fig.(25). W is a sum of intrinsic width and broadening contributed by magnetic field inhomogeneity W'. From experimental data, W' can be as large as ±30 Hz. The calculated T_2 varies from 1.22 to 2.1 ms over a wide range of temperature and this is comparable with 2.1 ms measured by the spin-echo pulsed method

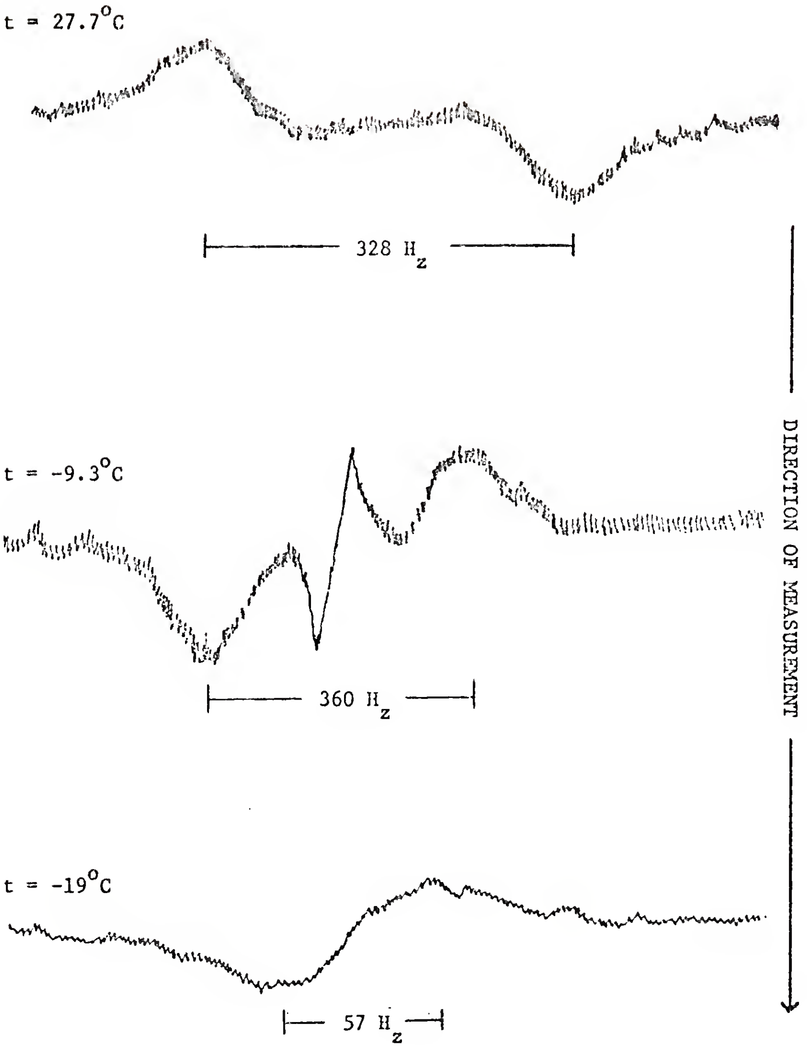

Fig.(65) Line shape variation of the liquid crystal W/O = 1.4 with S/O = 0.2 obtained on cooling the sample from room temperature to -19°C (vertical scale is arbitray)

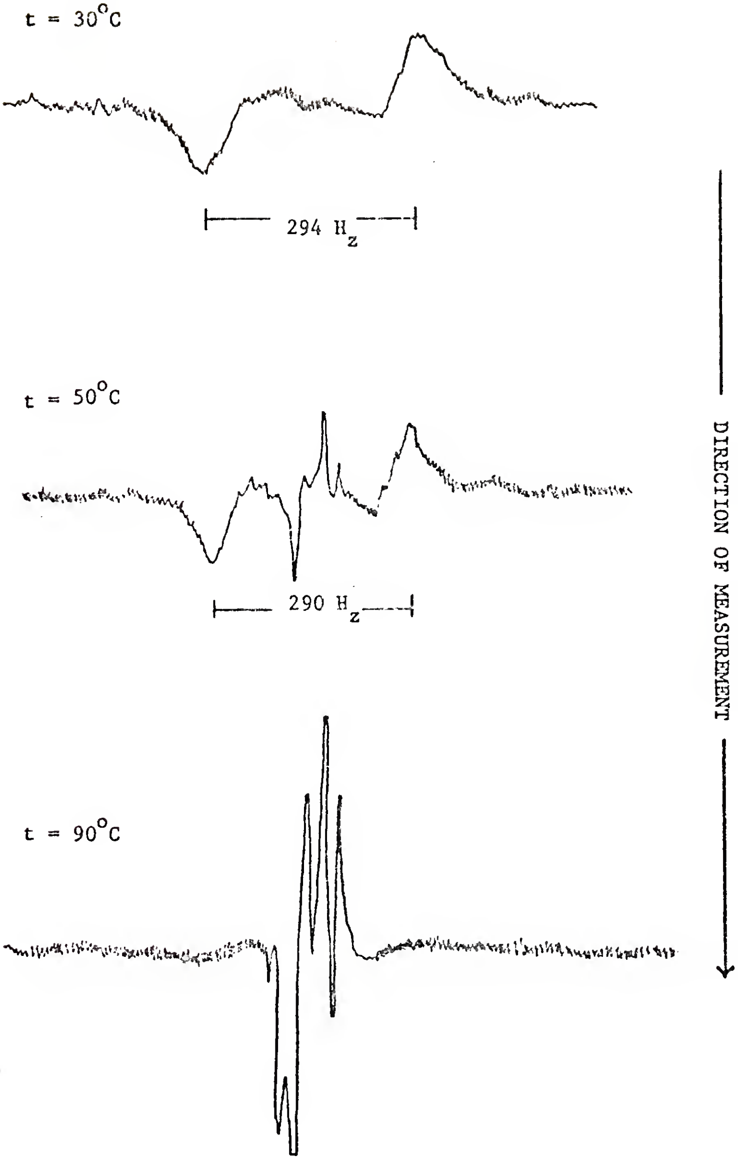

Fig. (66) Line shape variation of the liquid crystal W/O = 1.4 with S/O = 0.2 obtained by heating the sample from room temperature to 90°C (vertical scale is arbitrary)

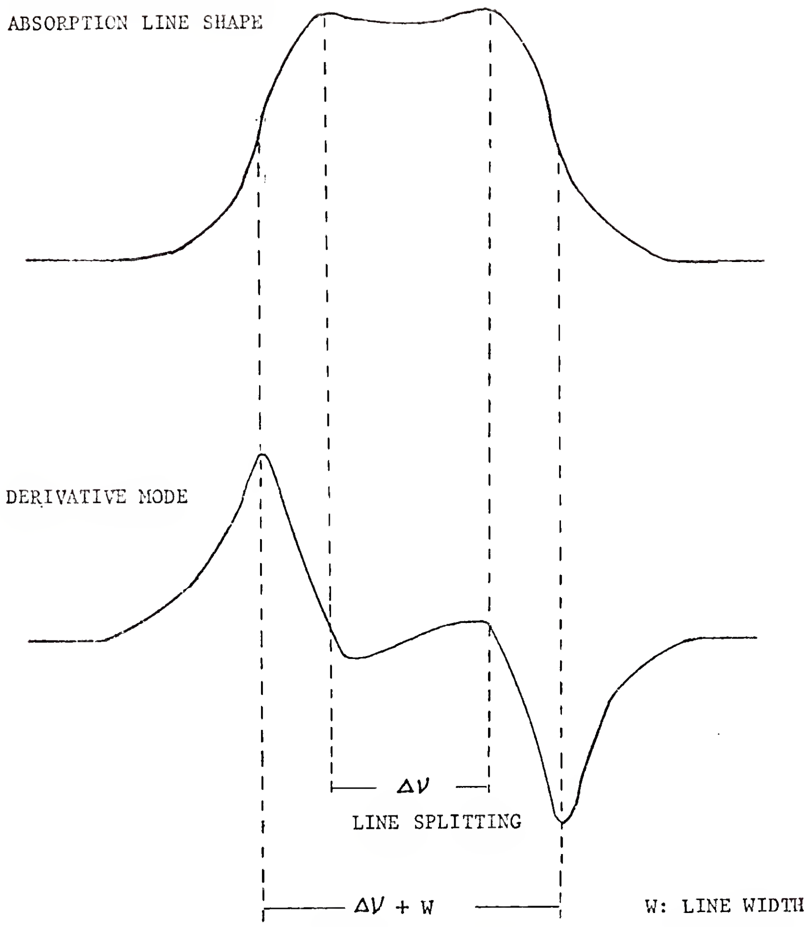

Fig.(67) The powder-pattern wide-line spectra in the derivative mode and the corresponding absorption line shape as shown in Fig.(73). The quadrupole splitting $\Delta\nu$ is about 200±10 Hz over a wide range of temperatures.The chief source of uncertainty in the splitting is due to the growth of the central peak as the temperature is lowered, which superposes it on the wide line spectra.

As to the hexanol cylindrical liquid crystal W/O=1.0, a larger splitting (about 275±10 Hz) is observed, but the line width is about the same as for the sample with W/O=1.4 and fluctuates around 120±30 Hz, over a wide range of temperature. This is also verified by the pulsed method to have the same T_2 values of 2.2 ms[Fig.(71)]. The larger quadrapole splitting means less motional narrowing. This is reasonable because the cylindrical rods, with diameter roughly 100 Å, has more restriction for the polar groups of the surfactants than does the lamellae W/O=1.4.

The results from the pulsed method indicate, that the T_2 curve of the liquid crystals has thermal hysterisis below the freezing point. In the supercooling region, the liquid crystal's geometry has not been destroyed by ice crystal yet, the short T_2 spin-spin relaxation time is still dominated by the bound water contribution. Once the ice crystal aggregates are large enough to disrupt the boundaries, the remaining water can travel around more freely as mentioned before, and we observe a much larger T_2 , which again decreases when the temperature is cooled further. In the heating process, the liquid crystal structure by freezing is limited in local area, because rapid melting starting from a temperature colder than the lower limit of supercooling quickly restores the same short T_2 value. But this is not true in the case of phase separation in the higher temperature region. The same separation point is always observed on heating. But if we cool down rapidly from an initial temperature above the phase separation point, we do not observe a short T_2 right below the separation temperature; instead it takes many hours or a day for T_2 to return to its original value.

The liquid crystal W/0 = 1.2 has its composition between that of cylindrical rod and lamellae. This sample has a quadrupole splitting $\Delta\nu = 220 \pm 10$ Hz over a wide temperature range, smaller than that of W/0 = 1.0 but larger than that of W/0 = 1.4 obtained from CW-measurement. The line width of the main peaks is about the same as in the other two samples. This sample produces two kinds of spin echoes corresponding to two different T_2 values in the temperature range from -2°C to 18°C. These values are denoted by ◻ in Fig.(72). This kind of two features coexistance stops before room temperature, visual observation provides no information on this region because, hexadecane freezes and the sample becomes opaque at 18°C. Above 18°C, the spin echo returns to one feature.

All those samples of the liquid crystal have significantly increased T_2 values after violent shaking as shown in Fig.(70). This is very similar to the T_2 increasing after freezing because of local disruption of the structure affecting the motion of water molecules. As observed from CW spectra, shaking makes the cut-off frequency due to quadrupole splitting of powder pattern more apparent as may be seen by comparing Fig.(65) with Fig.(68) and Fig.(69).

The composition dependence of the quadrupole splitting and the width of the wide line are listed in Table(7). Visual observation verifies the temperature of phase separation is the same as the temperature obtained from the relaxation time measurement.

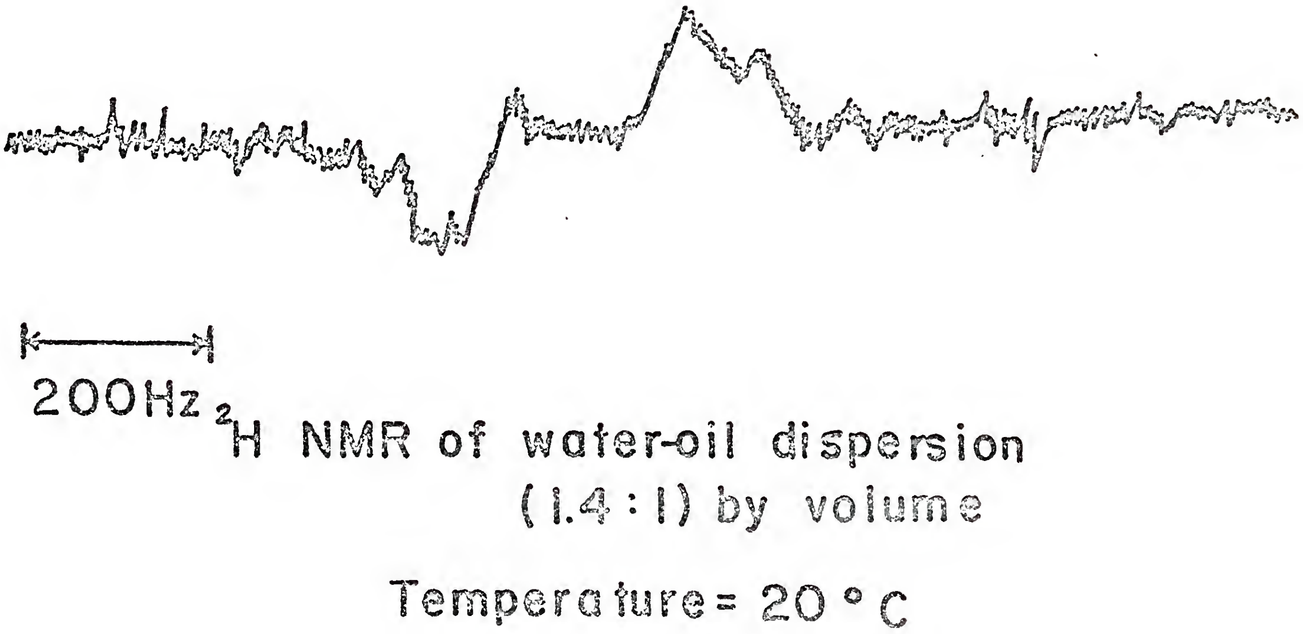

Fig.(68) The wide line spectrum of the hexanol liquid crystal W/O= 1.4 with S/O= 0.2 after shaking

W/O= 1.0 at t= 24.5°C

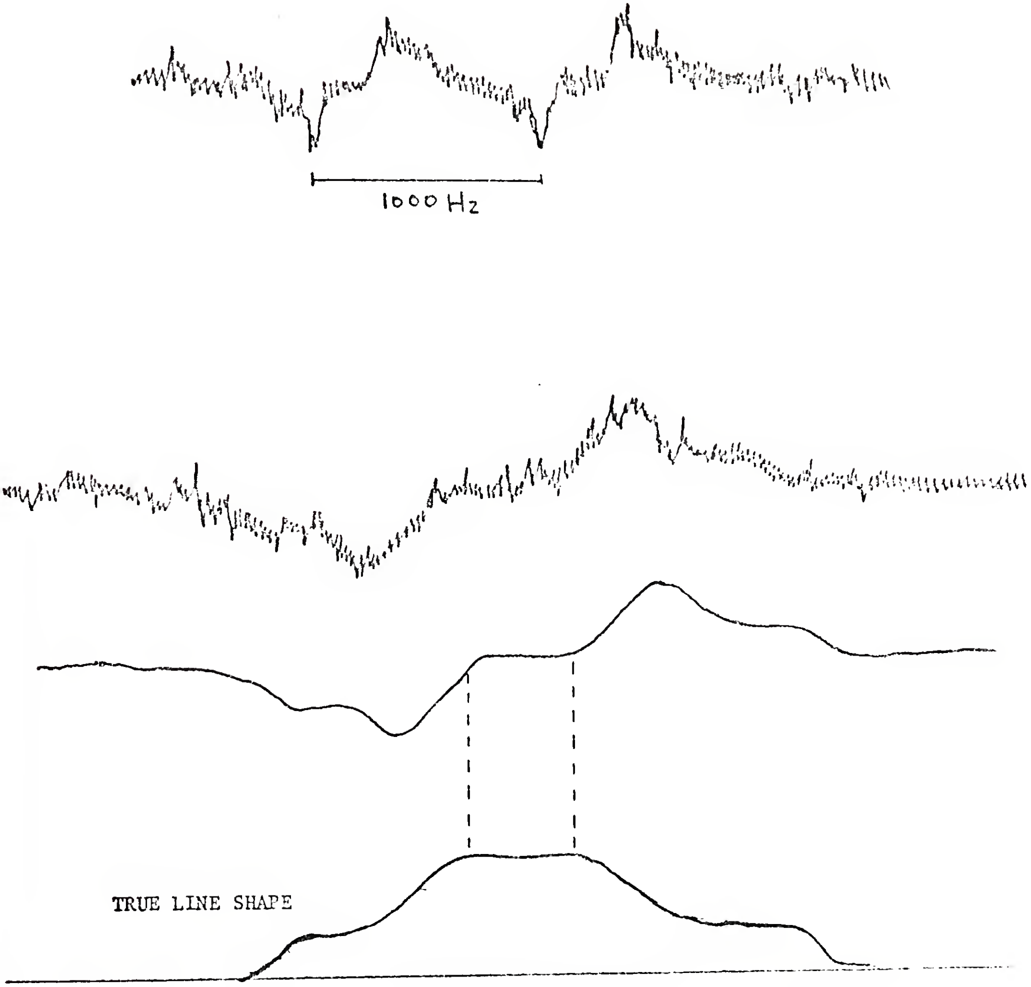

Fig. (69) The wide line spectrum of the hexanol liquid crystal W/O = 1.0 with S/O = 0.2 after shaking

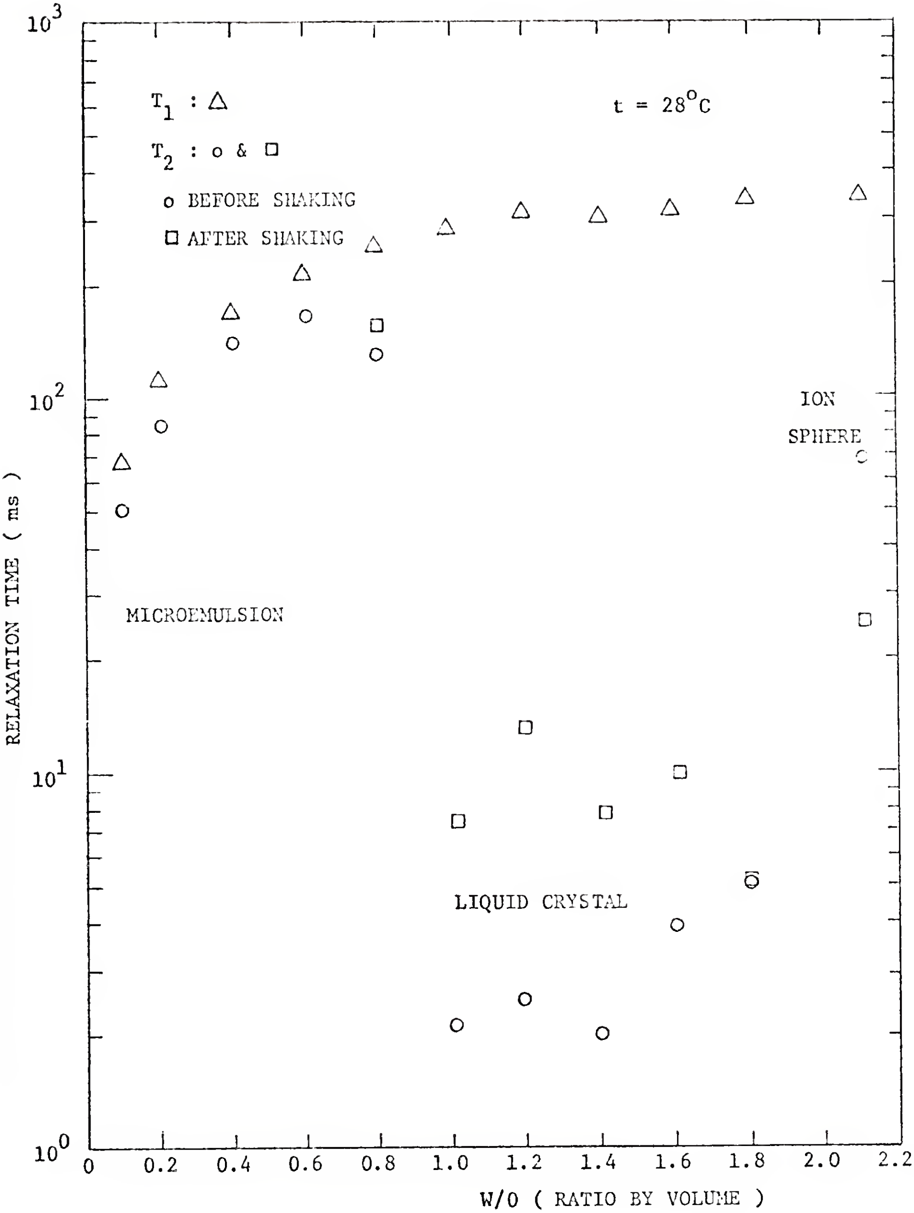

Fig. (70) The composition dependence of the relaxation times of the hexanol system

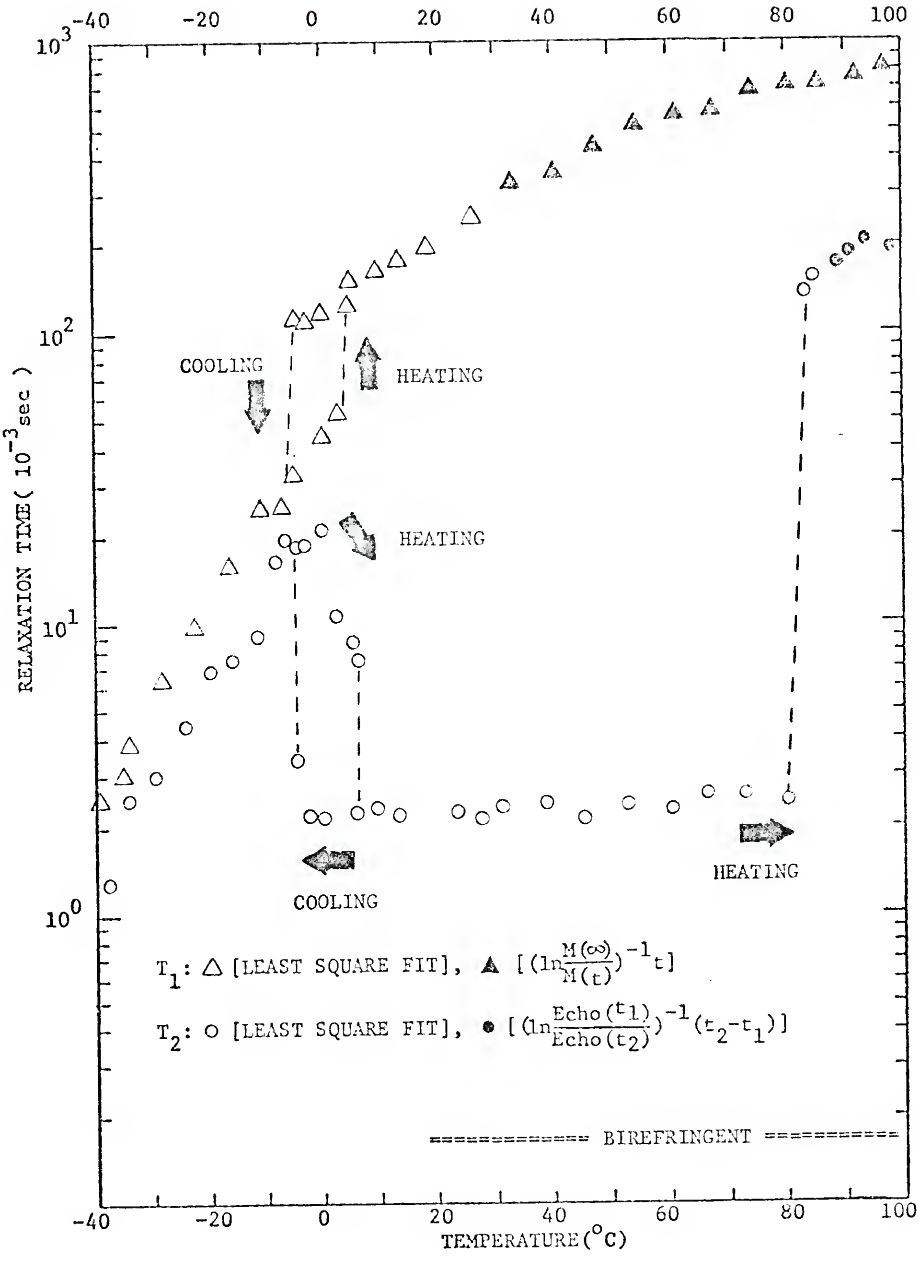

Fig.(71) The temperature dependence of the relaxation times of the hexanol liquid crystal W/O = 1.0 with S/O = 0.2

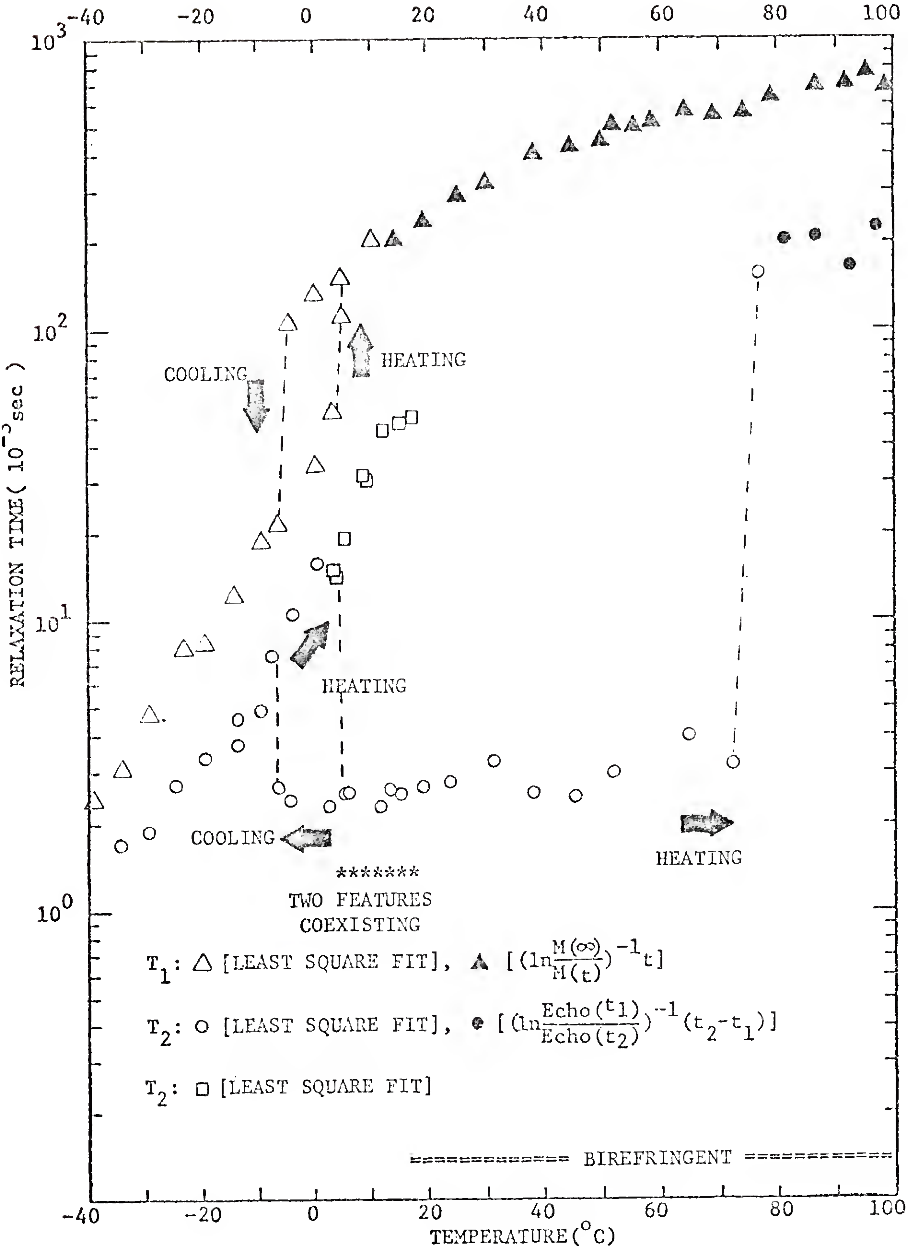

Fig.(72) The temperature dependence of the relaxation times of the hexanol liquid crystal W/O = 1.2 with S/O = 0.2

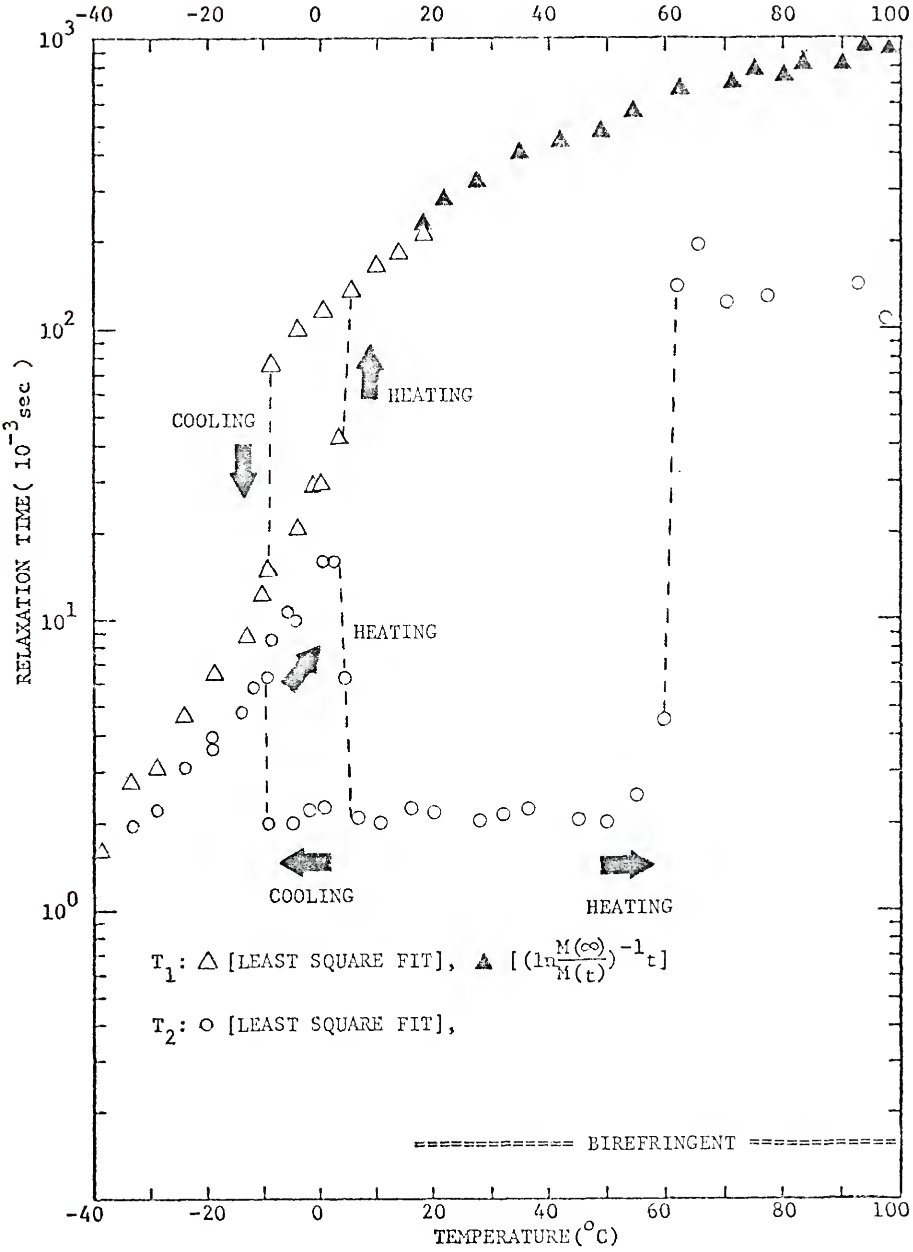

Fig.(73) The temperature dependence of the relaxation times of the hexanol liquid crystal W/O = 1.4 with S/O = 0.2

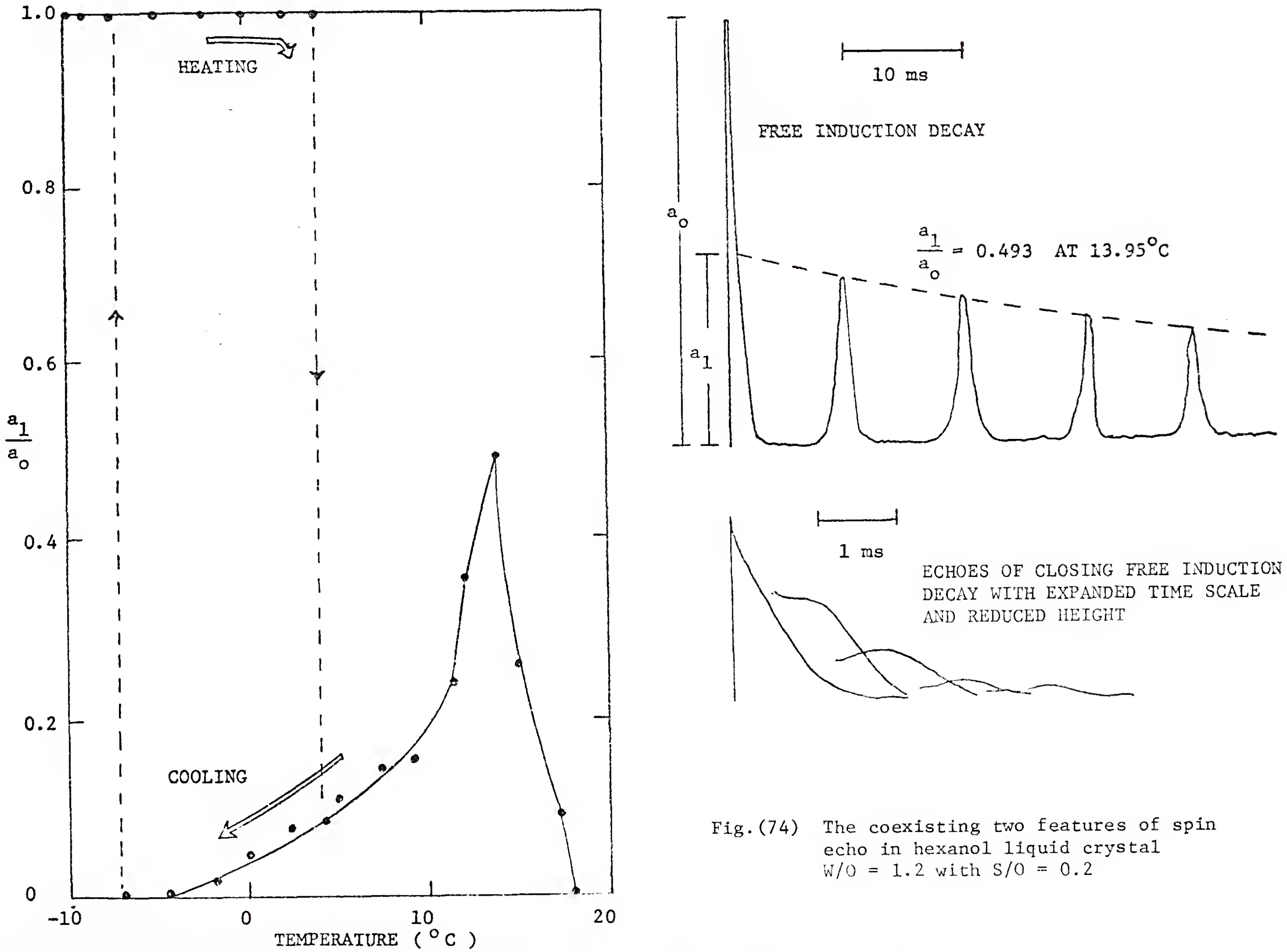

Fig.(74) The coexisting two features of spin echo in hexanol liquid crystal
W/O = 1.2 with S/O = 0.2

Table(7) The composition dependence of quadrupole splittings and widths of the wide lines

W/O	$\Delta\nu$ (Hz)	W (Hz)
1.0	275 ± 10	120 ± 30
1.2	220 ± 10	120 ± 30
1.4	200 ± 10	120 ± 30

** The above data are taken at 28°C, but are true over a wide range of temperatures during which the liquid crystal structure remains.

IV.2.2 Motional Narrowing of the Quadrupole Splitting

The quadrupole splitting of several hundred Hz in the liquid crystal is much smaller than the value estimated by using the relation(II.5.12).

$$\Delta\nu = \frac{3}{4}\left(\frac{e^2 qQ}{h} \right)_{obs.} = \frac{3}{4}(258.6 \text{ kHz}) \times \frac{\Delta}{d} = 2.42 \text{ kHz} \qquad (IV.2.2.1)$$

where Δ is the thickness of the bound water layer of roughly about 1.25 Å, d is the thickness of a single water layer trapped by surfactant interfaces of roughly about 100 Å. This indicates a considerable amount of additional time-averaging of the electric field gradients giving rise to the splittings. Such time averaging may be caused by three origins: (I) 180° flip of the bound D_2O molecules, which immediately reduces the electric field gradient to one half, and other modes of motion such as vibration etc., (II) tumbling of the water molecules by thermal motions while being constantly bound and released from the binding sites, (III) motion (within the relevant time scale) of the group to which the water is bound. The last possibility is probably more important in the case of the lamellar liquid crystals than for the cylindrical case, because the packing of the polar groups of the surfactants on the flat interface is not so tight as it is on the curved interface. The relative immobility of polar groups on the curved interface, micro-emulsions for example, has been demonstrated in a high resolution NMR study on the surfactants by Hansen [41]. This effect explains why the cylindrical rod phase(W/O=1.0) gives a slightly larger characteristic splitting, because the circular geometry of the cylindrical rod makes the polar groups more restricted in motion. If this possibility dominates, the water molecules provide a useful and non-perturbing probe for investigating motions of the binding groups. If the second possibility dominates, the deuteron NMR spectrum should be determined primarily by the energy of binding of the water of hydration. It is informative to establish the set of relevant time scales before going further.

The criterion for the start of motional averaging is that the frequency of the averaging process be comparable to the transition frequency between the nuclear energy levels. In a sample containing all possible orientations of the OD bonds, only a mean value can be used for the critical frequency; this is of the order of $(\frac{e^2qQ}{h})$ for a rigid lattice D_2O molecule, giving a critical timescale for the averaging process of about 10^{-5} sec. Averaging processes occurring over a longer timescale than this are unobserved and one obtains only a spatial averaging of the electric field gradients, producing the characteristic powder spectrum. In order to determine whether motion of the binding group does contribute to the narrowing of the splitting of the water resonance, it is therefore necessary to consider the correlation time of water, since it is not clear which modes of the polar groups are relevant.

If we take the liberty to choose the activation energy of the binding site as 3 kcal/mole from Fig.(16) by assuming an isotropic rotational motion[25], the rate to disrupt the water binding group will be on the order of $(\frac{e^2qQ}{h}) \exp(-3 \text{ kcal}/RT) \simeq 10^{11} \text{ sec}^{-1}$. If any free water molecule has its correlation time shorter than 10^{-11} sec, then the reorientation between free and bound molecule is possible. The rotational correlation time of a free water molecule is generally about 10^{-12} sec, thus we expect the rapid bonding and releasing from the binding sites occurring.

For the bound-free two state model, we need two correlation times to characterize the motion. Therefore,

$$\tau_c = \frac{\Delta}{d} \tau_c^b + (1 - \frac{\Delta}{d}) \tau_c^f \quad , \qquad \text{(IV.2.2.2)}$$

and d have been defined i.e., Δ = thickness of the bound water layer and d the thickness of water between surfactant interfaces. Since the T_2 values of the liquid crystal region in Fig.(71-73) are so different from those of the isotropic case (about 10^{-2} factor of the T_2 in microemulsions, which experience rapid exchange between bound and free water), it is reasonable to assume $\tau_c^b >> \tau_c^f$.

Therefore,

$$\tau_c \simeq \frac{\Delta}{d} \tau_c^b \qquad \text{(IV.2.2.3)}$$

In the special case of rapid reorientation about an axis which itself tumbles fairly slowly, only the tumbling will determine the relaxation rates. Woessner[42][43] provides the theoretical treatment in this special case and obtains the equations

$$\frac{1}{T_{1,2}} = \left(\frac{1}{T_{1,2}} \right)_{\text{isotropic}} \times \frac{1}{4} \left(3 \cos^2\psi - 1 \right)^2, \tag{IV.2.2.4}$$

where $(T_{1,2})_{\text{isotropic}}$ are given by

$$\left(\frac{1}{T_1} \right)_{\text{isotropic}} = \frac{3}{80}\left(\frac{e^2qQ}{\hbar}\right)^2 \left(\frac{2\,\tau_c}{1 + \omega_o^2\,\tau_c^2} + \frac{8\,\tau_c}{1 + 4\omega_o^2\,\tau_c^2}\right) \tag{IV.2.2.5}$$

$$\left(\frac{1}{T_2} \right)_{\text{isotropic}} = \frac{3}{80}\left(\frac{e^2qQ}{\hbar}\right)^2 \left(3\tau_c + \frac{5\,\tau_c}{1 + \omega_o^2\,\tau_c^2} + \frac{2\,\tau_c}{1 + 4\omega_o^2\,\tau_c^2}\right). \tag{IV.2.2.6}$$

Here $\omega_o^2\tau_c^2$ is no longer much smaller than 1. We have to use (IV.2.2.5) and (IV.2.2.6) instead of (II.3.5). ψ is the angle between the axis of fast rotation and the principal axis of the electric field gradient tensor(OD bond). Since the relaxation time measurement gives a very similar result, we can take just one typical case of W/O = 1.4 at 28°C. T_1 and T_2 are 270 and 2.1 ms respectively. We obtain $\tau_c = 0.32 \times 10^{-6}$ sec by dividing the two Woessner equations (IV.2.2.4) with $\omega_o = 2\pi \times 6.5 \times 10^6$ radians/sec. This τ_c is for the slowest component of the motion of the bound water. τ_c is quite close to $\frac{\omega_o}{2\pi} = 0.154 \times 10^{-6}$ second. This explains roughly why the quadrupole splittings of the liquid crystals are so small.

IV.3 Comparison between Hexanol and Pentanol in the Water-Oil System

IV.3.1 Electrical Conductivity Differences

In the paper "Some Structural Aspects of Microemulsions and Cosolubilized System" by Shah, Walker, Hsieh, Nelander and Pepinsky (Presented in the Improved Oil Recovery Symposium of the Society of Petroleum Engineers of AIME in Tulsa, Okla., March 22-24, 1976) it is reported that the electrical resistance of microemulsions containing hexanol and pentanol as the cosurfactant have dramatic differences. (Microemulsion System: hexadecane + potassium oleate + cosurfactant + water.)

Figure(75A) and Fig.(75B) are reproduced from this paper. A cosolubilized solution model was proposed to explain the low resistivity of the pentanol system. There is no explanation for why the addition of one more 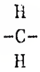 $\overset{H}{\underset{H}{-C-}}$ group to pentanol causes such dramatically different results.

Measurements of the NMR relaxation times T_1 and T_2 obtained by the spin-echo method provide new information for comparing these two systems. This evidence is discussed in the following subsections.

IV.3.2 Experimental Evidence and Explanation

For comparison, relaxation times T_1 and T_2 of deuterons were measured over a wide range of composition in the oil/water systems containing hexanol and pentanol. Data at room temperature are shown in Fig.(70) and Fig.(76). We observe that the pentanol system starts having liquid crystalline properties (low T_2 value of about a few miliseconds) with lower water/oil ratio than that of the hexanol system.

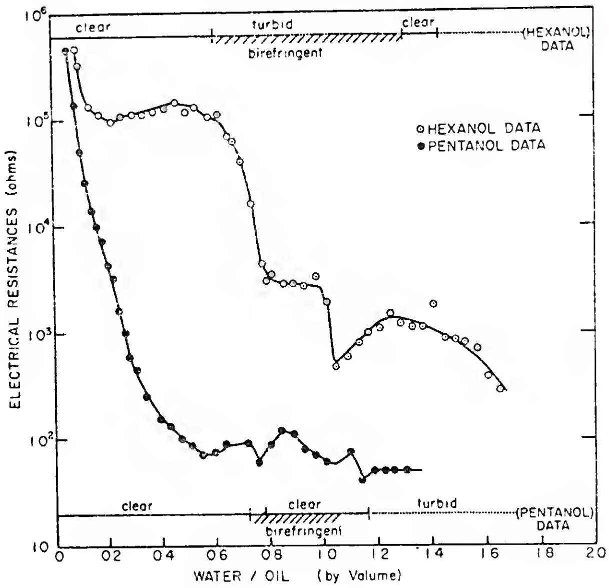

Fig.(75A) Electrical resistance of microemulsions containing hexanol or pentanol as cosurfactant (Microemulsion system: water + hexadecane + potassium oleate + cosurfactant)

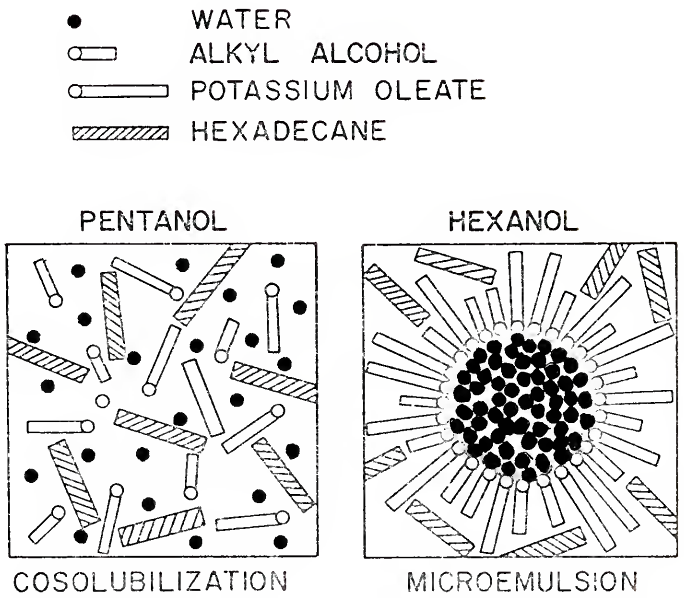

Fig.(75B) Schematic representation of cosolubilized and microemulsions system

The hexanol system is a perfect microemulsion for the composition W/O = 0.6, but the pentanol system is not. Careful relaxation measurements of pentanol W/O = 0.6 were made from $-40^{\circ}C$ to $100^{\circ}C$. Below $25^{\circ}C$, we observed an abnormal spin echo envelope. Normally, the envelope of the spin echoes starts at the peak of the free induction decay. As we see in Fig.(77) although the free induction decay is large, the echoes are much smaller than would be expected. We do not observe another feature of echoes associated with short T_2 as has been observed in the hexanol liquid crystal W/O = 1.2 in the lower right portion of Fig.(74). This implies the envelope of the short T_2 coincides with the free induction decay with $T_2 = T_2^+$, where $(T_2^+)^{-1}$ is approximately the half width at half intensity of the free induction decay due to the field inhomogeneity. The T_2^+ value is about 0.7 ms. This situation with short T_2 is similar to the liquid crystal behavior. Figure(78) shows an intermediate range between microemulsion and liquid crystal behavior at different temperatures. At $5^{\circ}C$, a strong liquid crystalline tendency is apparent ($a_o - a_1 \simeq 1$) whereas near room temperature liquid crystalline tendency is minor ($a_o - a_1 \simeq 0$).

Similar phenomena occurs at lower temperature. In Fig.(79), graph(a) shows spin echoes of the normal type at $-6.98^{\circ}C$. Graph(b) and graph(c) show that the train of echoes disappear completely when cooled down to $-9.3^{\circ}C$; the observed T_2 is then only $T_2 = T_2^+ = 0.72$ ms. Graph(d) and graph(e) show the echoes reappear on further cooling and reach their normal type at $-13.95^{\circ}C$. These observations are reversible on thermal cycling. The small hump of spin echoes in both graph(b) and graph(d) is believed to be a modulation of the spin echoes due to the coupling (dipolar or scalar) between the resonant and nonresonant deuteron spins subject to the local field inhomogeneity [44],[45],[46],[47].

The results of visual observation indicated in Fig.(80) are that the pentanol dispersion W/O = 0.6 gives a dark pattern for all angles of the two polarized plates relative to each other at room temperature. In the normal microemulsions or cosolubilized molecular solutions, we expect to see the brightest clear pattern when we orthogonalize the polarized plates because, the scattered light has its biggest intensity at 90° as we view it from the front side of the light source. If it is a liquid crystal phase with its grating-like "slit" width comparable to the visible light wave length, we will see interference patterns over a wide range of rotating angle. The normal hexanol liquid crystals with their "slit" width of about roughly 100 Å (the width measured with electronmicrograph by Shah and Pepinsky in the paper mentioned in the last subsection is 62 Å for hexanol lamellae liquid crystal), which is small compared with visible light wavelength of several thousand Å, therefore we can see interference pattern only when the rotating angle is close to 90° so that the path difference can be integer multiples of the wavelength to give birefringence.

The dark pattern implies that the water layer is so narrow that all incoming light beams can not penetrate the sample material. Since the pentanol dispersion W/O = 0.6 has a very short T_2 ($T_2 = T_2^+$) corresponding to a rather long correlation time, which is proportional to Δ/d by the analysis in the last section, the water layer thickness of the liquid crystal phase is quite small and is consistant with the dark pattern result by visual observation. The portion of the liquid crystal phase in the pentanol dispersion W/O = 0.6 is very small so that unlike Fig.(78) there is no difference $|a_o - a_1|$; i.e., the echoes are normal. For temperature above 32°C, it is conjected that the thermal expansion and reformation of the domains due to molecular motion increase the thickness of the water layer, only the light with short wavelength is possible to have interference pattern. This is why we see very light purple birefringence. The weak birefringence disappears again at 72°C and becomes bright transparent, when the thermal motion of the water molecules are strong enough to break the liquid crystal phase.

Even though the portion having liquid crystal characteristic is not apparent in the pentanol dispersion W/O = 0.6 at room temperature, it may still provides an adequate path for the translational motion of charge carriers such as potassium ions, in which case we can understand why the electric conductivity is much higher than in the hexanol microemulsions, which have isolated water spheres to prohibit the motion of the potassium ions.

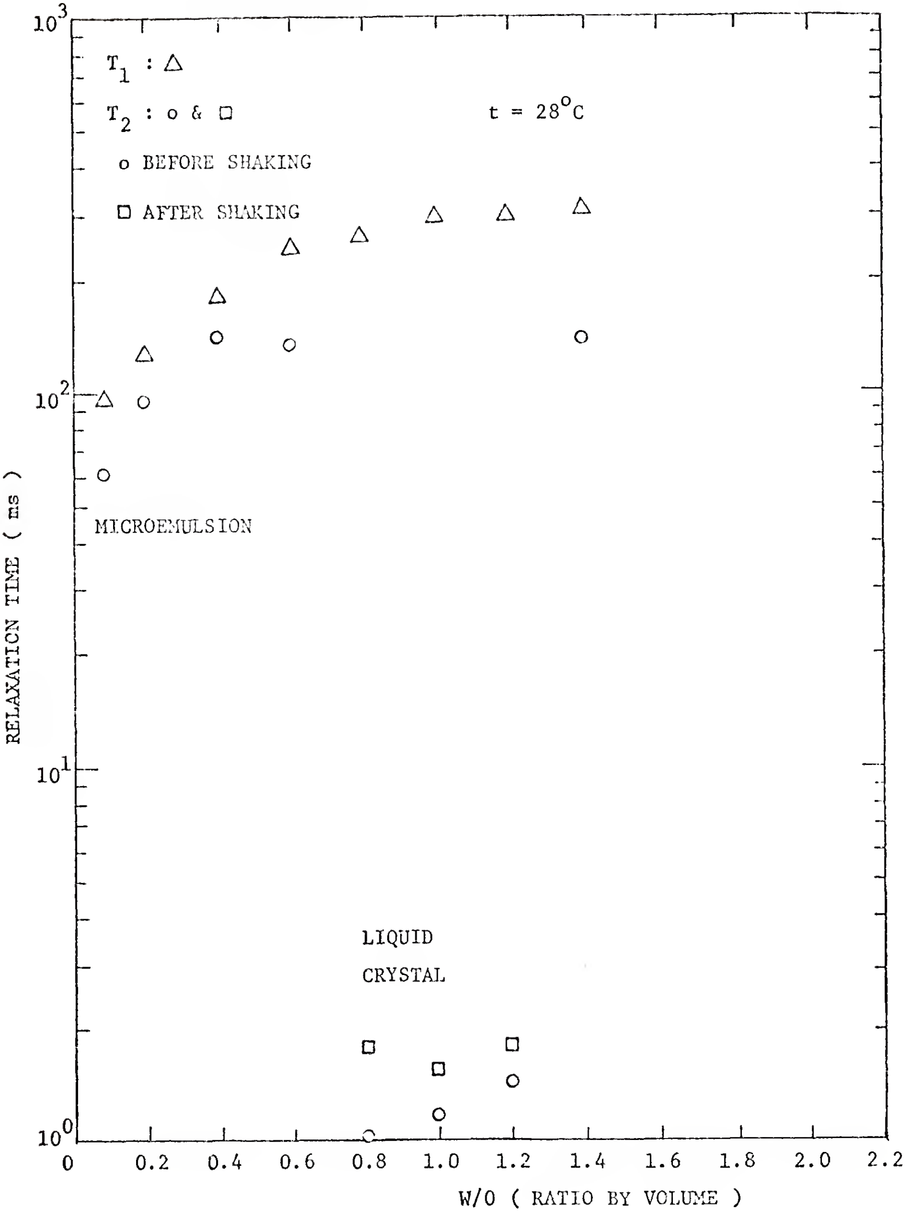

Fig.(76) Composition dependence of the relaxation times of the pentanol dispersion system with S/O = 0.2

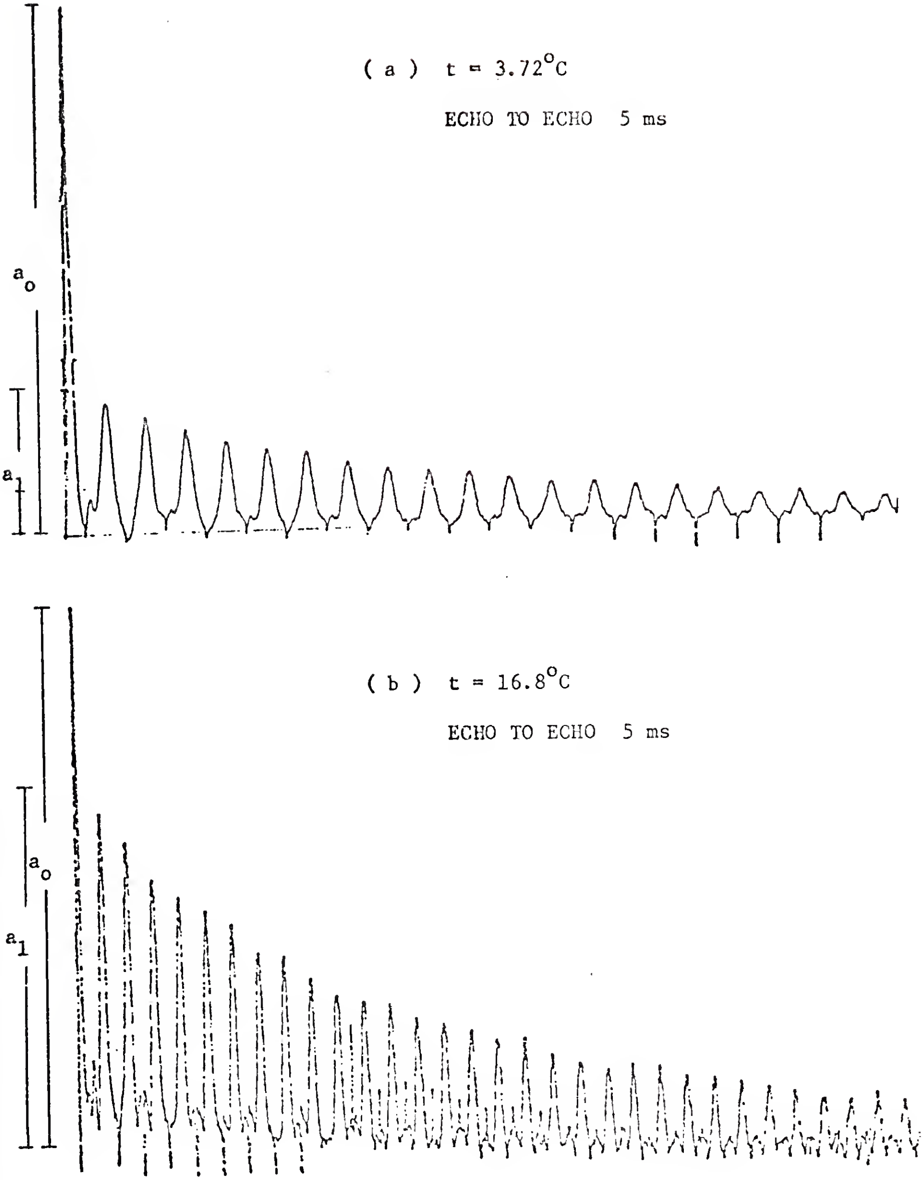

Fig. (77) The pattern of spin echo of the pentanol emulsion W/O = 0.6 with S/O = 0.2 at 3.72°C and 16.8°C (Carr-Purcell-Gill-Meiboom method)

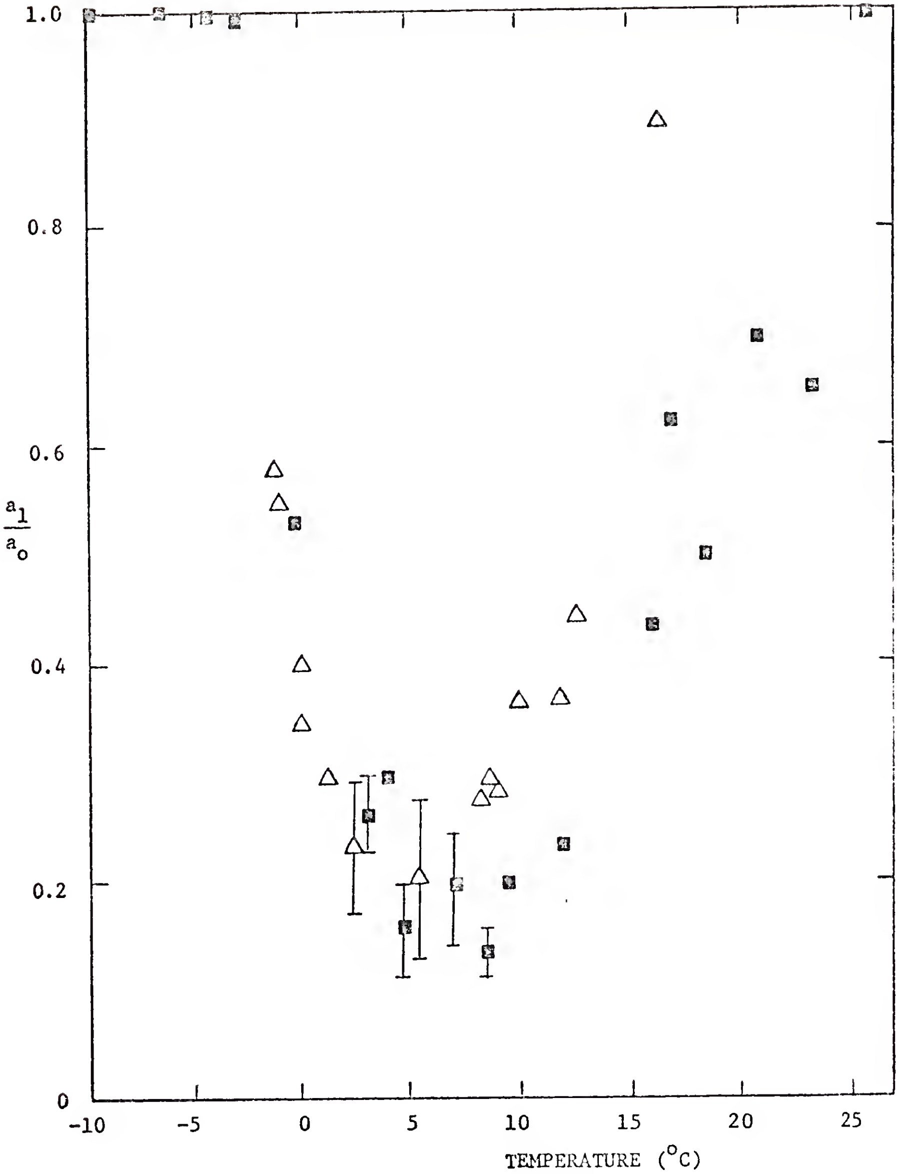

Fig.(78) Temperature distribution of two features of spin echoes in pentanol emulsion W/O = 0.6 with S/O = 0.2 (Δ: TWO PULSES METHOD: ■ : CARR-PURCELL-GILL-MEIBOOM METHOD)

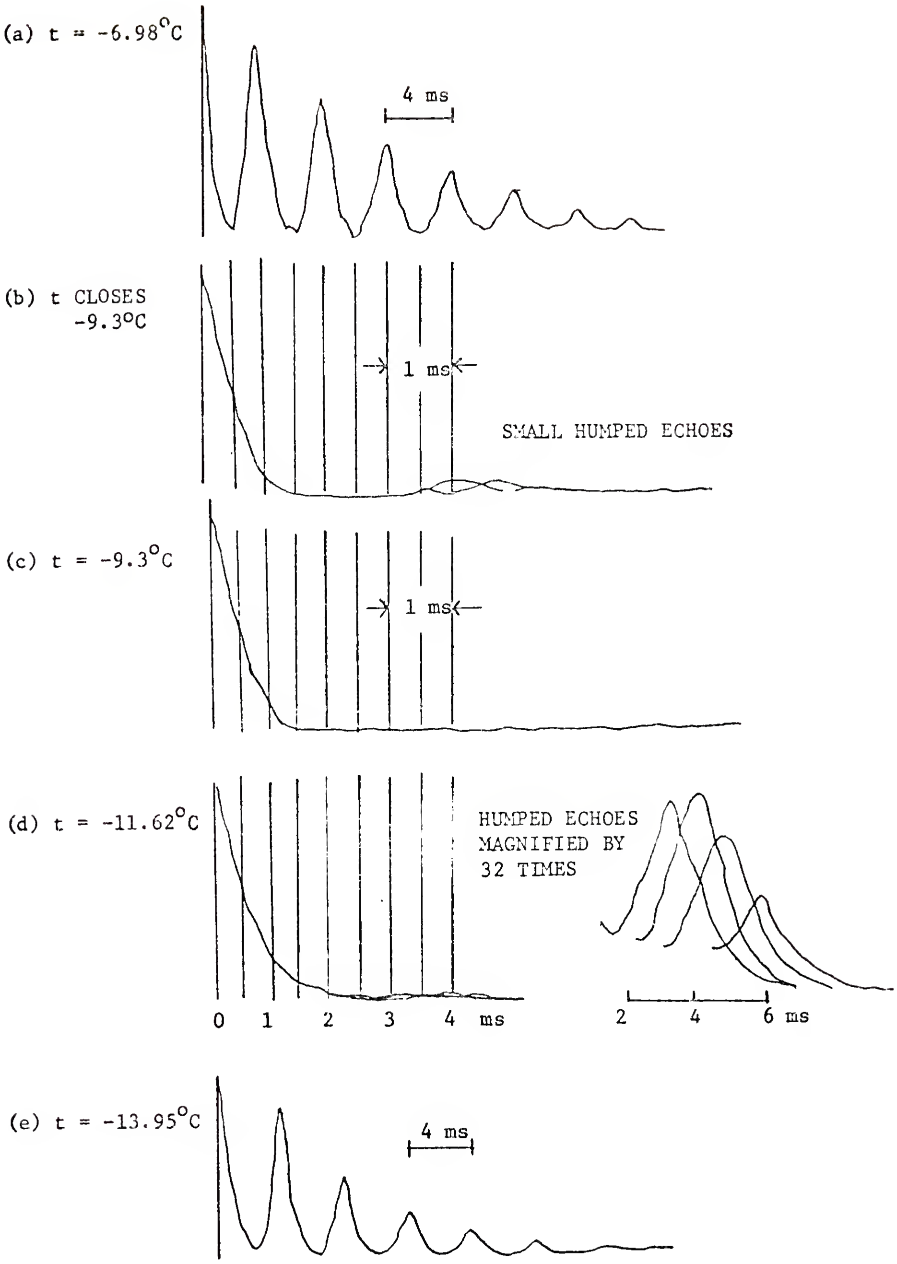

Fig.(79) The change of spin echoes of the pentanol emulsion W/O = 0.6 with S/O = 0.2 on cooling

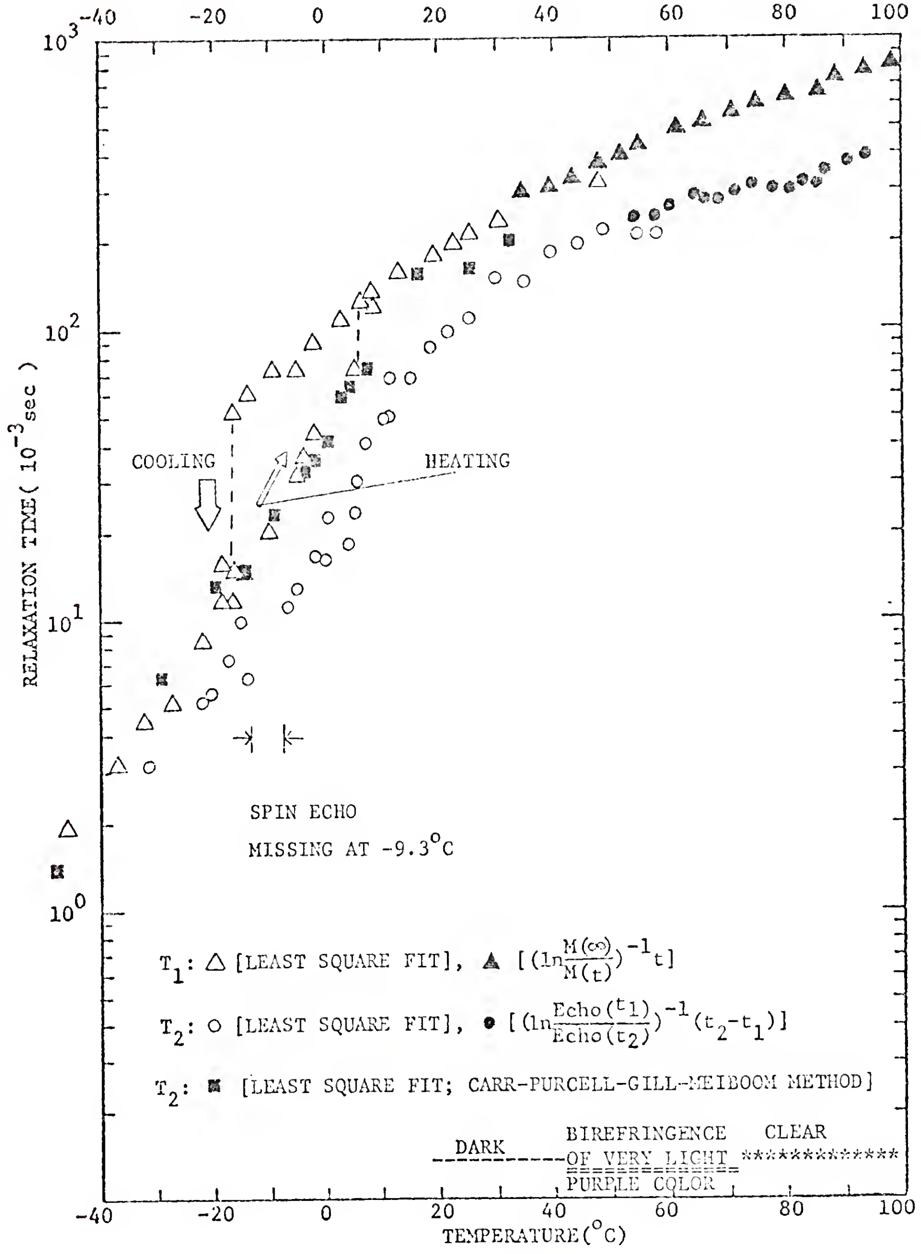

Fig.(80) The temperature dependence of the relaxation times of pentanol emulsion W/O = 0.6 with S/O = 0.2

IV.4 Conclusions

Continuous wave and pulse techniques have both been used to study deuteron NMR lineshape, resonance frequencies, and relaxation times T_1 and T_2 in oil-water dispersions as a function of temperature and composition. A model in which the water molecules rapidly exchange between a "bound" state on the surfactant interface and a "free" state in the bulk liquid is highly successful in explaining many of the observations.

For the microemulsions the relaxation rate is proportional to the reciprocal of the radius of the water droplet spheres dispersed in the oil. Analysis of the data and calculation of the relaxation times of bound water using formula(IV.1.1.6) demonstrates that only one molecular layer is bound to the polar groups of the surfactants. The correlation time for both bound and free molecules is on the order of 10^{-12} sec, which is fast compared with the reciprocal of the resonance frequency (10^{-6} sec). The electric quadrupole interaction is averaged to zero by the rapid interchange of water between the two states and diffusion of "bound" molecules around the spherical surface of the droplets. High resolution proton spectra obtained on a partially deuterated sample (water: 90% H_2O + 10% D_2O original mixture) clearly demonstrate that chemical exchange takes place at room temperature and higher between the OH of hexanol and DOH. At 23°C the hexanol OH appears as a partially resolved peak on the strong water OH peak showing therefore a condition of intermediate exchange. As the temperature is raised to 60°C the exchange becomes complete and the lines merge and then narrow still further due to decreasing viscosity as the temperature is increased to 80°C. This chemical exchange is believed to be correlated with an anomalous behavior of the spin-spin relaxation time T_2 occurring in the vicinity of $57^{o}C$.

The cylindrical rod and lamellar liquid crystal phases exhibit a static quadrupolar splitting of several hundred Hz, which was most readily observed as a CW powder pattern spectrum. The spectrum is drastically modified both at low temperature due to disruption of the liquid crystal structure by ice crystallization and at high temperature due to thermal agitation and phase separation. The observed quadrupolar splitting is approximately ten times smaller than is expected from the two state bound-free model without the occurrence of additional motional averaging. The small value of the quadrupole splitting is therefore attributed to additional degrees of freedom including (i) librational and vibrational modes of the bound D_2O molecules, (ii) tumbling of the water molecules occurring as bonds with the polar groups of the surfactants are broken and reformed at the same site, and (iii) motion (within the relevant time scale) of the group to which the water is bound. The correlation time for slowest tumbling of the bound water at room temperature, 0.32×10^{-6} sec, is only slightly larger than the characteristic time of the experiment, approximately 0.15×10^{-6} second. The quadrupolar splitting in the hexanol cylindrical rod liquid crystal is slightly larger than in the lamellar phase. The difference is attributed to the curved geometry of the interface which tightens the packing of the polar groups and therefore restricts their motion as well as that of the bound water, thus reducing the degree of motional averaging. Vigorous shaking of the liquid crystal samples is observed to substantially increase the T_2. This effect arises from disruption of the structure which permits more extensive translational motion of the water. A similar effect is observed when the liquid crystal long range order is disrupted by partial freezing of the mixture. Shaking of the sample results in a drastic viscosity increase precisely because of the mutual entanglement of the entire structure. Visual observations of the samples as a function of temperature show partial separation occurring above 80°C for lamellar and 60°C for cylindrical rod structures, in agreement with the resonance data.

The pentanol emulsion with W/O = 0.6 ; S/O = 0.2 was surveyed with relaxation time measurements and visual observations in order to obtain better understanding of why it displays a different electrical resistivity than hexanol. There are two coexisting features of the spin echoes, one for isotropic microemulsion and the other for a liquid crystalline structure with $T_2 \equiv T_2^+ \simeq 0.72$ ms. The portion having a liquid crystal characteristic is temperature dependent and is presumed to provide paths for charge carriers such as potassium ions, which enhances the electrical conductivity. This is also supported by the results of visual observation. A dark pattern is observed from 18°C to 42°C implying a very narrow water layer characteristic of the liquid crystal phase exists. The narrow water layer prohibits the penetration of the visible light. Above 42°C thermal expansion and reformation of the domains due to molecular motion increase the thickness of the water layers and thus gives purple colored birefringence, which in turn disappears above 72°C and the sample becomes clear and bright. If the cosolubilized molecular solution were true for the pentanol emulsions, the visual observation should give the same bright and clear pattern as that of the microemulsions.

APPENDIX A

```
10 REM    THIS PROGRAM CALCULATES SPIN LATTICE RELAXATION TIME BY AN
11 REM    ITERATIVE LEAST SQUARES FIT OF THE EQUATION A + B*EXP(-T/T1)
12 REM    TO FID DATA.  AN INITIAL GUESS FOR T1 IS REQUIRED.
13 REM    RELEVANT REFERENCE: J. MAGN. RES. VOL. 25, 263 (1977).
16 REM    INPUT DATA
25 FILEV#1:"LPT:"
30 DIM X$(60) \ DIM A(19) \ DIM T(19)
31 DIM E(19) \ DIM S(19) \ DIM Y(19)
35 PRINT "SAMPLE NAME "; \ INPUT X$
40 PRINT "TEMPERATURE "; \ INPUT X2
45 PRINT "NUMBER OF DATA POINTS "; \ INPUT N
50 PRINT "FID AMPLITUDE","  TIME"
55 FOR I=1 TO N
60 INPUT A(I)
65 PRINT TAB(16);" "; \ PRINT PNT(27);"A";
70 INPUT T(I)
75 NEXT I
80 PRINT "DO YOU WANT THIS DATA TABLE PRINTED ";\INPUT Y$
85 PRINT "T1 GUESS ";\INPUT G
87 LET R=-1/G
90 PRINT "DO YOU WANT T1 PRINTED AFTER EACH ITERATION ";\INPUT Z$
92 PRINT#1:"SAMPLE NAME ";X$
94 PRINT#1:"TEMPERATURE= ";X2
96 PRINT#1:
98 IF Y$="YES" GOTO 350
99 PRINT
100 REM   SUMS SET TO ZERO AND CALCULATION BEGINS
101 PRINT
105 FOR K=0 TO 9
110 LET S(K)=0
115 NEXT K
120 FOR I=1 TO N
125 LET E(I)=EXP(R*T(I))
130 LET S(0)=S(0)+E(I) \ S(1)=S(1)+E(I)^2
135 LET S(2)=S(2)+A(I) \ S(3)=S(3)+A(I)*E(I)
140 LET S(4)=S(4)+A(I)*T(I)*E(I) \ S(5)=S(5)+T(I)*E(T)
145 LET S(6)=S(6)+T(I)*E(T)^2 \ S(7)=S(7)+A(I)*E(T)*T(I)^2
150 LET S(8)=S(8)+E(I)*T(I)^2 \ S(9)=S(9)+E(I)^2*T(I)^2
155 NEXT I
160 LET A=N*S(1)-S(0)^2 \ B=S(3)*S(0)-S(2)*S(1)
165 LET C=S(2)*S(0)-N*S(3) \ D=N*S(6)-S(5)*S(0)
167 LET E=S(3)*S(5)-S(2)*S(6)
170 LET G1=A*S(4)+B*S(5)+C*S(6)
175 LET G2=D*S(4)+A*S(7)+E*S(5)+B*S(8)+2*C*S(9)
180 LET R=R-G1/G2
196 IF Z$<>"YES" GOTO 200
198 PRINT#1:-1/R
```

```
200 IF ABS((G1/G2)/R)<0.001 THEN 210
205 GOTO 105
210 LET M=-C/A \ H=(S(2)-M*S(0))/N \ Q=0
211 PRINT#1:
215 FOR I=1 TO N
220 LET Y(I)=H+M*E(I) \ Q=Q+(Y(I)-A(I))^2
222 PRINT#1:Y(I),Q
225 NEXT I
230 PRINT#1:
235 PRINT#1:"RELAXATION TIME= ";-1/R
240 PRINT#1:"A= ";H
245 PRINT#1:"B= ";M
250 PRINT#1:"SUM OF SQUARES= ";Q
255 PRINT#1:
260 PRINT#1:
265 PRINT#1:
280 CLOSE#1
290 STOP
350 PRINT#1:"FID AMPLITUDE"," TIME"
355 FOR I=1 TO N
360 PRINT#1:A(I),T(I)
365 NEXT I
367 PRINT#1:
370 GOTO 105
400 END
```

APPENDIX B

```
10 REM THIS PROGRAM CALCULATES RELAXATION TIMES BY AN ITERATIVE
11 REM  LEAST SQUARES FIT OF THE EQUATION A + B*EXP(-T/T1) TO
12 REM  AMPLITUDE VS TIME DATA.  EXPERIMENTAL DATA MUST BE
13 REM  ENTERED AS DATA STATEMENTS STARTING WITH LINE 300 (DO NOT
14 REM  EXCEED LINE 339).  AN INITIAL GUESS FOR RELAXATION TIME
15 REM  IS REQUIRED.
16 REM  RELEVANT REFERENCE: J. MAGN. RES. VOL. 25, 263 (1977).
25 FILEV#1;"LPT:"
30 DIM X$(60) \ DIM A(19) \ DIM T(19)
31 DIM E(19) \ DIM S(19) \ DIM Y(19)
35 PRINT "SAMPLE NAME ";  \ INPUT X$
36 PRINT#1;"SAMPLE NAME ";X$
37 PRINT#1;
38 PRINT "DO YOU WANT T1 PRINTED AFTER EACH ITERATION";\INPUT Z$
39 PRINT "DO YOU WANT DATA TABLES PRINTED ";\INPUT Y$
40 PRINT "NUMBER OF RUNS ";\INPUT P
41 FOR J=1 TO P
43 PRINT "TEMPERATURE ";\INPUT X2
45 PRINT "NUMBER OF DATA POINTS "; \ INPUT N
55 FOR I=1 TO N
60 READ A(I), T(I)
75 NEXT I
85 PRINT "T1 GUESS ";\INPUT G
87 LET R=-1/G
94 PRINT#1;"TEMPERATURE= ";X2
96 PRINT#1;
98 IF Y$="YES" GOTO 350
99 PRINT
100 REM   SUMS SET TO ZERO AND CALCULATION BEGINS
101 PRINT
105 FOR K=0 TO 9
110 LET S(K)=0
115 NEXT K
120 FOR I=1 TO N
125 LET E(I)=EXP(R*T(I))
130 LET S(0)=S(0)+E(I) \ S(1)=S(1)+E(I)^2
135 LET S(2)=S(2)+A(I) \ S(3)=S(3)+A(I)*E(I)
140 LET S(4)=S(4)+A(I)*T(I)*E(I) \ S(5)=S(5)+T(I)*E(I)
145 LET S(6)=S(6)+T(I)*E(I)^2 \ S(7)=S(7)+A(I)*E(I)*T(I)^2
150 LET S(8)=S(8)+E(I)*T(I)^2 \ S(9)=S(9)+E(I)^2*T(I)^2
155 NEXT I
160 LET A=N*S(1)-S(0)^2 \ B=S(3)*S(0)-S(2)*S(1)
165 LET C=S(2)*S(0)-N*S(3) \ D=N*S(6)-S(5)*S(0)
167 LET E=S(3)*S(5)-S(2)*S(6)
170 LET G1=A*S(4)+B*S(5)+C*S(6)
175 LET G2=D*S(4)+A*S(7)+E*S(5)+B*S(8)+2*C*S(9)
180 LET R=R-G1/G2
```

```
196 IF Z$<>"YES" GOTO 200
198 PRINT#1:-1/R
200 IF ABS((G1/G2)/R)<0.001 THEN 210
201 IF R>0 GOTO 340
205 GOTO 105
210 LET M=-C/A \ H=(S(2)-M*S(0))/N \ Q=0
211 PRINT#1:
215 FOR I=1 TO N
220 LET Y(I)=H+M*E(I) \ Q=Q+(Y(I)-A(I))^2
222 PRINT#1:Y(I),Q
225 NEXT I
230 PRINT#1:
235 PRINT#1:"RELAXATION TIME= ";-1/R
240 PRINT#1:"A= ";H
245 PRINT#1:"B= ";M
250 PRINT#1:"SUM OF SQUARES= ";Q
255 PRINT#1:
260 PRINT#1:
265 PRINT#1:
267 NEXT J
280 CLOSE#1
290 STOP
340 PRINT#1:"NEGATIVE RELAXATION TIME"
342 GOTO 255
350 PRINT#1:"AMPLITUDE"," TIME"
355 FOR I=1 TO N
360 PRINT#1:A(I),T(I)
365 NEXT I
367 PRINT#1:
370 GOTO 105
400 END
```

BIBLIOGRAPHY

[1] E. Oldfield, D. Chapman and W. Derbyshire, FEBS Letter 16, 102 (1971)

[2] J. M. Graham, Biochem. Biophys. Acta, 241, 180(1971)

[3] E. G. Finer, Biochem. Biophys. Acta, 260, 59(1972)

[4] I. C. P. Smith, Biochem. Biophys. Res. Comm., 49, No.4, 916(1972)

[5] J. Seelig, Biochem. Biophys. Res. Comm., 57, No.2, 406(1974)

[6] D. O. Shah and R. D. Walker, AIChE Journal, 18, No.6, 1116(1972)

[7] P. Ekwall and L. Mandell, Kolloid-Z., 169, 113(1960)

[8] J. H. Schulman and J. A. Friend, J. Colloid Sci. 4, 497(1949)

[9] J. H. Schulman and D. P. Riley, J. Colloid Sci. 3, 383(1948)

[10] C. E. Cook and J. H. Schulman, "SURFACE CHEMISTRY,"(Proceedings of the Second Scandinavian Symposium on Surface Activity, 1964)

[11] W. Stoeckenius, J. H. Schulman and L. M. Prince, Kolloid-Z., 169, 170(1960)

[12] J. E. Bowcott and J. H. Schulman, Z. Elektrochem., 59, 283(1955)

[13] G. Gillberg, H. Lehtinen, and S. Friberg, J. Colloid Interface Sci., 33, 40(1970)

[14] D. O. Shah and R. M. Hamlin, Jr., Science, 171, 483(1971)

[15] D. O. Shah and R. D. Walker, AIChE Journal, 18, No. 6, 1117(1972)

[16] L. M. Prince, J. Colloid and Interface Sci., 55, No. 1, 182(1975)

[17] D. O. Shah, J. Colloid and Interface Sci., 37, No. 4, 744(1971)

[18] D. O. Shah, J. W. Falco and R. D. Walker, AIChE Journal, 20, No. 3, 510(1974)

[19] E. L. Hahn, Phys. Rev., 80, 580(1950)

[20] H. Y. Carr and E. M. Purcell, Phys. Rev., 94, 630(1954)

[21] A. Abragam, "The Principles of Nuclear Magnetism," Oxford Univ. Press, 160(1961)

[22] E. M. Pound, Phys. Rev., 79, 685(1950)

[23] N. Bloembergen, Thesis, Univ. of Leiden(1948)

[24] D. Eisenberg, "The Structure and Properties of Water," Oxford Univ. Press, New York(1969)

[25] J. C. Hindman, J. Chem. Phys., 54, No. 2, 621(1971)

[26] T. E. Bopp, J. Chem. Phys., 47, 3621(1967)

[27] W. T. Huntress, Jr., J. Phys. Chem., 73, 103(1969)

[28] J. E. Anderson and P. A. Fryer, J. Chem. Phys., 50, 3784(1969)

[29] J. R. Zimmerman and W. E. Brittin, J. Phys. Chem., 61, 1328(1957)

[30] B. T. Feld and W. E. Lamb, Jr., Phys. Rev., 67, No. 1, 15(1945)

[31] E. M. Pound, Phys. Rev., 79, 695(1950)

[32] R. G. Barnes and J. W. Bloom, J. Chem. Phys., 57, No. 8, 3082 (1972)

[33] E. G. Finer, J. Chem. Soc. Faraday Trans., II, 69, 1590(1973)

[34] E. M. Pound, Phys. Rev., 72, 1233(1947)

[35] A. Abragam, "The Principles of Nuclear Magnetism," Oxford Univ. Press, 352(1961)

[36] S. Meiboom and D. Gill, Rev. Sci. Instr., 29, 688(1958)

[37] W. A. Anderson, Rev. Sci. Instr., March, 1160(1962)

[38] M. Sass and D. Ziessow, J. Mag. Res., 25, 263(1977)

[39] W. Dietrich and R. Gerhards, J. Mag. Res., 23, 21(1976)

[40] T. K. Leipert and D. W. Marquardt, J. Mag. Res., 24, 181(1976)

[41] J. R. Hansen, J. Phys. Chem., 78, No. 3, 256(1974)

[42] D. E. Woessner, J. Chem. Phys., 36, No. 1, 1(1962)

[43] D. E. Woesnner, J. Chem. Phys., 31, No. 1, 55(1959)

[44] A. Kumar and R. Ernst, J. Mag. Res., 24, 425(1976)

[45] H. S. Gutowsky, R. L. Vold and J. Wells, J. Chem. Phys., 43, 4107(1965)

[46] R. Freeman and H. D. W. Hill, J. Chem. Phys., 54, 301(1971)

[47] T. Tokuhiro and J. Fraenkel, J. Chem. Phys., 55, 2797(1971)

BIOGRAPHICAL SKETCH

Koahsiung Yang was born July 16, 1947, in Koahsiung, Taiwan province of China. In September 1965, he enrolled in the National Taiwan University in Taipei, from which he received the degree of Bachelor of Science with a major in physics in June 1969. After that, he taught general physics in the Second Army Sergeant School as military service duty for one year.

He enrolled in the Graduate School of Columbia University in New York City in September 1970, at which time he was granted a fellowship in the Physics Department and received the degree of Master of Arts and Sciences in June 1972. In September 1972 he enrolled in Graduate School at the University of Florida and has held appointments as a laboratory teaching assistant and as a research assistant, the latter in the Solid State Physics Laboratory.

I certify that I have read this study and that in my opinion it confirms to acceptable standards of scholarly presentation and is fully adequate, in scope and quality, as a dissertation for the degree of Doctor of Philosophy.

Thomas A Scott

Thomas A. Scott, Chairman
Professor of Physics

I certify that I have read this study and that in my opinion it confirms to acceptable standards of scholarly presentation and is fully adequate, in scope and quality, as a dissertation for the degree of Doctor of Philosophy.

Raymond Pepinsky

Raymond Pepinsky
Professor of Physics

I certify that I have read this study and that in my opinion it confirms to acceptable standards of scholarly presentation and is fully adequate, in scope and quality, as a dissertation for the degree of Doctor of Philosophy.

D. O. Shah

Dinesh O. Shah
Professor of Chemical Engineering

I certify that I have read this study and that in my opinion it confirms to acceptable standards of scholarly presentation and is fully adequate, in scope and quality, as a dissertation for the degree of Doctor of Philosophy.

John W. Flowers

John W. Flowers
Professor of Physics

I certify that I have read this study and that in my opinion it confirms to acceptable standards of scholarly presentation and is fully adequate, in scope and quality, as a dissertation for the degree of Doctor of Philosophy.

James W. Dufty
Associate Professor of Physics

This dissertation was submitted to the Graduate Faculty of the Department of Physics in the College of Arts and Sciences and to the Graduate Council, and was accepted as partial fulfillment of the requirements for the degree of Doctor of Philosophy.

December 1977

Dean, Graduate School

UNIVERSITY OF FLORIDA
3 1262 08666 268 0